7-2020

Ensemble and Single Particle Studies of Cation Exchange in CuInS2/ZnS QDs and Their Application in Super-Resolution Imaging

Anh Tue Nguyen
University of Arkansas, Fayetteville

Ensemble and Single Particle Studies of Cation Exchange in $CuInS_2$/ZnS QDs and Their Application in Super-Resolution Imaging

A dissertation submitted in partial fulfillment
of the requirements for the degree of
Doctor of Philosophy in Chemistry

by
Anh Tue Nguyen
National University of Vietnam
Bachelor of Science in Material Science, 2008
Purdue University
Master of Science in Chemistry, 2014

July 2020
University of Arkansas

This dissertation is approved for recommendation to the Graduate Council.

_____

Colin D. Heyes, Ph.D.
Dissertation Director

_____

Jingyi Chen, Ph.D.
Committee Member

_____

Stefan Kilyanek, Ph.D.
Committee Member

_____

Gregory Salamo, Ph.D.
Committee Member

_____

Ryan Tian, Ph.D.
Committee Member

ABSTRACT

Colloidal quantum dots (QDs) have great potential in many applications such as bioimaging, light emitting diodes, solar cells and lasers. However, a great number of studies have been focused on Cd based (II-VI) and Pb (IV-VI) based materials which are not suitable for mass production. Therefore, alternative types of QD containing less toxic materials have been introduced, including $CuInS_2$ QDs. This I-III-VI semiconductor nanocrystals also attract lots of attention due to their large Stock shift, long fluorescence lifetime and high defect tolerance, making them attractive emitters for applications in bioimaging, photovoltaics and light emitting diodes.

In the first project, we synthesized CIS/ZnS QDs using different concentration of Zn precursors. the relationships of structure, elemental composition and photophysics of the QDs were thoroughly investigated. As the concentration of Zn precursor increases up to 4 mmol the emitting centers CIS get smaller and act as dopants in zinc blende ZnS lattices. Concurrent with this transition, subpopulation blinking analysis shows a wide heterogeneity from QD to QD increased. Also, it shows that the on time blinking statistics shift from inverse power law (or multiexponential) to monoexponential behavior. We proposed a model where the different positions of CIS in ZnS is the explanation for the wide heterogeneity in blinking behavior of the QDs. We anticipate these results can be contributed to the design for a large-scale production of the QDs.

In the second project, we applied fast blinking CIS/ZnS QDs as fluorescence probes in single particle localization super resolution imaging and compared the resolution of reconstructed images with those using commercial CdSe/ZnS QDs. The results show that even CIS/ZnS QDs obtained less precision in single molecule localization, the resolution in reconstructed images of f-actins was comparable with those using commercial CdSe/ZnS QDs. This project provides some useful

insights to demonstrate that Cd-free and fast blinking CIS/ZnS QDs can be used as fluorescence probes for super resolution imaging.

ACKNOWLEDGEMENT

And this moment finally has come. I did it. This has been such a challenging journey and very important chapter in my life. Even with so much ups and downs, I would forever cherish every moment of it.

First of all, I would like to express my special gratitude and appreciation to my Ph.D. advisor, Dr. Colin Heyes for his guidance and encouragement throughout the journey. I want to thank my committee members, Dr. Chen, Dr. Kilyanek, Dr. Tian and Dr. Salamo for their fruitful discussion during committee meetings. Thank you Dr. Mourad Benamara for his help during all of my TEM sessions. I would like to thank Colette for teaching me CIS synthesis when I first joined the lab. I am grateful for the help and contributions from Dr. Feng Gao and Dr. Dustin Baucom during my research. Sincere regards to all group members, I enjoyed every moment we had together.

Con cảm ơn bố mẹ đã có công sinh thành và nuôi dưỡng con nên người. Bố mẹ luôn luôn là nguồn động lực to lớn để con vươn lên để thành công hơn trong cuộc sống. Cảm ơn em gái đã luôn động viên và chia sẻ với anh Hai. Và cảm ơn Ngọc đã ở bên anh trong chặng đường khó khăn và gian nan này.

TABLE OF CONTENT

CHAPTERS

LIST OF PUBLICATIONS

Chapter 2. Nguyen, A. T., Gao, F., Baucom, D., Heyes, C.D. $CuInS_2$-doped ZnS Quantum Dots Obtained via Non-Injection Cation Exchange Show Reduced but Heterogeneous Blinking and Provides Insights into their Structure-Optical Property Relationships. J. Phys. Chem. C 2020, 124, 10744-10754.

Chapter 3. Nguyen, A. T., Baucom, D., Wang, Y., Heyes, C.D. Compact and blinking Cd-free quantum dots for single-particle super-resolution imaging (to be submitted).

Chapter 1. Introduction

1.1. Quantum dots

1.1.1. Quantum confinement in quantum dots

Quantum dots are nanoscale semiconductors with sizes usually less than ~10 nm. A material is defined as a semiconductor when there is a low-to-moderately sized energy gap (< ~3eV) separating the conduction bands from the valence bands. In a bulk semiconductor, the width of this energy gap is a fixed parameter and is dependent only on the material. However, when the size of a semiconductor becomes comparable to or smaller than the length of the excited electron-hole pair separation (exciton Bohr radius), electronic excitations experience the presence of the particle boundaries in all three dimensions (for spherical particles) and respond to changes in the particle size by adjusting their energy spectra. This phenomenon is known as quantum confinement and nanoscale particles that exhibit it are often referred to as quantum dots (QDs). As the QD size decreases, the energy gap separating conduction bands and valence bands increases, resulting in a decrease (blue shift) of the excitation and emission wavelengths (figure 1.1a). Moreover, because of the quantum confinement, the continuous energy bands of the bulk semiconductor turn into discrete, atomic-like energy levels for QDs. Thus, QDs are also known as artificial atoms. These discrete energy levels of QD can be labeled using atomic-like notations (1S, 1P, 1D, etc.), as illustrated in figure 1.1b.[1] The discrete structure of energy states leads to the discrete absorption spectrum of QDs, which is in contrast to the continuous absorption spectrum of a bulk semiconductor (figure 1.1c). Semiconductor QDs bridge the gap between cluster molecules and bulk materials although the boundaries between molecular, QD, and bulk regimes are not well defined and strongly depend on materials. In general, a material can be considered as QD when it contains approximately from ~100 to ~10,000 atoms.

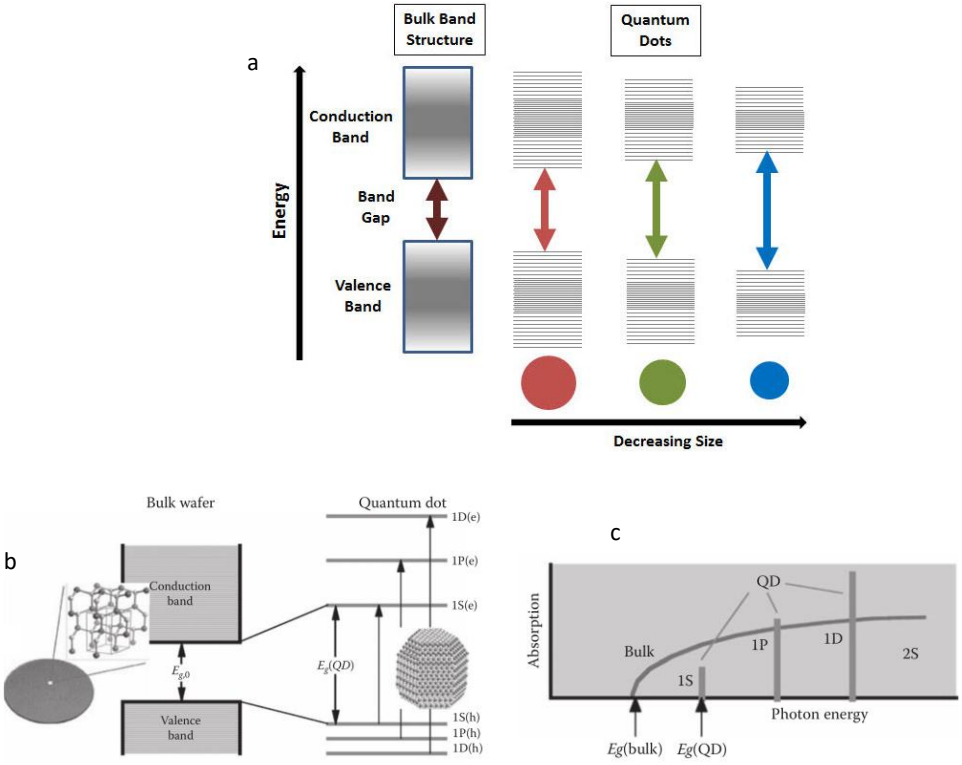

Figure 1.1. (a) Emission wavelength of QDs can be tuned by adjusting the size of the QDs. (b) A bulk semiconductor has continuous conduction and valence energy bands separated by a fixed energy gap, $E_{g,0}$ (left), while a QD is characterized by discrete atomic-like states with energies that are determined by the QD (right). (c) A schematic representation of the continuous absorption spectrum of a bulk semiconductor (curved line), compared to the discrete absorption spectrum of a QD (vertical bars). Image is modified from ref.1 and https://www.sigmaaldrich.com/technical-documents/articles/materials-science/nanomaterials/quantum-dots.html.

The Bohr radius of a QD is defined as

$$a_B = \varepsilon \frac{m}{m^*} a_o \qquad \text{(Eq. 1.1)}$$

where ε is the dielectric constant of the material, m* is the mass of the particle, m is the rest mass of the electron, and a_o is the Bohr radius of the hydrogen atom. For a QD, it is convenient to consider three different Bohr radii: one for the electron (a_e), one for the hole (a_h), and one for the exciton (electron–hole pair) (a_{exc}). In the case of the exciton, the reduced mass of the electron–hole pair is used for m*. When comparing the QD radius, a, with those three Bohr radii, three different

situations can be considered. First, when a is much smaller than a_e, a_h, and a_{exc} (i.e., when a < a_e, a_h, a_{exc}), this is known as the strong confinement regime. Second, when a is larger than both a_e and a_h, but is smaller than a_{exc}, (i.e., when a_e, a_h < a < a_{exc}), this limit is called the weak confinement regime. Finally, when a is between a_e and a_h (e.g., when a_h < a < a_e, a_{exc}), this is the intermediate confinement regime. Of course, the confinement regime depends on the material and size of the QD. For example, the exciton Bohr radius of InAs is 36 nm, thus InAs QDs in the ~10 nm size scale are in the strong confinement regime. In contrast, CuCl has an exciton Bohr radius of 0.7 nm so that CuCl QDs of similar sizes are in the weak confinement regime. The Bohr radius of CdSe is 6 nm so it can be in either the strong confinement or the intermediate confinement regime, depending on the exact size of the QD.[1]

Based on the semiconductor material and its bulk bandgap, Brus developed an approximate relationship between the size of QD and its bandgap.[2]

$$E_g^{QD} = E_g^{bulk} + \frac{h^2}{8m_0r^2}\left(\frac{1}{m_e^*}+\frac{1}{m_h^*}\right) - \frac{1.8e^2}{4\pi\varepsilon_0\varepsilon r} \qquad \text{(Eq. 1.2)}$$

E_g^{QD} is the theoretical bandgap of QD, E_g^{bulk} is the bandgap of the bulk material, h is Planck's constant, r is the radius of nanoparticle, m_0 is the mass of an electron, m_e* is the effective mass of the electron, m_h* is the effective mass of hole, e is the charge of electron, ε_0 is the permittivity of free space, ε is the permittivity of the material.

The first term is based on the properties of the bulk material, the second term is based on the particle-in-a-box confinement of the exciton, and the third term is based on the Coulombic attraction between the electron and the hole.

1.1.2. Photophysics of single quantum dots

Since they were first reported by Ekimov et al.[3] and Brus et al.,[4] QDs have been considered as a versatile candidate in many applications, including solar cells,[5] bioimaging,[6-7] and displays.[8] However, in 1996 Nirmal et al. reported a blinking phenomenon of isolated CdSe QDs under steady-state laser excitation conditions.[9] Blinking is a phenomenon in which, even under constant illumination, single QD fluoresce intermittently and stochastically. The incoherency of such blinking behavior of single QD would be averaged out and therefore undetectable in an ensemble measurement.

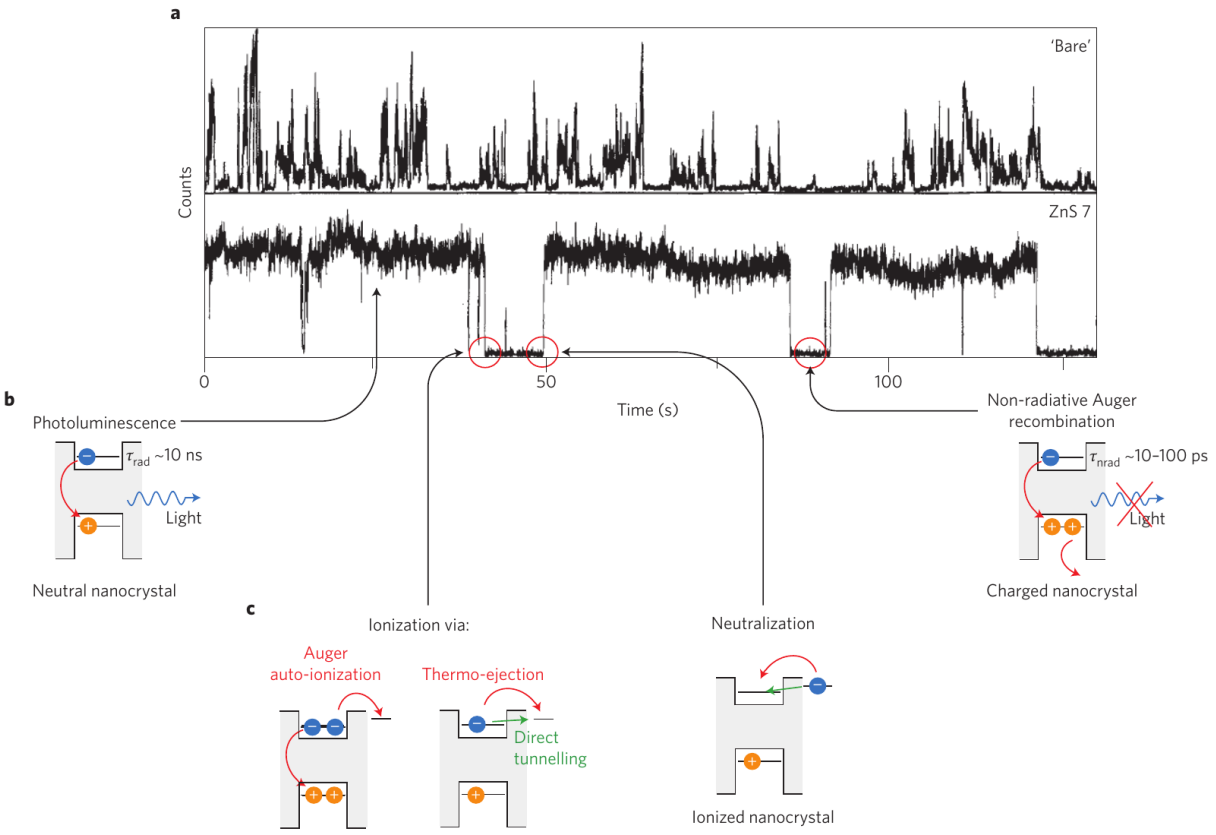

Figure 1.2. Blinking of single QD. (a) The time dependence of the PL intensity of a single CdSe QD with a radius of 2.1 nm (upper panels) and CdSe coated with a seven-monolayer-thick ZnS shell (lower panel) under a continuous-wave excitation intensity of 0.7 kW cm^{-2} as reported in ref.. (b) Schematics of explanation for blinking in QDs. Optical excitation of the neutral QD leads to PL with a radiative decay time τ_{rad} on the order of 10 ns; excitation of the charged QD leads to fast non-radiative Auger recombination with a decay time τ_{nrad} on the order of 10–100 ps. Arrows

show the phenomena that control fluorescence trajectory measured in a single CdSe QD. (c) Processes leading to QD ionization and neutralization. Image is modified from ref. 10.

Figure 1.2a shows the time-dependent PL intensity of a single CdSe QD with a radius of 2.1 nm under continuous illumination.[10] Obviously, the time dependence of PL intensity exhibits a sequence of 'on' and 'off 'periods. After the QD was coated with a seven-monolayer-thick ZnS shell, the duration of the 'on' periods is longer than that for CdSe QD. Since this report, many research groups have observed this effect at various temperatures in many types of QD and nanowire. QD blinking dynamics is observed even down to very low temperatures (4 K), which rules out thermally activated processes as the source. Given the excellent photophysical attributes for QDs noted under ensemble conditions, blinking at the single-level QDs can limit their applications when quantitative emission is required.

Currently, the most widely accepted explanation is that the blinking phenomenon arise due to illumination-induced charging (on → off) followed by reneutralization (off → on) of the QD.[11-12] This occurs because, for a neutral QD, a photon excites an electron–hole pair (exciton), which then recombines, emitting another photon and thus QD fluoresce (Fig. 2b), a process known as radiative recombination. In the presence of an excess charge (or, more accurately, charge separation in a neutral QD) a process known as non-radiative Auger recombination occurs, by which the additional exciton energy is efficiently transferred to the extra electron or hole non-radiatively (Fig. 2b). As a simple physical picture, one can think of the extra carrier as a third body that can take away the excess energy of the exciton. Because the rate of Auger-assisted recombination can be orders of magnitude faster than that of radiative recombination, the radiative emission can therefore be strongly suppressed in charge-separated QDs.

The switching time between on and off states is stochastic and seemed to span multiple timescales. When on or off event durations are plotted on a log-log scale, a negative linear dependence was observed (figure 1.3b and c), and was interpreted as inverse power law behavior according to Eq. 1.3.[13]

$$P_{(On\ or\ Off)} = At^{-m} \qquad \text{(Eq.1.3)}$$

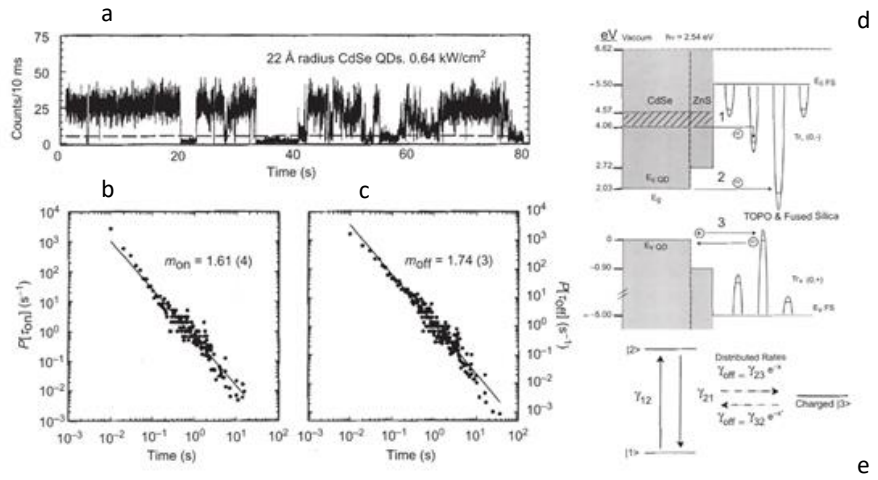

Figure 1.3. (a) Typical blinking trace of CdSe, (b) probability distribution of on-time durations (log-log plot), (c) probability distribution of off-time durations (log-log plot), (d) physical model of hot electron trapping (process 1) and quantum mechanical tunneling of electrons (process 2) or holes (process 3) to external trap states underlying blinking, (e) distributed rates of QD charging used to explain the inverse power-law dynamics of blinking shown in (b) and (c). Image is modified from ref. 13.

In 2003 Kuno and Nesbitt reported the first model to explain the blinking phenomenon of QD, indicating that external trap states in the ligand and/or substrate have stochastically time-varying energy and distance from the QD (figure 1.3d and e).[14] The stochastically-varying trapping rate of external trapping/charging led to a power law behavior in the on-times, and a diffusive random walk of the trapped external charge back to the charged QD led to power law behavior in the off times. The value of the exponent, α, in a 1-D random walk model is 3/2, which agreed with most

experimental data at the time. On the other hand, some other studies noted a cutoff in the on times that limited the maximum length of on events, modifying Eq. (1.3) to Eq. (1.4) for on events.[15]

$$P_{(On)} = At^{-m}\exp(-t/\tau_c) \qquad \text{(Eq.1.4)}$$

The dependence of the values of the power law exponent in Eq. (1.3) and (1.4) and of the characteristic cutoff time in the exponential term, τ_c of Eq. (1.4) under different conditions has been extensively examined over the years. For example, one of the early landmark studies by the Bawendi group showed a truncation in the exponential cutoff time for the on states with increasing QD size, excitation power and temperature or with ZnS capping, although the exact ZnS shell thickness was not given.[15] Meanwhile Heyes et al. reported a negligible effect of ZnS shell thickness on either power law exponent or exponential cutoff time.[16] These inconsistencies suggested that microscopic structural differences in the shells and/or core-shell interface may play a role.

Two theoretical models were published by the Marcus group at approximately the same time that provided alternative explanations to the power law blinking dynamics from that of figure 1.3d.[17-18] The first, proposed by Tang and Marcus, is not dissimilar to the model in figure 1.3d, but interprets it as a photoinduced diffusion-controlled electron transfer (DCET) model between bright and dark states based on the foundation of (Nobel prize winning) Marcus theory.[17] The second, proposed by Frantsuzov and Marcus, used a model in which a long-lived trap state hypothesis was not needed, relying on a fluctuating resonance between hole trapping energy and electronic excitation energy.[18]

Since blinking can limit the potential application of QDs in various fields, there are many methods have been developed to reduce blinking of QDs,[19-20] one of which is to encapsulate the core with a “giant” epitaxial shell.[21] During the shelling chemistry for core QD, one should consider the

difference bandgap and lattice mismatch of core and shell materials, since these factors have significant effect on the blinking of final core/shell QDs. In fact, the Heyes group reported that a balance between wavefunction confinement and induced lattice strain by a multishell structure of CdSe/CdS/ZnS can be used to reduce blinking when the ZnS outer shell is thin. However, as the thickness of the outer ZnS shell increases, blinking increases due to the formation of trap states at the interface induced by the lattice strain, leading to a "Goldilocks effect" of finding just the right shell thickness to reduce blinking while keeping the QD relatively compact.[22] When toxicity is less of an issue, complete or near-complete suppression of blinking has been reported for CdSe/CdS core/shell QDs, which allows for epitaxial growth of very thick shells (12–15 monolayers) due to the low lattice mismatch between CdSe and CdS.[21] This approach both reduced interfacial trap states and isolated the QD from external trap states. Subsequently, through carefully growing the shell with exceptionally high crystallinity by changing the shell precursor reactivities and reaction conditions, non-blinking (or at least very low blinking) CdSe/CdS core/shell QDs with thinner shells were reported.[20]

Depending on the bandgaps and the relative position of electronic energy levels of the involved semiconductors, the shell can have different functions in core/shell QDs. Figure 1.4 provides an overview of the band alignment of the bulk materials, which are commonly used in QD synthesis. Three classes can be distinguished as demonstrated in figure 1.4.[13] In type-I, the bandgap of the shell material is larger than that of the core and both electrons and holes are confined in the core. In type II, the bandgap of the shell material is smaller than that of the core and depending of the thickness of the shell, the holes and electrons are separated between core and shell. In quasi-type II, either the valence-band edge or the conduction-band edge of the shell material is located in the

bandgap of the core, so that one charge carrier can be confined in the core and the other can delocalize between core and shell. The bulk band gaps of various QDs are given in figure 1.4b.

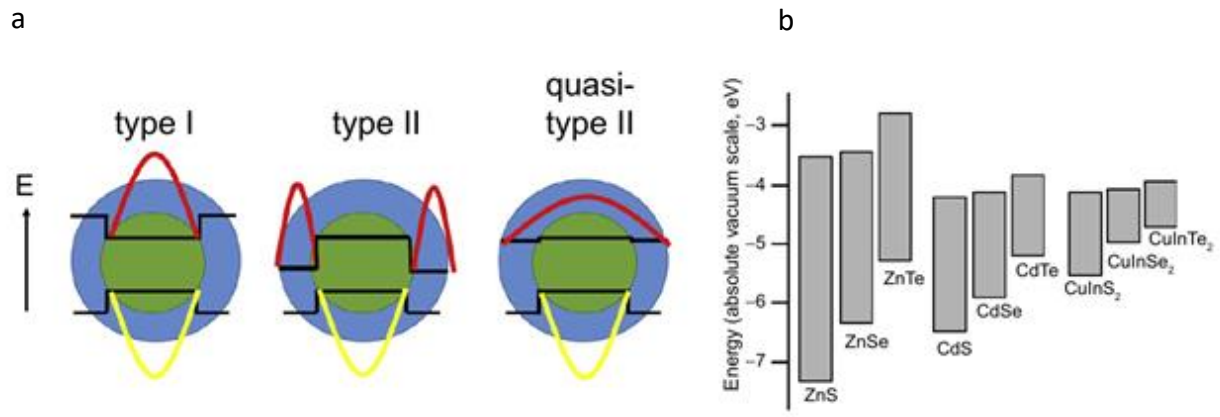

Figure 1.4. (a) Comparison of type I, type II and quasi-type II core/shell QDs. (b) The relative band gaps and band edge offsets between different QD materials. The shaded region is the band gap, so that the lower limit of the shaded region represents the valence band edge and the upper limit of the shaded region represents the conduction band edge. Image is modified from ref. 13.

1.1.3. $CuInE_2$ QDs

Since the early reports for synthesis of QDs, there have been tremendous work focusing on synthesis procedures, structural and optoelectric characterization for QDs.[10, 23] Especially in the case of binary materials, such as II−VI[24-28] or IV−VI[29-33] semiconductors, a vast amount of synthetic procedures allowing for precise size and shape control has been developed and a number of studies were conducted in recent years, which shed light on the underlying reaction mechanisms of the nanocrystals formation and growth. The excellent and precisely controllable optical properties of Cd and Pb-based nanocrystals have made them great types of QDs for fundamental studies. However, because II−VI and IV−VI semiconductors usually contain the highly toxic heavy metals of cadmium, mercury or lead, their large scale applications are greatly limited. Thus, a great number of studies has been carried out focusing on other types of QDs with less toxic

materials but possessing similar optical properties.[34] Copper indium disulfide $CuInS_2$ (CIS), for instance, is a direct semiconductor with a bulk bandgap of 1.45 eV, high extinction coefficient in the visible spectral range, exceptional radiation hardness, and pronounced defect tolerance.[35-39] Therefore, increasing activity in the field of the colloidal synthesis of CIS QDs has been observed in the hope to develop alternative nanocrystalline materials for applications in solar energy conversion, photodetectors, light-emitting devices, photocatalysis, or biomedical applications.[37] The Bohr exciton radius of CIS is 4.1 nm, thus quantum confinement effects can be observed in CIS nanocrystals up to a size of about 8 nm. By changing the size of CIS QDs, their absorption and emission can be tuned from the visible spectrum up to the near infrared.[39] In comparison with the prototypical II-VI QDs, some important fluorescent properties of I-III-IV QDs are presented in table 1.[36]

Table 1. Comparison in fluorescent properties of II-VI and I-III-IV QDs.

Properties	**II-VI QDs**	**I-III-VI QDs**
Spectral tunable window	UV-visible and NIR	UV-visible and NIR
PLQYs	> 50%	>50%
FWHM	25-35 nm	80-120 nm
Stoke shifts	< 100 meV	200-300 meV
PL lifetime	~ 20 ns	100-300 ns

Bulk CIS has a chalcopyrite structure, but CIS QDs have been reported to crystallize in three distinct crystal structures: chalcopyrite (CP), zinc blende (ZB), and wurtzite (WZ) (panels a, b, and c of figure 1.5, respectively).[38] The microstructure of CP has been well-studied and has a significant impact on the optoelectronic properties of CIS QDs with this structure. CP $I–III–VI_2$ materials exhibit cation ordering (Figure 1.5a) with each S atom surrounded by two In and two Cu

atoms. The different bond lengths ($R_{Cu-S} \neq R_{In-S}$) cause anion displacement from a close-packed arrangement, leading to a tetragonal distortion of the crystal lattice. The structural complexity of I−III−VI_2 CP semiconductors results in a lower band gap energy and an abundance of intrinsic defects, in comparison to the II−VI ZB analogues.

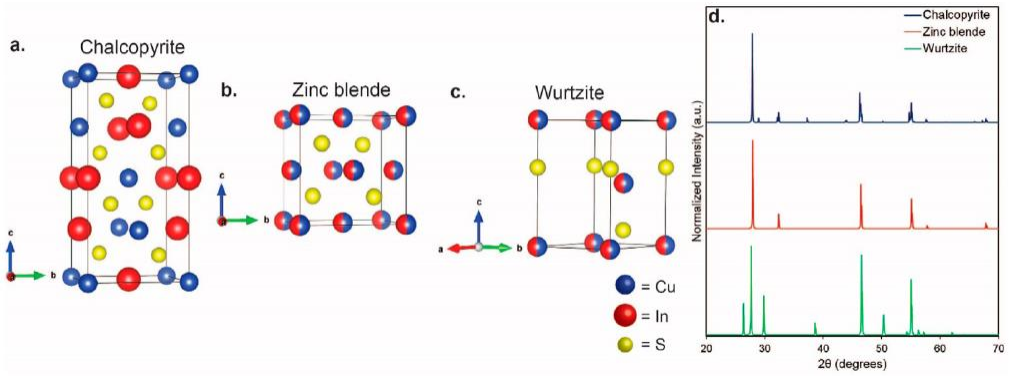

Figure 1.5. Crystal structures of CIS QDs of (a) Chalcopyrite; (b) Zinc blende; (c) Wurtzite; (d) XRD patterns of chalcopyrite, zinc blende and wurtzite. Image is modified from ref. 28.

Over the past several years, even though synthetic developments for CIS QDs have been substantially refined in order to decrease ensemble size, shape, and composition distributions, a sharp first absorption transition has not yet been observed and emission bands have remained broad. Therefore, the exceptionally broad emission bands and essentially featureless absorption spectra of colloidal CIS QDs cannot be explained by the heterogeneity of their size, shape and composition, as is the case for binary II-VI and IV-VI QDs.[40] Furthermore, recent single-QD measurements have shown that the PL fwhm of single CIS QD is only slightly narrower than that of the ensemble (190−270 meV vs 300−400 meV, respectively),[41] indicating that the broad spectral bandwidths (and likely also the large Stokes shifts) of CIS QDs must originate from the intrinsic characteristics of individual QDs.

To date, several models have been proposed to explain the intriguing characteristics of the radiative recombination in CIS QDs, including donor−acceptor pair recombination (figure 1.6a);

recombination in which only one of the carriers is localized – either the electron (figure 1.6b) or the hole (figure 1.6c); and the exciton fine-structure model (Figure 1.6d).

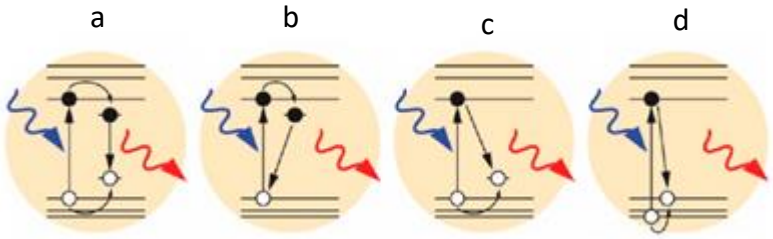

Figure 1.6. Schematic representation of the different mechanisms proposed for the exciton radiative recombination in $CuInS_2$ QDs. (a) Donor−acceptor pair recombination. (b) Localized electron recombines with delocalized valence band hole. (c) Delocalized conduction band electron recombines with localized hole. (d) Exciton fine-structure: absorption transition occurs to a higher-energy hole state while emission takes place from a lower-energy hole state. Image is modified from ref. 29.

Recently, many studies have agreed that the radiative recombination of a delocalized conduction band electron with a localized hole is the most convincing mechanism that explains all the observed PL characteristics for CIS QDs (i.e. broad PL bands with size-dependent spectral positions but size-independent bandwidths, large and size-independent Stokes shift, long radiative lifetimes and multiexponential PL decays).[40] It was concluded by both Knowles et al.[42] and Rice et al.[43] that radiative recombination requires Cu^{2+}-centers, but there is still a question whether Cu^{2+} already exists prior to photoexcitation or if it is formed as a result of oxidization of Cu^{+} by localization of the photogenerated valence band hole.[44-45] Not only is the formal charge of copper ions in the QDs ground state still under debate, but also the nature of the Cu-centers at which radiative recombination takes place. The Cu-center involved may be a Cu^{+} ion with the intrinsic CIS crystalline surrounding (figure 1.7b), or a Cu-related defect (for example, a Cu^{2+} ion neighboring a Cu vacancy or a Cu^{+} ion in an antisite defect, figure 1.7d).[40]

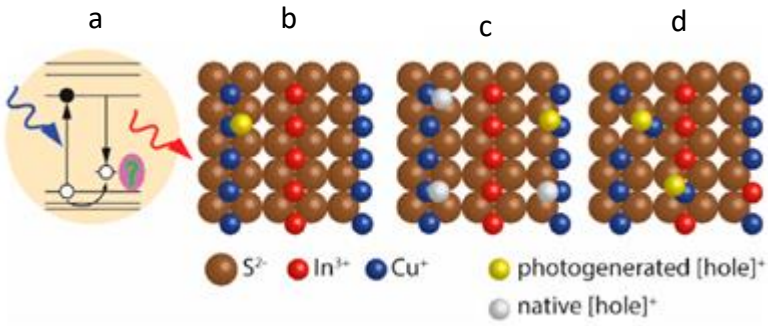

Figure 1.7. (a) Recombination of a delocalized conduction band electron with a localized hole. The green question mark highlights the remaining question on the nature of the hole-localization center. (b–d) Proposed hole-localization centers: (b) Photogenerated hole localizes on a regular Cu^{+} ion. (c) Photogenerated hole localizes on a Cu^{+} ion, and there are also native holes present (i.e., Cu^{2+} ions). (d) Photogenerated hole localizes on Cu^{+}-related native defects. Image is modified from ref. 29.

1.2. Super-resolution microscopy

1.2.1. Breaking the diffraction limit of light

An optical microscope is a lens system that produces a magnified image of a small object. Through this lens system, light rays from a point source converge to a single point at the image plane. However, because of the wave nature of the diffracted light, the image of the point source blurs into an Airy disk. An Airy disk is the region enclosed by the first minimum of the airy pattern and contains approximately 84 percent of the luminous energy, as depicted in figure 1.[46] The three-dimensional (3D) intensity distribution of the Airy disk is called the point spread function (PSF). The size of the PSF determines the resolution of the microscope: two points reside within the full width at half-maximum (FWHM) of the PSF will be difficult to resolve because their images overlap substantially. Thus, image resolution is the smallest distance at which the two points can still be seen as separate entities.

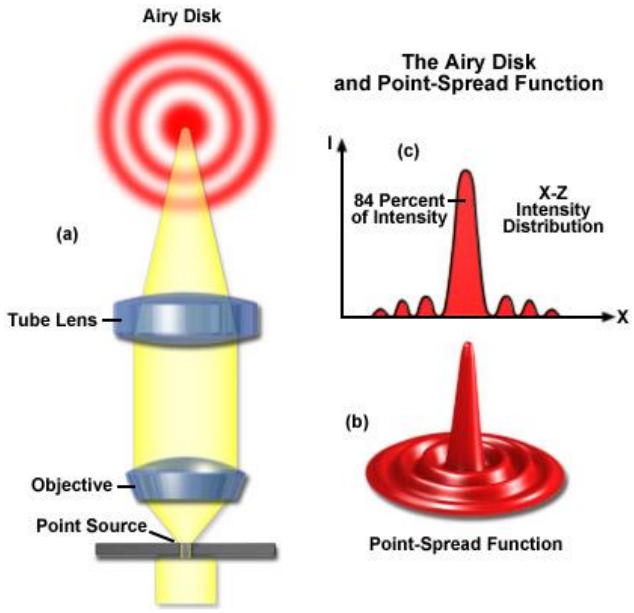

Figure 1. (a) The formation of an Airy disk due to the diffraction of light. (b) PSF is a 3D intensity of an Airy disk. (c) 84% of intensity enclosed within the first minimum of an airy pattern. Image is modified from ref.1.

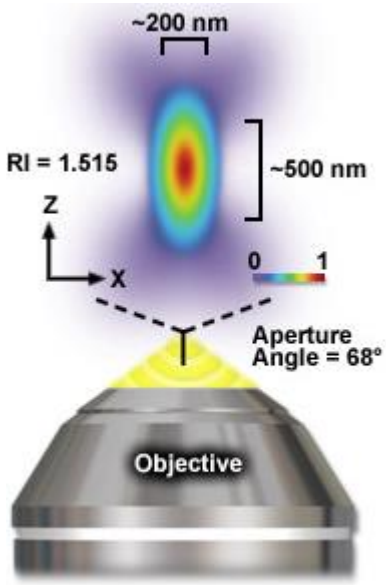

Figure 2. The PSF of a common oil immersion objective with numerical aperture (NA) = 1.40, showing the focal spot of 400 nm light in a medium with a refractive index n = 1.515. The lateral and axial resolutions are 200 nm and 500 nm, respectively. Image is modified from ref.1.[46]

The formal expressions presented by Abbe in 1882 for lateral and axial resolution in the optical microscope are:

$$\text{Resolution}_{x,\,y} = \lambda/2(n.\sin(\alpha)) \qquad \text{Resolution}_{z} = 2\lambda/(n.\sin(\alpha))^2 \qquad \text{(Eq. 1.5)}$$

where λ is the wavelength of light (excitation in fluorescence), n represents the refractive index of the imaging medium, and the combined term n.sin(α) is known as the objective numerical aperture (NA). These equations were later refined by Lord Rayleigh in 1896 to give the Rayleigh criterion, defined as the shortest distance at which two-point emitters can be distinguished as separate objects: R = 0.61λ/NA. Therefore, the theoretical resolution limit at the shortest practical excitation wavelength (approximately 400 nanometers) is around 200 nanometers in the lateral dimension and approaching 500 nanometers in the axial dimension when using an objective having a numerical aperture of 1.5 (figure 2).

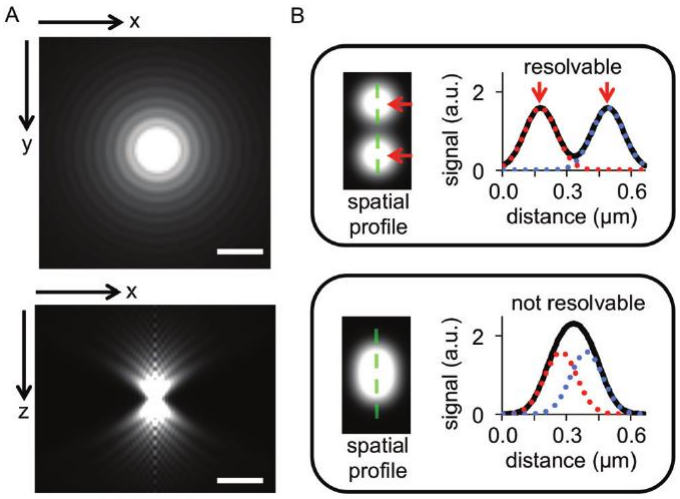

Figure 3. PSF and the resolution limit: (A) representative PSF profile for a wide-field or TIRF microscope viewed in the xy-plane (scale bar 200 nm) and xz-plane (scale bar 600 nm); (B) two particles at resolvable and unresolvable distances as seen in a microscope, red arrows demonstrate when the centers of the particles are resolvable, green line is showed as the intensity profile, dotted red and blue lines correspond to the profile of the upper and lower particles, blackline to the summed profile of both particles.[47]Image is modified from ref.2.

Thus, structures that lie within 200 nanometers cannot be resolved in the lateral plane using either a widefield or confocal fluorescence microscope (figure 3).[47] As many subcellular structures have features much smaller than this size—including microtubules, actin fibers, ribosomes, transport

vesicles, and the intramembrane organization of organelles, a microscopic technique that can be both nondestructive and achieve nanometer resolution is highly desirable for biological research. Over the past few decades, there are many new imaging techniques have been introduced that can break the diffraction limit. It is clear that a short wavelength light source is able to produce a high-resolution image (Eq.1.5). In 1931 M. Knoll and E.A.F. Ruska invented electron microscope (EM) which is a very powerful imaging tool to visualize structures much smaller than 200 nm.[48] The electron beam plays a role of forming images of the specimen objects just similar to the light beams in light microscopy. It provides a resolution under 1 nm because of the short wavelength of the electron beam.[49] However, EM has several practical issues that limit its usage in biological imaging. The issues come from the substantially high energetic electron beam carries electron charges, which as a result, damage or alter samples, requires a fixed, dehydrated and thin section sample to be imaged in an extremely high vacuum. Therefore, EM is not suitable for live imaging and multi-color imaging for biological samples. Besides the method of shortening the wavelength to improve spatial resolution, near-field scanning microscopy (NSOM) has also been demonstrated to address the diffraction problem by placing the imaging aperture close (within one wavelength of light) to the sample, to obtain sub-diffraction resolution before the light spatially diverges.[50-51] However, due to the need for the sample to be in the near field, this method is limited to the very surface of a sample. On the other hand, far-field optical super-resolution microscopies have also been rapidly developed since the first inventions occurred in the 1980s. These innovations can be divided into three types. One of the strategies is based on increasing the effective NA of an optical system to enhance the resolution. For instance, 4Pi-microscopy proposed by Stefan Hell who used two opposing objective lenses for sample illumination by two coherent laser beams, and achieved remarkable improvement in axial resolution by a factor of seven.[52] A similar approach, but with

an additional illumination path named I^5M microscopy was later reported with five to seven fold improvement in axial resolution compared to conventional microscopy.[53] However, these axial interferometric techniques provided very little improvement in the lateral resolution (as also can be seen from Eq.1.5), because improving the effective NA will improve axial resolution much more than lateral resolution. Another type of resolution enhancement is based on pattern illumination of samples. For example, in 1994 Stimulated Emission Depletion (STED) method was developed by Stefan W. Hell and Jan Wichmann,[54] which suppresses the fluorescence emission from the probes located off the center of the excitation by illuminating them with an extra annular laser beam after a normal excitation laser beam, causing stimulated emission in these regions upon reaching their saturation intensity. In this method, only fluorophores at the center of the donut-shaped beam remain fluorescent, resulting in an extremely small fluorescence area (figure 4).[55] With STED depletion, a smaller effective PSF size is obtained in the expression:

$$\Delta_{eff} \approx \Delta/(1 + I/I_s)^{1/2} \qquad \text{(Eq. 1.6)}$$

where Δ refers to the diffraction-limit size of PSF, I is the peak intensity of the donut shape beam, and I_s is the saturation intensity of fluorophores. In cases where I equals zero, equation 1.6 reduces to the Abbe diffraction limit. Conversely, when I is much greater than the fluorophore saturation intensity (i.e. the value of the square root increases), the PSF becomes very narrow and super resolution is achieved. For example, when I/I_s equals 100, the resolution improves by ten-fold. Even though there is no theoretical resolution limit according to this formula, in practice photodamage of the sample restricts the depletion light intensity at a safe value, particularly for biological samples. Typical resolution in biological samples using STED is $\sim$ 50 nm.[56]

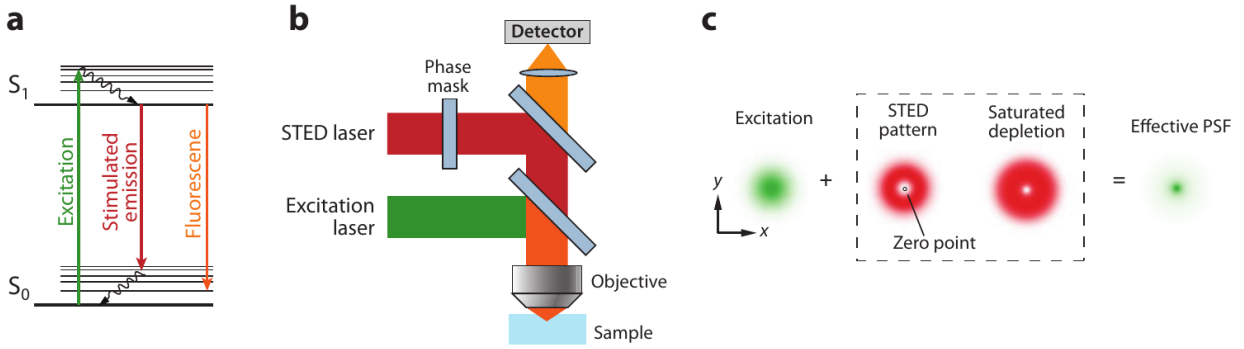

Figure 4. The principle of stimulated emission depletion (STED) microscopy. (a) The process of stimulated emission. A ground state (S_0) fluorophore can absorb a photon from the excitation light and jump to the excited state (S_1). Spontaneous fluorescence emission brings the fluorophore back to the ground state. Stimulated emission happens when the excited-state fluorophore encounters another photon with a wavelength comparable to the energy difference between the ground and excited state. (b) Schematic drawing of a STED microscope. The excitation laser and STED laser are combined and focused into the sample through the objective. A phase mask is placed in the light path of the STED laser to create a specific pattern at the objective focal point. (c) In the xy mode, a donut-shaped STED laser is applied with the zero point overlapped with the maximum of the excitation laser focus. With saturated depletion, fluorescence from regions near the zero point is suppressed, leading to a decreased size of the effective PSF. Image is modified from ref. 10.

Another microscopic technique using saturation process for super-resolution imaging is saturated structure illumination microscopy (SSIM).[57] In this method, the illumination beam is shaped by a diffraction grating to create a sinusoidal-type illumination pattern directly in the sample. A series of images is then acquired while varying the position and rotation of this pattern. Computational reconstruction methods then yield a super-resolution image by exploring the additional frequency information extracted from the acquired images. This method virtually doubles the NA of the system, hence doubling the lateral resolution to around 100 nm (figure 5a).

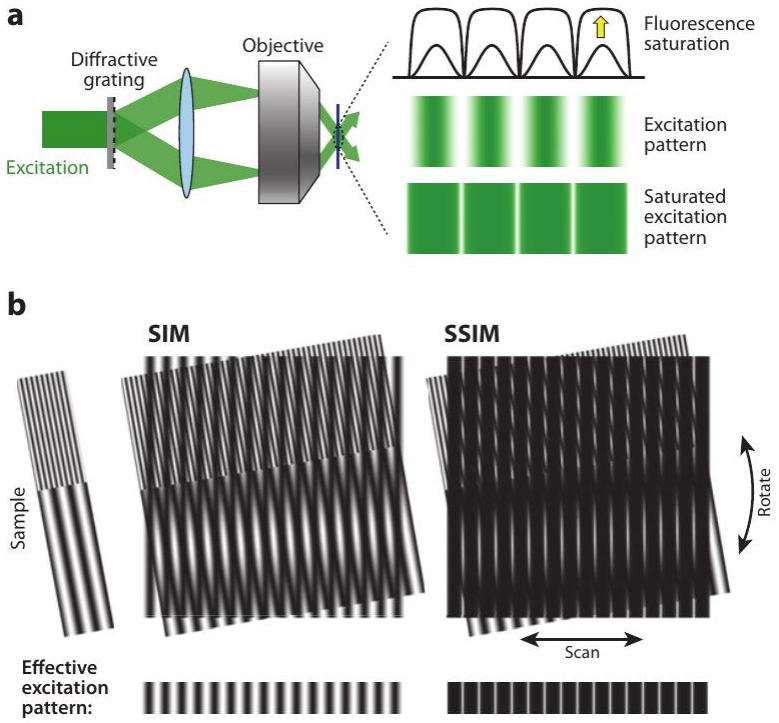

Figure 5. The principle of saturated structured-illumination microscopy (SSIM). (a) The generation of the illumination pattern. The excitation beam is devided into two by placing a diffractive grating in the excitation path. Their interference after emerging from the objective and reaching the sample creates a sinusoidal illumination pattern with alternating peaks and zero points. (b) Resolving fine structures with structured-illumination microscopy (SIM) and SSIM. When a sinusoidal illumination pattern is applied to a sample, a moiré pattern at a significantly lower spatial frequency than that of the sample can be generated and imaged by the microscope (SIM panel, lower part). in the moiré pattern (SIM panel, upper part). SSIM introduces a high-frequency component into the excitation pattern, allowing features far below the diffraction limit to be resolved. Imaged is modified from ref. 10

In 2005, Gustafsson further improved the resolution for this imaging technique using nonlinear structured illumination.[58] Under intense illumination, the emission intensity can depend nonlinearly on the illumination intensity. This nonlinearity causes the illumination pattern to saturate at the high-intensity illumination region as indicated in figure 5b. With high illumination intensity, the effective illumination pattern in figure 5b contains harmonics with spatial frequencies that are higher than the original illumination spatial frequency. These higher spatial frequency

components have provided a resolution of 50 nm on bright and photostable samples,[58] 3D cell imaging[59] and 3D live cell imaging.[60]

Another type of super resolution microscopy is single molecule localization microscopy, which include photoactivated localization microscopy (PALM)[61] and stochastic optical reconstruction microscopy (STORM).[62] The main concept of this imaging technique is to label the imaging sample with fluorescent probes that can switch between a fluorescent and a dark state. In this approach, molecules within a diffraction limited region can be activated at different time points so that they can be individually imaged, localized, and subsequently deactivated. The process is repeated with thousands of cycles through wide-field imaging, so that there are enough coordinates from many fluorophores that can be mapped and a super-resolution image subsequently reconstructed.

Super-resolution imaging methods are able to achieve substantially high resolution (even down to several nm). Figure 6 summarizes the approximate resolution of some widely used microscopy. This significance of far-field super-resolution imaging techniques were recognized when the 2014 Nobel Prize for Chemistry was awarded to Eric Betzig, Stefan Hell and William Moerner for their pioneering contributions to this field.

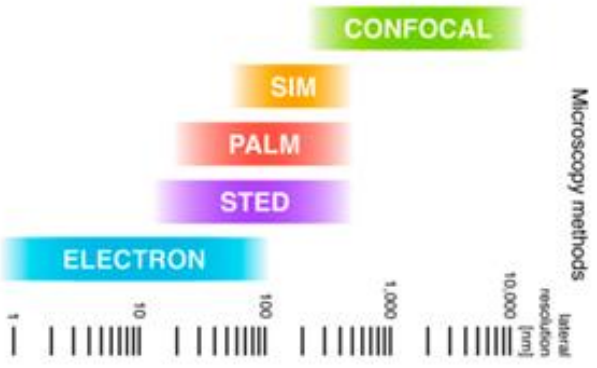

Figure 6. Comparison of the spatial scales at which different microscopy techniques. Image is modified from ref.[63]

1.2.2. Single molecule localization microscopy

The principle of single molecule localization super resolution imaging relies on a combination of two capabilities: the localization of single fluorophores with very high precision and imaging of sparse subsets of photoswitchable fluorescent labels in time.

Because of the diffraction of light, the image of a single molecule captured through a conventional optical microscope is much larger than the molecule itself and is often referred to as PSF. When the molecule is isolated, it is possible to determine its position with very high precision by finding the centroid of its PSF as illustrated in figure 7.[64-66]

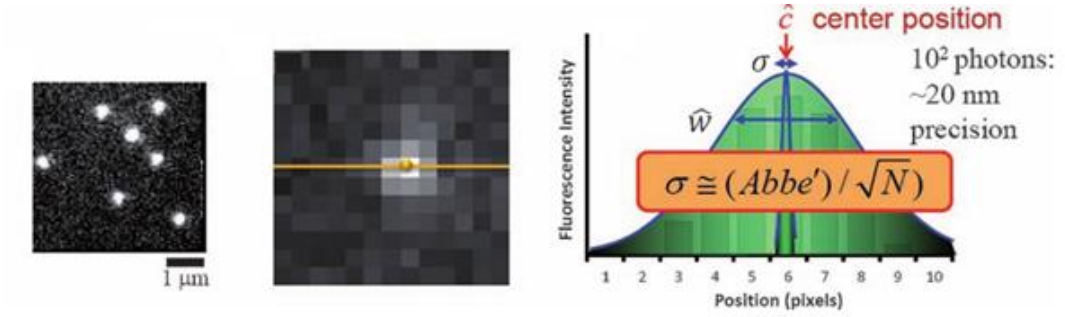

Figure 7. The basic concept of localization of single molecule. (left) wide field image of fluorophores. (middle) wife field image of single fluorophore. (right) PSF and Gaussian fitting to find the center position with very high precision of the single fluorophore. Image is modified from ref. 21.

The localization precision mainly depends on the number of photons emitted by the molecule and subsequently captured by the microscope, background noise, and pixel size.[64] The localization precision is described as:

$$\sigma^2 = s^2/N + a^2/(12N) + 8\pi s^2 b^2/(N^2 b^2) \qquad \text{(Eq. 1.7)}$$

where s is the standard deviation (SD) of the PSF, a is the pixel size in the image, b is the background noise, and N is the number of photons collected. Based on equation 1.7, the higher the number of photons emitted by a fluorophore/collected by the microscope, the more precise the

localization accuracy. For example if a fluorophore emits 100 photons that are all captured by the microscope, the localization precision of that fluorophores can approach 20 nm.

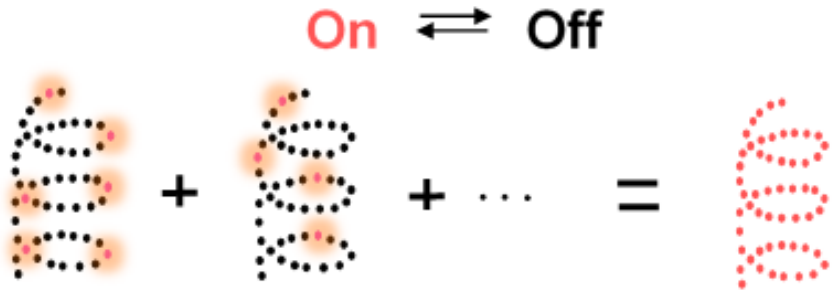

Figure 8. The principle of single molecule localization super resolution imaging. In one cycle of imaging, just a small subset of fluorophores is activated. Their positions can be localized with a high precision. Then these fluorophores are turn off. Another subset of fluorophores is activated and the imaging cycle is repeated many times so that there are enough positions of fluorophores to reconstruct an image with resolution much better than diffraction limit.

Although the ability to precisely localize single molecules is powerful by itself, this concept alone is not enough to break the diffraction limit when imaging densely-labeled samples. The resolving power of an optical microscope is dependent on the ability to distinguish each fluorescent molecule in close proximity, which is still limited by diffraction since the PSF of these molecules will overlap when they are closer than the diffraction limit. Therefore, to transfer the single-molecule localization concept to super-resolution imaging, it is important to be able to actively control the density of fluorophores that are fluorescent at any point in time (the binning time of the detector) to avoid overlapping fluorescent signals. This active control of fluorophore density was made possible by the discovery of photoswitchable probes.[61, 67]

Photoswitchable probes can be cycled between bright and dark states (or between two different spectral colors) using illumination. In particular, the majority of probes can be “switched off” to allow only a very small fraction of them to be in the fluorescent state. Even in a densely-labeled sample, the signals of the subset of activated probes will no longer overlap and therefore their positions can be localized with high precision. Through many cycles of activation and deactivation,

the positions of all the probes can be precisely determined, and these positions can then be used to reconstruct a high-resolution image (figure 8). Two ground breaking studies for single molecule super resolution microscopy from Betzig who used photoactivatable fluorescent protein (PA-FP) molecules for PALM[61] and Zhuang used Cy3-Cy5 dye pair for STORM showed substantial improvements in spatial resolution.[62]

The spatial resolution in single molecule localization microscopy depends on several factors. First, the precision by which each molecule can be localized, known as localization precision, which is described above. Second, spatial resolution depends on the labeling density. Low-labeling densities typically cause continuous structures to appear discontinuous, resulting in a loss of detail. The effects of the labeling density on the spatial resolution can be quantified by the Nyquist criterion,[68] which states that structural features smaller than twice the fluorophore-to-fluorophore distance cannot be reliably discerned. And the smallest resolvable feature size is determined as followed equation:

$$\Delta_{Nyquist} = 2/N^{1/D} \qquad \text{(Eq. 1.8)}$$

where N is the labeling density calculated as the number of localizations per unit area or volume, and D is the dimension of the structure to be imaged (2 for twodimensional (2D) and 3 for three-dimensional (3D) imaging). According to equation 1.8, to achieve a 20-nm 2D (or 3D) resolution, an extremely high labeling density of 10^4 per μm^2 (or 10^6 per μm^3) is required in general. This requires that only about 1 in several thousand fluorophores be active at any (binning) time point to obtain a super-resolution image.

1.2.2.1. Fluorescent probes for single molecule localization microscopy

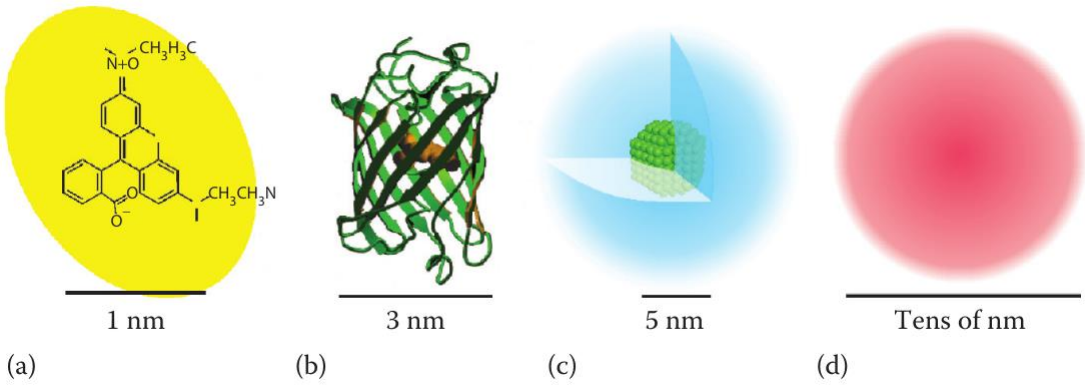

Figure 9. Common types of fluorophores in the bioimaging are (a) organic dye molecules (tetramethylrhodamine (TMR) is shown), (b) fluorescent proteins (GFP is shown), (c) quantum dots, and (d) dyed polymer particles. Image is modified from ref. 24.

Several fluorophore classes have emerged as candidates for labeling subcellular structures in photoactivated single-molecule localization microscopy. These include genetically encoded proteins, small-molecule synthetic dyes, quantum dots, and dyed polymer particles (figure 9).[69] Each class of probe has its particular strengths and weaknesses, but no single class or individual fluorophore can combine all the preferred characteristics of an ideal probe for single molecule super resolution microscopy.[55, 70-74] The principal property for fluorescent probes in this class is that they must be capable of being photoactivated, photoswitched, or photoconverted by light of a specific wavelength so that they can alter their spectral properties for the detection of selected subpopulations.

Among the most desirable characteristics for single-molecule super resolution probes are very high brightness and contrast levels, which are necessary to maximize the number of photons that can be detected per molecule before it photobleaches or reverts to a dark state. Brightness is determined

by the product of the molar extinction coefficient (ε_{abs}) and the fluorescence quantum yield (φ).[75] In addition, these probes should be able to switch between fluorescent and dark state so that in a given binning time, only a small subset of probes are fluorescent.

One of the biggest advantages of fluorescent proteins is that they are genetically encodable and are straightforward for specific cellular structural labelling, such as lysosomes, and mitochondria.[72] Nowadays, the fluorescent proteins family has been expanded to a wide range of derivative products, with a wide range of optical and chemical properties. For example, photoactivatable fluorescent proteins such as PA-GFP that can increase the fluorescence by 100 fold compared to wild type GFP when excited at 488 nm[67]; PA-mcherry has improved pH stability, faster photoactivation and higher contrast;[76] photoconvertible fluorescent proteins such as EosFP, mEosfp, mEos2 can convert from one emission wavelength to another; and photoswitchable fluorescent proteins such as Dronpa, which can switch to an on state after brief illumination at 405 nm and revert to a dark state when illuminated at 488 nm.[72]

Organic dyes have provided an alternative fluorescence labelling solution to fluorescent proteins, in terms of their small structure, high QY (more than 90 %) which results in brighter probes with higher numbers of photons per molecule and good photostability in cellular environments. Dyes are small conjugated organic molecules such as Fluorescein, Quinine, Coumarin, Rhodamine, Cyanines and Oxazines, which are usually 1-5 nm in size. Many advanced biofunctional fluorescent dyes are commercially available and include derivatives from green-color-emitting products such as Carboxyfluorescein, to orange-color-emitting products such as ATTO532, and even red/near IR-color-emitting products such as Rhodamine B, Cy5, Cy7.[55, 62, 70]

For single-molecule localization based super resolution microscopy, such as PALM and STORM, the spatial resolution is limited by the number of photons, as indicated in equation 1.7. PALM or

STORM collects the maximum number of photons emitted from each molecule, and the resolution is determined by the number of photons detected. The number of photons a molecule can emit before it is photobleached (or switched off) varies from molecule to molecule. For example, EosFP used for PALM, can emit ~750 photons per molecule, and the switchable fluorophore pair Cy3–Cy5 used for STORM can provide ~6000 photons per molecule per switching cycle and lasts ~200 switching cycles.[72] Overall, photoswitchable dyes have larger numbers of collected photons per molecule compared with fluorescence proteins. Quantum dots (QDs) offer excellent photostability for long-term imaging (figures 10),[77] and several applications of QDs for super resolution microscopy have been demonstrated (Figure 11).[78-80]

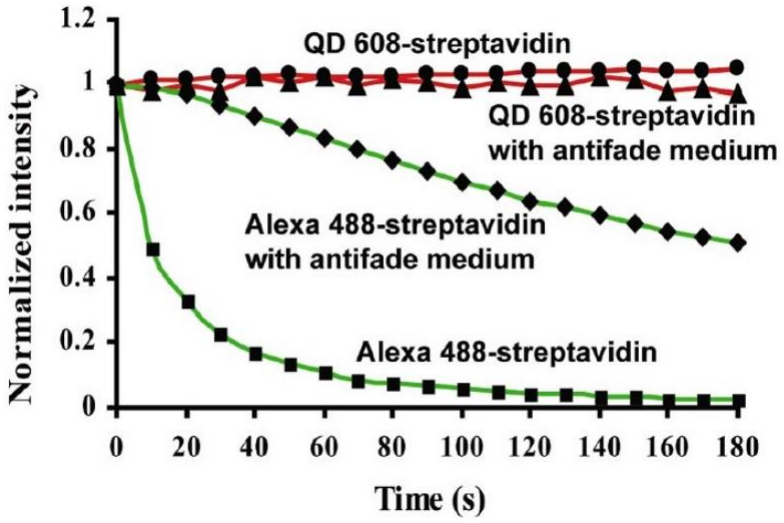

Figure 10. Comparison of photostability between QD and Alexa 488 dye. Image is modified from ref. 32.

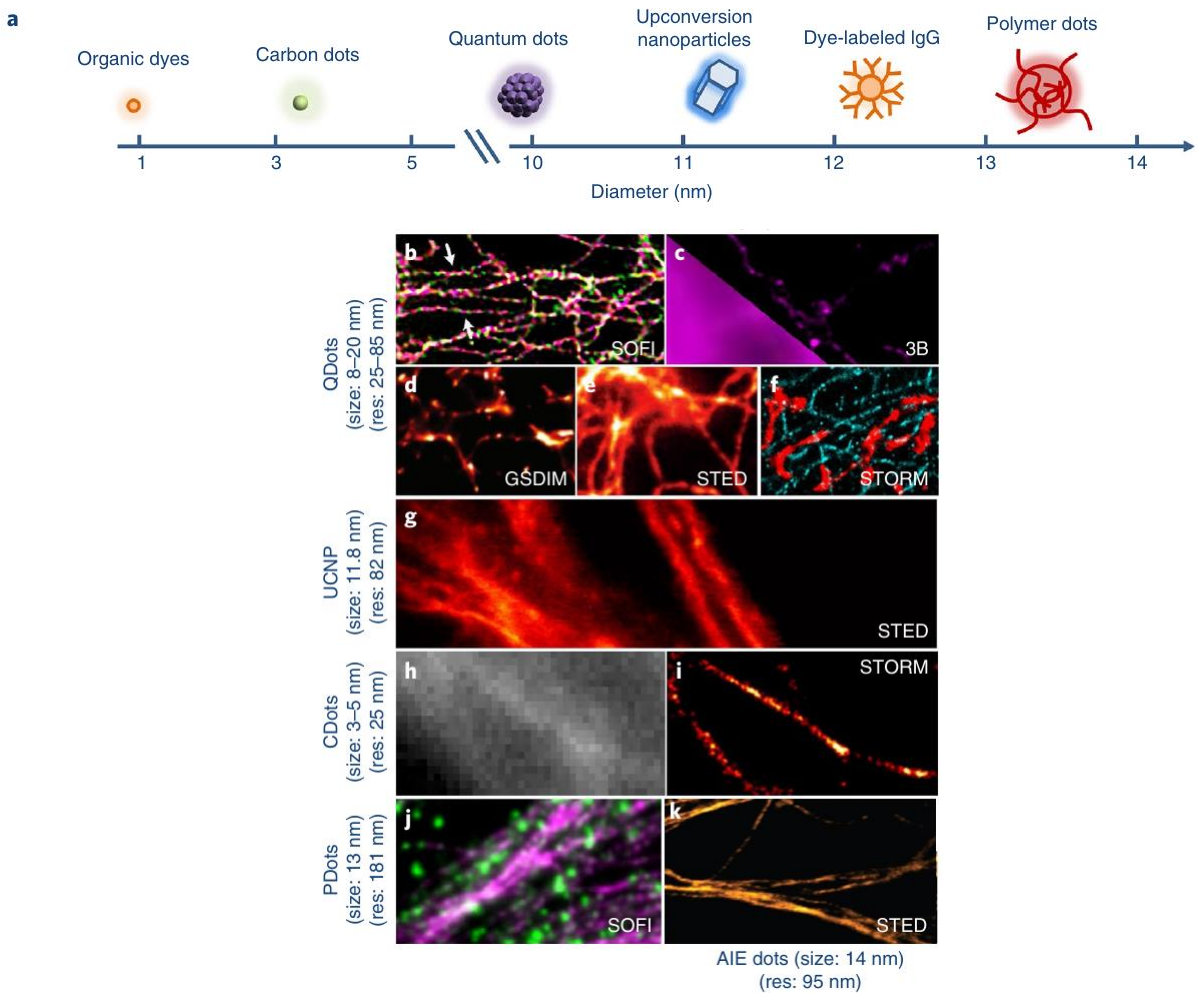

Figure 11. Luminescent nanoparticles used in super-resolution microscopy imaging. a, Illustration of the physical dimensions of dye molecules, carbon dots, quantum dots, upconversion nanoparticles, dye-labeled IgG antibody, and polymer dots used in super-resolution microscopy. b–f, QDots used in super-resolution imaging. b, Multi-color SOFI image of microtubules in HeLa cells. c, 3B microscopy image of microtubules in HeLa cells. d, Ground-state depletion microscopy followed by individual molecule return (GSDIM) image of the microtubular network in mammalian PtK2 cells. e, STED imaging of vimentin fibers in REF cells. f,Two-color STORM imaging of microtubles and mitochondria. g, UCNPs used in STED imaging of microtubules in HeLa cells. h,i, CDots used in wide-field and STORM imaging of microtubules in HeLa cells. j, PDots used in multicolor SOFI microscopy imaging of microtubules in HeLa cells. k, AIE dots used in STED imaging of microtubules in HeLa cells. Image is modified from ref. 29.

Compared to traditional fluorophores, QDs have a broader absorption spectrum and a narrower emission spectrum, which is beneficial for simultaneous multicolor imaging with the same

excitation light.[75] QDs have been estimated to be up to 20 times brighter and 100 times more stable than organic dyes such as rhodamine. However, for specific labeling, QDs must be conjugated to biomolecules that provide binding specificity. While commercial kits and established labeling protocols are widely available for conjugating dyes to biomolecules, conjugating QDs to biomolecules and specific binding of QDs to imaging samples still remains challenging.[72, 74]

QDs represent the first generation of inorganic fluorescent nanoparticles used for fluorescent labeling. Compared with conventional dyes, they have a much larger absorption coefficient, with comparable luminescent quantum yields, and, as a result, have greater brightness. QDs exhibit narrow-band emission (spectral width < 50 nm), and their emission color can be tuned through adjustments to their size (quantum confinement effect), which makes these particles ideal for multicolor imaging applications and a range of super-resolution imaging modes (figure 11). The commercially available CdSe/ZnS QD 705 nm (from Thermo Fisher), CdTe/ZnS QD 700 nm, and CdTe/ZnS QD 720 nm (from PlasmaChem GmbH) are suitable for STED microscopy with spatial resolutions of 85 nm for QD-705-stained microtubule networks in HeLa cells, and 106 nm for vimentin filaments in fibroblasts.[79, 81] The high stability of QDs allows for extended imaging before they are bleached. The QDs blinking-based super-resolution was first reported in 2005 in which the authors used Independent Component Analysis (ICA) to accurately localize two-point fluorophores as a function of their separation.[78] Blinking CdSe QDs have been used to improve spatial resolution with super resolution optical fluctuation imaging (SOFI).[82] Wang et al. introduced quantum dot blinking with three-dimensional imaging (QDB3) technique,[83] in which 3D super-resolution imaging with blinking QDs is achieved by extracting the point-spread function (PSF) of individual QDs by subtracting subsequent frames. Multicolor imaging has also been presented using QDs as probes.[84] Upconversion nanoparticles (UCNPs) represent an entirely new

class of multiphoton probes that rely on high densities of multiphoton emitters in small particles.[85] Each particle contains thousands of doped lanthanide ions that form a network of photon sensitizers and activators, which upconvert near-infrared photons into visible and ultraviolet ones. Because of the large anti-Stokes spectral separation between excitation and emission, these probes are highly useful in background-free and photostable bioimaging.[86] Recent studies reported that thousands of emitters per nanoparticle can be activated by microscopes, resulting in a brightness that makes UCNPs suitable as single-molecule probes.[86] As a result, a low saturation intensity of ~0.19 MW cm^{-2} in upconversion STED microscopy was recorded, with a maximum resolution of 28 nm (λ /36) for optical imaging of single 13-nm UCNPs. High-speed (100 μs dwelling time) super-resolution imaging of cellular cytoskeleton protein structures with a resolution of 80 nm has also been demonstrated (Fig. 11g).

Carbon dots (CDots) with diameter of 2-5 nm have attracted substantial attention as subcellular targeting probes. CDots have different functional groups such as – OH, $–NH_2$, and –COOH on the surface for further conjugation to biomolecules. Recently, a couple of reports introduced biocompatible carbon dots with burst like fluorescent for single molecule localization super resolution imaging of microtubule networks[87] and fixed trout epithelial gill cells.[88]

PDots are particles that consist predominantly of π -conjugated polymers and have been shown to have superior brightness compared with that of conventional QDs.[89] Very small PDots (10 nm or less) were found to be suitable for fluctuation-based super-resolution techniques such as SOFI (Fig. 11j).[90] To functionalize the PDots, an optically inert polymer, poly(styrene-co-maleic anhydride) (PSMA), has been added. The PSMA polymer also generates surface carboxyl groups, which enables specific biomolecular conjugation through biotinylated antibodies. Their small size

confers improved biocompatibility, and they were shown to be able to label a variety of subcellular organelles such as mitochondria, the nuclear envelope, and microtubules.

1.2.2.2. Total internal reflection fluorescence (TIRF)

Background noise is significantly reduced when using TIRF. With this microscopy method, incoming laser light whose incident angle is larger than a critical angle impinges on the glass-water interface and is reflected back away from the interface. However, an evanescent field (which falls off exponentially from the interface) is generated in the aqueous medium

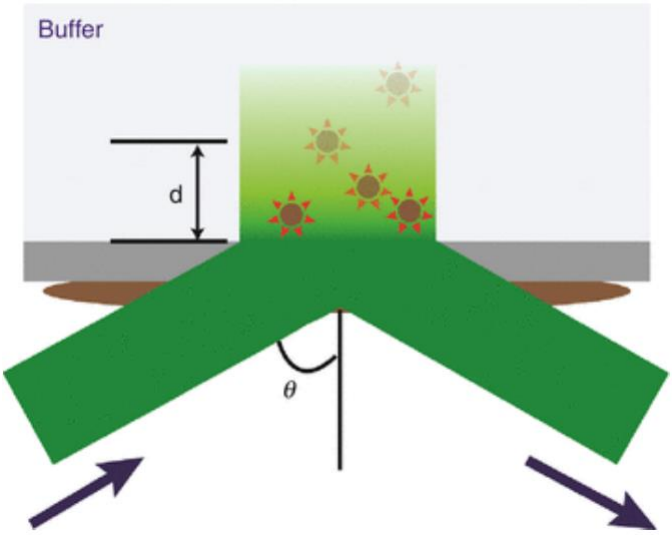

Figure 12. Illustration of TIRF. The laser impinges on the water-glass interface with angle θ, which is over the critical angle. An evanescent field is generated whose intensity exponentially decreases away from the interface. Fluorescent dyes within penetration depth d are excited. The indexes of refraction are all the same for the cover glass (gray), the index-matching immersion oil (brown). Image is modified from ref. 47.

upon reflection of the laser beam, which enters the water through a glass coverslip/slide. Consequently, only fluorophores near the glass-water interface are excited.[91] The 1/e depth varies with the incident excitation light, and is generally about 100 nm. (The index of refraction of water, n_{water} = 1.33; the index of refraction of glass, n_{glass} = 1.518.)

$$\text{Penetration depth } d = \lambda/(4\pi(n^2_{glass}\sin^2\theta - n^2_{water})^{1/2}) \qquad \text{(Eq. 1.9)}^{92}$$

Other samples regions outside of this ~100nm are not excited (figure 12), thereby reducing the background as compared to standard epi-fluorescence microscopy.

1.2.2.3. Labeling density

In super-resolution fluorescence microscopy, because the optical resolution often approaches the distance between adjacent fluorescent probes in a sample, the labeling density could become a limiting factor of the effective spatial resolution. This aspect applies to all super-resolution fluorescence microscopy methods, including STED, RESOLFT, SSIM, as well as STORM/PALM. When the labeling efficiency (fraction of target molecules labeled) of a sample is not sufficient, artifacts can be observed in super resolution images, for example, causing continuous structures to appear discontinuous.[55, 72] The effect of labeling density on the effective resolution can be quantified by the Nyquist criterion as describes above in equation 1.8. For the single-molecule localization approach, too high labeling density can also be disadvantageous because the overlap of fluorophore signals prevents high-precision localization. The optical properties of the fluorophore and the spatial properties of the object being imaged need to be carefully matched to ensure maximum effectiveness of the super-resolution image.

1.2.2.4. Time resolution

The imaging speed of the single-molecule localization approach is limited by the time required to accumulate a fluorophore localization density that is sufficient for a desired resolution given by the Nyquist criterion, as described earlier. Because different subsets of fluorescent probes are localized sequentially, the time resolution of single molecule localization super-resolution imaging is intrinsically slower than conventional microscopy.

The rate of accumulating localization points is limited by the switching kinetics of fluorescent probes and the acquisition rate of the camera. Photoswitchable fluorophores have been reported to exhibit an off-switching time on the order of 1 ms. At this high off-switching/acquisition rate of 1 kHz, probe molecules can be activated at a rate of ~1000 $\mu m^{-2}s^{-1}$ without causing substantial overlap between single-molecule images, giving a Nyquist-limited lateral resolution of about 60 nm at 1 s time resolution for homogenous structures in a 30 μm × 30 μm region.[55] 3D imaging at 60 nm Nyquist resolution in a 30 μm × 30 μm × 3 μm volume can be performed at about 100 s per frame. For biological samples, which are usually heterogeneous structures, a lower number of localizations is typically needed to achieve the specified resolution, and the imaging speed will be even faster.

1.3. Overview of dissertation

My dissertation is comprised of two complete projects which are shown in two chapters, chapter 2 and chapter 3.

Chapter 2: $CuInS_2$-doped ZnS quantum dots obtained via non-injection cation exchange show reduced but heterogeneous blinking and provides insights into their structure-optical property relationships.

The study was carried out in order to shed light on the relationship of structures, elemental composition and photophysics of single particle QDs.

The synthesis started with synthesis of CIS QDs cores which have a quantum yield of 12%. The shelling of CIS with ZnS using different concentration (0.1; 1; 2 and 4 mmol) of zinc stearate $Zn(St)_2$ was used to encapsulate CIS cores, and to improve the optical properties. In the shelling procedure zinc stearate was added to CIS cores at room temperature then the solution was heated

up to 230 C, which is more suitable for large scale production of QDs compared to the current literature methods which involve a dropwise hot injection step.

TEM analysis showed that the resulting QDs are small (8 nm or less) and relatively isotropic. The photoluminescence quantum yields (PL QY) reach almost 70% with emission peaks in the 560-600 nm window, depending on the amount of Zn precursor added. The results indicated an extensive cation exchange of Cu^{x+} (x = 1 or 2) and/or In^{3+} with Zn^{2+} resulting in small $CuInS_2$ 'clusters' within a zinc-blende ZnS lattice which act as the radiative recombination centers in the nanoparticle. Interestingly, and somewhat unexpectedly, higher ensemble photoluminescence quantum yields (PL QY) result when cation exchange is less extensive (~80 % ZnS composition), while a reduction in blinking is observed when ZnS composition exceeds 99%. A wide heterogeneity in blinking behavior from QD-to-QD is evident, especially when 2 and 4 mmol of zinc precursor was used, and a subpopulation statistical analysis shows that the on-state dwell times change from multiexponential (or inverse power law) behavior towards mono-exponential behavior for particles that spend more of their time in the on-state. These results indicate that, as the number of $CuInS_2$ emitting centers is reduced, the number of pathways leading to the off-state decreases, and a model is proposed to relate this behavior to the QD structure. These results provide a novel route towards $CuInS_2$-doped visible-light emitting ZnS QDs with high quantum yield and reduced blinking and provides insight into how the composition of dopant and host matrix affects the radiative recombination mechanisms in single particles.

Chapter 3: Utilization of fast blinking CIS/ZnS QDs as fluorescent probes for single particle localization based super resolution imaging.

In general, highly suppressed or non-blinking QDs are ideal for many applications as mentioned in introduction for QDs. However, for some particular applications including single particle localization super resolution imaging, QDs with burst like fluorescent are needed.

In this chapter, we present a comparison between $CuInS_2$/ZnS (CIS/ZnS) and commercially-available CdSe/ZnS QDs in their blinking behavior, localization precision and super resolution localization imaging. The rationale for this project is that CIS/ZnS QDs are less bright but give burst like fluorescence compared to CdSe/ZnS QDs. Therefore, imaging samples can be labeled with much higher density of CIS/ZnS QDs and reconstructed super resolution images should give more details.

First, Cd-free CIS/ZnS are synthesized similar to those in chapter 2, and then subsequently modified to render them biocompatible. Their surface is specifically functionalized to bind to actin filaments in aqueous solution. The resulting biocompatible QDs are compact (~ 5nm), have relatively high fluorescence quantum yield (~ 30%) and shows burst like fluorescence blinking. Even though CdSe/ZnS QDs showed better localization precision in single QD experiments due to their higher brightness (quantum yield), the faster, burst-like blinking of the CIS/ZnS allowed for a higher labeling density to provide comparable super-resolution precision in actin filaments. The width of the observed actin filaments in the super resolution images shows a ~4.5 fold improvement over the diffraction-limited images acquired by conventional TIRF images. Furthermore, the higher labeling density of CIS/ZnS allows for more imaging information along the length of the filament compared to CdSe/ZnS. These results demonstrate that CIS/ZnS QDs can be a powerful candidate in the toolbox of fluorescent probes for single molecule localization microscopy.

1.4. References

1. Klimov, V. I., Nanocrystal Quantum Dots. **2010**.

2. Brus, L., Electronic wave functions in semiconductor clusters: experiment and theory. *The Journal of Physical Chemistry* **1986,** *90* (12), 2555-2560.

3. Ekimov, A. I., Onushchenko, A. A., Tzehomski, V. A., Excitonic absorption by CuCl mirocrystals in a glass matrices. *Sov. Phys. Chem. Glass* **1980,** *6*, 511-512.

4. Rossetti, R.; Nakahara, S.; Brus, L. E., Quantum size effects in the redox potentials, resonance Raman spectra, and electronic spectra of CdS crystallites in aqueous solution. *The Journal of Chemical Physics* **1983,** *79* (2), 1086-1088.

5. Yang, Z.; Fan, J. Z.; Proppe, A. H.; Arquer, F. P. G. d.; Rossouw, D.; Voznyy, O.; Lan, X.; Liu, M.; Walters, G.; Quintero-Bermudez, R.; Sun, B.; Hoogland, S.; Botton, G. A.; Kelley, S. O.; Sargent, E. H., Mixed-quantum-dot solar cells. *Nature communications* **2017,** *8* (1), 1325.

6. Mandal, G.; Darragh, M.; Wang, Y. A.; Heyes, C. D., Cadmium-free quantum dots as time-gated bioimaging probes in highly-autofluorescent human breast cancer cells. *Chemical communications* **2013,** *49* (6), 624-6.

7. Bruns, O. T.; Bischof, T. S.; Harris, D. K.; Franke, D.; Shi, Y.; Riedemann, L.; Bartelt, A.; Jaworski, F. B.; Carr, J. A.; Rowlands, C. J.; Wilson, M. W. B.; Chen, O.; Wei, H.; Hwang, G. W.; Montana, D. M.; Coropceanu, I.; Achorn, O. B.; Kloepper, J.; Heeren, J.; So, P. T. C.; Fukumura, D.; Jensen, K. F.; Jain, R. K.; Bawendi, M. G., Next-generation in vivo optical imaging with short-wave infrared quantum dots. *Nature Biomedical Engineering* **2017,** *1* (4), 0056.

8. Manders, J. R.; Qian, L.; Titov, A.; Hyvonen, J.; Tokarz-Scott, J.; Xue, J.; Holloway, P. H., 8.3: Distinguished Paper: Next-Generation Display Technology: Quantum-Dot LEDs. *SID Symposium Digest of Technical Papers* **2015,** *46* (1), 73-75.

9. Nirmal, M.; Dabbousi, B. O.; Bawendi, M. G.; Macklin, J. J.; Trautman, J. K.; Harris, T. D.; Brus, L. E., Fluorescence intermittency in single cadmium selenide nanocrystals. *Nature* **1996,** *383*, 802.

10. Efros, A. L.; Nesbitt, D. J., Origin and control of blinking in quantum dots. *Nature Nanotechnology* **2016,** *11* (8), 661-671.

11. Efros, A. L.; Rosen, M., Random Telegraph Signal in the Photoluminescence Intensity of a Single Quantum Dot. *Physical review letters* **1997,** *78* (6), 1110-1113.

12. Efros, A. L., Almost always bright. *Nature materials* **2008,** *7* (8), 612-613.

13. Heyes, C. D., Chapter 4 - Quantum dots in single molecule spectroscopy. In *Spectroscopy and Dynamics of Single Molecules*, Johnson, C. K., Ed. Elsevier: 2019; pp 163-228.

14. Kuno, M.; Fromm, D. P.; Johnson, S. T.; Gallagher, A.; Nesbitt, D. J., Modeling distributed kinetics in isolated semiconductor quantum dots. *Physical Review B* **2003,** *67* (12), 125304.

15. Shimizu, K. T.; Neuhauser, R. G.; Leatherdale, C. A.; Empedocles, S. A.; Woo, W. K.; Bawendi, M. G., Blinking statistics in single semiconductor nanocrystal quantum dots. *Physical Review B* **2001,** *63* (20), 205316.

16. Heyes, C. D.; Kobitski, A. Y.; Breus, V. V.; Nienhaus, G. U., Effect of the shell on the blinking statistics of core-shell quantum dots: A single-particle fluorescence study. *Physical Review B* **2007,** *75* (12), 125431.

17. Tang, J.; Marcus, R. A., Diffusion-Controlled Electron Transfer Processes and Power-Law Statistics of Fluorescence Intermittency of Nanoparticles. *Physical review letters* **2005,** *95* (10), 107401.

18. Frantsuzov, P. A.; Marcus, R. A., Explanation of quantum dot blinking without the long-lived trap hypothesis. *Physical Review B* **2005,** *72* (15), 155321.

19. Jin, S.; Song, N.; Lian, T., Suppressed Blinking Dynamics of Single QDs on ITO. *ACS nano* **2010,** *4* (3), 1545-1552.

20. Chen, O.; Zhao, J.; Chauhan, V. P.; Cui, J.; Wong, C.; Harris, D. K.; Wei, H.; Han, H. S.; Fukumura, D.; Jain, R. K.; Bawendi, M. G., Compact high-quality CdSe-CdS core-shell nanocrystals with narrow emission linewidths and suppressed blinking. *Nature materials* **2013,** *12* (5), 445-51.

21. Chen, Y.; Vela, J.; Htoon, H.; Casson, J. L.; Werder, D. J.; Bussian, D. A.; Klimov, V. I.; Hollingsworth, J. A., "Giant" multishell CdSe nanocrystal quantum dots with suppressed blinking. *Journal of the American Chemical Society* **2008,** *130* (15), 5026-7.

22. Omogo, B.; Gao, F.; Bajwa, P.; Kaneko, M.; Heyes, C. D., Reducing Blinking in Small Core-Multishell Quantum Dots by Carefully Balancing Confinement Potential and Induced Lattice Strain: The "Goldilocks" Effect. *ACS nano* **2016,** *10* (4), 4072-82.

23. Reiss, P.; Protière, M.; Li, L., Core/Shell Semiconductor Nanocrystals. *Small* **2009,** *5* (2), 154-168.

24. Danek, M.; Jensen, K. F.; Murray, C. B.; Bawendi, M. G., Synthesis of Luminescent Thin-Film CdSe/ZnSe Quantum Dot Composites Using CdSe Quantum Dots Passivated with an Overlayer of ZnSe. *Chemistry of Materials* **1996,** *8* (1), 173-180.

25. Kim, Y.-T.; Han, J. H.; Hong, B. H.; Kwon, Y.-U., Electrochemical Synthesis of CdSe Quantum-Dot Arrays on a Graphene Basal Plane Using Mesoporous Silica Thin-Film Templates. *Advanced Materials* **2010,** *22* (4), 515-518.

26. Murcia, M. J.; Shaw, D. L.; Woodruff, H.; Naumann, C. A.; Young, B. A.; Long, E. C., Facile Sonochemical Synthesis of Highly Luminescent ZnS−Shelled CdSe Quantum Dots. *Chemistry of Materials* **2006,** *18* (9), 2219-2225.

27. Wang, J.; Han, H., Hydrothermal synthesis of high-quality type-II CdTe/CdSe quantum dots with near-infrared fluorescence. *Journal of Colloid and Interface Science* **2010,** *351* (1), 83-87.

28. Hamizi, N. A.; Johan, M. R., Synthesis and size dependent optical studies in CdSe quantum dots via inverse micelle technique. *Materials Chemistry and Physics* **2010,** *124* (1), 395-398.

29. Micic, O. I.; Curtis, C. J.; Jones, K. M.; Sprague, J. R.; Nozik, A. J., Synthesis and Characterization of InP Quantum Dots. *The Journal of Physical Chemistry* **1994,** *98* (19), 4966-4969.

30. Mićić, O. I.; Ahrenkiel, S. P.; Nozik, A. J., Synthesis of extremely small InP quantum dots and electronic coupling in their disordered solid films. *Applied Physics Letters* **2001,** *78* (25), 4022-4024.

31. Tessier, M. D.; Dupont, D.; De Nolf, K.; De Roo, J.; Hens, Z., Economic and Size-Tunable Synthesis of InP/ZnE (E = S, Se) Colloidal Quantum Dots. *Chemistry of Materials* **2015,** *27* (13), 4893-4898.

32. Ramasamy, P.; Kim, N.; Kang, Y.-S.; Ramirez, O.; Lee, J.-S., Tunable, Bright, and Narrow-Band Luminescence from Colloidal Indium Phosphide Quantum Dots. *Chemistry of Materials* **2017,** *29* (16), 6893-6899.

33. Byun, H.-J.; Lee, J. C.; Yang, H., Solvothermal synthesis of InP quantum dots and their enhanced luminescent efficiency by post-synthetic treatments. *Journal of Colloid and Interface Science* **2011,** *355* (1), 35-41.

34. Reiss, P.; Carrière, M.; Lincheneau, C.; Vaure, L.; Tamang, S., Synthesis of Semiconductor Nanocrystals, Focusing on Nontoxic and Earth-Abundant Materials. *Chemical Reviews* **2016,** *116* (18), 10731-10819.

35. Zhong, H.; Zhou, Y.; Ye, M.; He, Y.; Ye, J.; He, C.; Yang, C.; Li, Y., Controlled Synthesis and Optical Properties of Colloidal Ternary Chalcogenide CuInS2 Nanocrystals. *Chemistry of Materials* **2008,** *20* (20), 6434-6443.

36. Zhong, H.; Bai, Z.; Zou, B., Tuning the Luminescence Properties of Colloidal I–III–VI Semiconductor Nanocrystals for Optoelectronics and Biotechnology Applications. *The Journal of Physical Chemistry Letters* **2012,** *3* (21), 3167-3175.

37. Kolny-Olesiak, J.; Weller, H., Synthesis and Application of Colloidal CuInS2 Semiconductor Nanocrystals. *ACS applied materials & interfaces* **2013,** *5* (23), 12221-12237.

38. Leach, A. D. P.; Macdonald, J. E., Optoelectronic Properties of CuInS2 Nanocrystals and Their Origin. *The Journal of Physical Chemistry Letters* **2016,** *7* (3), 572-583.

39. van der Stam, W.; Berends, A. C.; de Mello Donega, C., Prospects of Colloidal Copper Chalcogenide Nanocrystals. *Chemphyschem : a European journal of chemical physics and physical chemistry* **2016,** *17* (5), 559-581.

40. Berends, A. C.; Mangnus, M. J. J.; Xia, C.; Rabouw, F. T.; de Mello Donega, C., Optoelectronic Properties of Ternary I–III–VI2 Semiconductor Nanocrystals: Bright Prospects with Elusive Origins. *The Journal of Physical Chemistry Letters* **2019,** *10* (7), 1600-1616.

41. Zang, H.; Li, H.; Makarov, N. S.; Velizhanin, K. A.; Wu, K.; Park, Y. S.; Klimov, V. I., Thick-Shell CuInS2/ZnS Quantum Dots with Suppressed "Blinking" and Narrow Single-Particle Emission Line Widths. *Nano Lett* **2017,** *17* (3), 1787-1795.

42. Knowles, K. E.; Nelson, H. D.; Kilburn, T. B.; Gamelin, D. R., Singlet–Triplet Splittings in the Luminescent Excited States of Colloidal Cu+:CdSe, Cu+:InP, and CuInS2 Nanocrystals: Charge-Transfer Configurations and Self-Trapped Excitons. *Journal of the American Chemical Society* **2015,** *137* (40), 13138-13147.

43. Rice, W. D.; McDaniel, H.; Klimov, V. I.; Crooker, S. A., Magneto-Optical Properties of CuInS2 Nanocrystals. *The Journal of Physical Chemistry Letters* **2014,** *5* (23), 4105-4109.

44. Fuhr, A. S.; Yun, H. J.; Makarov, N. S.; Li, H.; McDaniel, H.; Klimov, V. I., Light Emission Mechanisms in CuInS2 Quantum Dots Evaluated by Spectral Electrochemistry. *ACS Photonics* **2017,** *4* (10), 2425-2435.

45. Pinchetti, V.; Lorenzon, M.; McDaniel, H.; Lorenzi, R.; Meinardi, F.; Klimov, V. I.; Brovelli, S., Spectro-electrochemical Probing of Intrinsic and Extrinsic Processes in Exciton Recombination in I–III–VI2 Nanocrystals. *Nano letters* **2017,** *17* (7), 4508-4517.

46. Medda, R.; Jakobs, S.; Hell, S. W.; Bewersdorf, J., 4Pi microscopy of quantum dot-labeled cellular structures. *Journal of Structural Biology* **2006,** *156* (3), 517-523.

47. Herbert, S.; Soares, H.; Zimmer, C.; Henriques, R., Single-Molecule Localization Super-Resolution Microscopy: Deeper and Faster. *Microscopy and Microanalysis* **2012,** *18* (6), 1419-1429.

48. Freundlich, M. M., Origin of the electron microscope. *Science* **1963,** *142* (3589), 185-188.

49. Jonge, N. d.; Peckys, D. B.; Kremers, G. J.; Piston, D. W., Electron microscopy of whole cells in liquid with nanometer resolution. *Proceedings of the National Academy of Sciences* **2009,** *106* (7), 2159.

50. Pohl, D. W.; Denk, W.; Lanz, M., Optical stethoscopy: Image recording with resolution λ/20. *Applied Physics Letters* **1984,** *44* (7), 651-653.

51. Betzig, E.; Trautman, J. K.; Harris, T. D.; Weiner, J. S.; Kostelak, R. L., Breaking the Diffraction Barrier: Optical Microscopy on a Nanometric Scale. *Science* **1991,** *251* (5000), 1468.

52. Hell, S.; Stelzer, E. H. K., Fundamental improvement of resolution with a 4Pi-confocal fluorescence microscope using two-photon excitation. *Optics Communications* **1992,** *93* (5), 277-282.

53. Gustafsson; Agard; Sedat, I5M: 3D widefield light microscopy with better than 100 nm axial resolution. *Journal of Microscopy* **1999,** *195* (1), 10-16.

54. Hell, S. W.; Wichmann, J., BREAKING THE DIFFRACTION RESOLUTION LIMIT BY STIMULATED-EMISSION - STIMULATED-EMISSION-DEPLETION FLUORESCENCE MICROSCOPY. *Optics Letters* **1994,** *19* (11), 780-782.

55. Huang, B.; Bates, M.; Zhuang, X., Super-Resolution Fluorescence Microscopy. *Annual Review of Biochemistry* **2009,** *78* (1), 993-1016.

56. Willig, K. I.; Kellner, R. R.; Medda, R.; Hein, B.; Jakobs, S.; Hell, S. W., Nanoscale resolution in GFP-based microscopy. *Nature Methods* **2006,** *3* (9), 721-723.

57. Gustafsson, M. G. L., Surpassing the lateral resolution limit by a factor of two using structured illumination microscopy. *Journal of Microscopy* **2000,** *198*, 82-87.

58. Gustafsson, M. G. L., Nonlinear structured-illumination microscopy: Wide-field fluorescence imaging with theoretically unlimited resolution. *Proceedings of the National Academy of Sciences of the United States of America* **2005,** *102* (37), 13081.

59. Schermelleh, L.; Carlton, P. M.; Haase, S.; Shao, L.; Winoto, L.; Kner, P.; Burke, B.; Cardoso, M. C.; Agard, D. A.; Gustafsson, M. G. L.; Leonhardt, H.; Sedat, J. W., Subdiffraction multicolor imaging of the nuclear periphery with 3D structured illumination microscopy. *Science* **2008,** *320* (5881), 1332-1336.

60. Shao, L.; Kner, P.; Rego, E. H.; Gustafsson, M. G. L., Super-resolution 3D microscopy of live whole cells using structured illumination. *Nature Methods* **2011,** *8* (12), 1044-+.

61. Betzig, E.; Patterson, G. H.; Sougrat, R.; Lindwasser, O. W.; Olenych, S.; Bonifacino, J. S.; Davidson, M. W.; Lippincott-Schwartz, J.; Hess, H. F., Imaging intracellular fluorescent proteins at nanometer resolution. *Science* **2006,** *313* (5793), 1642-1645.

62. Rust, M. J.; Bates, M.; Zhuang, X., Sub-diffraction-limit imaging by stochastic optical reconstruction microscopy (STORM). *Nature Methods* **2006,** *3* (10), 793-795.

63. Gutierrez, R.; Grossmann, G.; Frommer, W. B.; Ehrhardt, D. W., Opportunities to Explore Plant Membrane Organization with Super-Resolution Microscopy. *Plant Physiology* **2010,** *154* (2), 463.

64. Thompson, R. E.; Larson, D. R.; Webb, W. W., Precise nanometer localization analysis for individual fluorescent probes. *Biophysical Journal* **2002,** *82* (5), 2775-2783.

65. Yildiz, A.; Forkey, J. N.; McKinney, S. A.; Ha, T.; Goldman, Y. E.; Selvin, P. R., Myosin V Walks Hand-Over-Hand: Single Fluorophore Imaging with 1.5-nm Localization. *Science* **2003,** *300* (5628), 2061.

66. Moerner, W. E., Single-Molecule Spectroscopy, Imaging, and Photocontrol: Foundations for Super-Resolution Microscopy (Nobel Lecture). *Angewandte Chemie International Edition* **2015,** *54* (28), 8067-8093.

67. Patterson, G. H.; Lippincott-Schwartz, J., A Photoactivatable GFP for Selective Photolabeling of Proteins and Cells. *Science* **2002,** *297* (5588), 1873.

68. Shroff, H.; Galbraith, C. G.; Galbraith, J. A.; Betzig, E., Live-cell photoactivated localization microscopy of nanoscale adhesion dynamics. *Nature Methods* **2008,** *5* (5), 417-423.

69. Diaspro, A. E., van Zandvoort, M. (Ed.) *Super-Resolution Imaging in Biomedicine*. Boca Raton: CRC Press: 2017.

70. Fernández-Suárez, M.; Ting, A. Y., Fluorescent probes for super-resolution imaging in living cells. *Nature Reviews Molecular Cell Biology* **2008,** *9* (12), 929-943.

71. Heilemann, M.; van de Linde, S.; Mukherjee, A.; Sauer, M., Super-Resolution Imaging with Small Organic Fluorophores. *Angewandte Chemie International Edition* **2009,** *48* (37), 6903-6908.

72. Patterson, G.; Davidson, M.; Manley, S.; Lippincott-Schwartz, J., Superresolution Imaging using Single-Molecule Localization. *Annual Review of Physical Chemistry* **2010,** *61* (1), 345-367.

73. Endesfelder, U.; Malkusch, S.; Flottmann, B.; Mondry, J.; Liguzinski, P.; Verveer, P. J.; Heilemann, M., Chemically Induced Photoswitching of Fluorescent Probes—A General Concept for Super-Resolution Microscopy. *Molecules* **2011,** *16* (4).

74. Jin, D.; Xi, P.; Wang, B.; Zhang, L.; Enderlein, J.; van Oijen, A. M., Nanoparticles for super-resolution microscopy and single-molecule tracking. *Nature Methods* **2018,** *15* (6), 415-423.

75. Resch-Genger, U.; Grabolle, M.; Cavaliere-Jaricot, S.; Nitschke, R.; Nann, T., Quantum dots versus organic dyes as fluorescent labels. *Nature Methods* **2008,** *5* (9), 763-775.

76. Subach, F. V.; Patterson, G. H.; Manley, S.; Gillette, J. M.; Lippincott-Schwartz, J.; Verkhusha, V. V., Photoactivatable mCherry for high-resolution two-color fluorescence microscopy. *Nature Methods* **2009,** *6* (2), 153-159.

77. Wu, X.; Liu, H.; Liu, J.; Haley, K. N.; Treadway, J. A.; Larson, J. P.; Ge, N.; Peale, F.; Bruchez, M. P., Immunofluorescent labeling of cancer marker Her2 and other cellular targets with semiconductor quantum dots. *Nature Biotechnology* **2003,** *21* (1), 41-46.

78. Lidke, K. A.; Rieger, B.; Jovin, T. M.; Heintzmann, R., Superresolution by localization of quantum dots using blinking statistics. *Optics Express* **2005,** *13* (18), 7052-7062.

79. Irvine, S. E.; Staudt, T.; Rittweger, E.; Engelhardt, J.; Hell, S. W., Direct light-driven modulation of luminescence from Mn-doped ZnSe quantum dots. *Angewandte Chemie-International Edition* **2008,** *47* (14), 2685-2688.

80. Watanabe, T. M.; Fukui, S.; Jin, T.; Fujii, F.; Yanagida, T., Real-Time Nanoscopy by Using Blinking Enhanced Quantum Dots. *Biophysical Journal* **2010,** *99* (7), L50-L52.

81. Hanne, J.; Falk, H. J.; Görlitz, F.; Hoyer, P.; Engelhardt, J.; Sahl, S. J.; Hell, S. W., STED nanoscopy with fluorescent quantum dots. *Nature communications* **2015,** *6*, 7127-7127.

82. Dertinger, T.; Colyer, R.; Iyer, G.; Weiss, S.; Enderlein, J., Fast, background-free, 3D super-resolution optical fluctuation imaging (SOFI). *Proceedings of the National Academy of Sciences of the United States of America* **2009,** *106* (52), 22287-22292.

83. Wang, Y.; Fruhwirth, G.; Cai, E.; Ng, T.; Selvin, P. R., 3D Super-Resolution Imaging with Blinking Quantum Dots. *Nano Letters* **2013,** *13* (11), 5233-5241.

84. Xu, J.; Tehrani, K. F.; Kner, P., Multicolor 3D Super-resolution Imaging by Quantum Dot Stochastic Optical Reconstruction Microscopy. *ACS Nano* **2015,** *9* (3), 2917-2925.

85. Zhou, B.; Shi, B.; Jin, D.; Liu, X., Controlling upconversion nanocrystals for emerging applications. *Nature Nanotechnology* **2015,** *10* (11), 924-936.

86. Fan, W.; Bu, W.; Shi, J., Upconversion Nanoparticles: On The Latest Three-Stage Development of Nanomedicines based on Upconversion Nanoparticles (Adv. Mater. 21/2016). *Advanced Materials* **2016,** *28* (21), 3977-3977.

87. He, H.; Liu, X.; Li, S.; Wang, X.; Wang, Q.; Li, J.; Wang, J.; Ren, H.; Ge, B.; Wang, S.; Zhang, X.; Huang, F., High-Density Super-Resolution Localization Imaging with Blinking Carbon Dots. *Analytical Chemistry* **2017,** *89* (21), 11831-11838.

88. Zhi, B.; Cui, Y.; Wang, S.; Frank, B. P.; Williams, D. N.; Brown, R. P.; Melby, E. S.; Hamers, R. J.; Rosenzweig, Z.; Fairbrother, D. H.; Orr, G.; Haynes, C. L., Malic Acid Carbon Dots: From Super-resolution Live-Cell Imaging to Highly Efficient Separation. *ACS Nano* **2018,** *12* (6), 5741-5752.

89. Wu, C.; Schneider, T.; Zeigler, M.; Yu, J.; Schiro, P. G.; Burnham, D. R.; McNeill, J. D.; Chiu, D. T., Bioconjugation of Ultrabright Semiconducting Polymer Dots for Specific Cellular Targeting. *Journal of the American Chemical Society* **2010,** *132* (43), 15410-15417.

90. Chen, X.; Li, R.; Liu, Z.; Sun, K.; Sun, Z.; Chen, D.; Xu, G.; Xi, P.; Wu, C.; Sun, Y., Small Photoblinking Semiconductor Polymer Dots for Fluorescence Nanoscopy. *Advanced Materials* **2017,** *29* (5), 1604850.

91. Fish, K. N., Total Internal Reflection Fluorescence (TIRF) Microscopy. *Current Protocols in Cytometry* **2009,** *50* (1), 12.18.1-12.18.13.

92. Kim, H.; Selvin, P. R., Fluorescence Imaging with One Nanometer Accuracy. In *Encyclopedia of Biophysics*, Roberts, G. C. K., Ed. Springer Berlin Heidelberg: Berlin, Heidelberg, 2013; pp 803-809.

Chapter 2. $CuInS_2$-doped ZnS Quantum Dots Obtained via Non-Injection Cation Exchange Show Reduced but Heterogeneous Blinking and Provides Insights into their Structure-Optical Property Relationships

Anh T. Nguyen, Feng Gao, Dustin Baucom and Colin D. Heyes*

Department of Chemistry and Biochemistry, University of Arkansas, 345 North Campus Drive, Fayetteville, Arkansas 72701, United States

Corresponding author: Colin D. Heyes; email: cheyes@uark.edu

2.1. Abstract

Cadmium-free $CuInS_2$-doped ZnS quantum dots (QDs) are synthesized through a 2-step non-injection synthetic method. The resulting QDs are small (8 nm or less) and relatively isotropic with photoluminescence quantum yields (PL QY) up to almost 70% and emission peaks in the 560-600 nm window, depending on the amount of Zn precursor added. The results indicate small $CuInS_2$ 'clusters' within a zinc-blende ZnS lattice are the radiative recombination centers in the nanoparticle. Interestingly, higher ensemble photoluminescence quantum yields (PL QY) result when cation exchange is less extensive (~80 % ZnS composition), while a reduction in blinking is observed when ZnS composition exceeds 99%. A wide heterogeneity in blinking behavior from QD-to-QD is evident and a subpopulation statistical analysis shows that the on-state dwell times change from multiexponential (or inverse power law) behavior towards more mono-exponential behavior for particles that spend more of their time in the on-state. These results indicate that, as the number of $CuInS_2$ emitting centers is reduced, the number of pathways leading to the off-state decreases, and a model is proposed to relate this behavior to the QD structure. These results provide a novel route towards $CuInS_2$-doped visible-light emitting ZnS QDs with high quantum yield and reduced blinking and provides insight into how the composition of dopant and host matrix affects the radiative recombination mechanisms in single particles.

2.2. Introduction

Colloidal semiconductor nanocrystals (NCs), also known as quantum dots (QDs), have shown great potential in applications such as bioimaging,[1-2] lasers,[3] light emitting diodes[4] and solar-harvesting materials[5] since their optical properties can be tuned by size and shape due to quantum-confinement effects. The vast majority of colloidal QD studies have been performed on the II-VI

CdE (E=S, Se, Te) (for reviews see refs 6[6], 7[7] and 8[8] and references therein) although other binary materials such as IV-VI PbE[9] and III-V InP[10] and InAs[11-12] have also been investigated.

A particularly interesting phenomena that colloidal QDs exhibit is that of fluorescence intermittency (or blinking) of QDs at the single-particle level. Although academically interesting, it can severely limit certain biological and optoelectronic applications of QDs, such as for single nanoparticle tracking[13-14] and single-photon light sources.[15] Since blinking of Cd-containing QDs was first reported in 1996,[16] the underling mechanisms of blinking have been extensively studied, (see ref 8[8] and references therein) particularly towards the aim of reducing or eliminating it. Blinking reduction/elimination is primarily accomplished by epitaxial shelling of the emitting QD core, although it is critical to take the utmost care in the choice of shelling material(s), thickness and reaction conditions.[17-21] Two types of blinking have been identified – the originally-hypothesized charging (on → off)/neutralization (off → on) processes that is dependent on the excitation power[22-23] and external environment[24-28] and internal/surface trapping of charge carriers that is dependent on the QD composition and architecture.[21, 29-32]

$CuInS_2$ (CIS) QDs are ternary I-III-VI systems that have recently attracted a great deal of interest as a less toxic alternative to binary II-VI CdE QDs .[33-36] In addition to the lower toxicity, the large photoluminescence (PL) Stokes shifts and long fluorescence lifetimes of CIS NCs also make them particularly attractive emitters for applications in bioimaging,[37-40] light-emitting diodes,[41] and luminescent solar concentrators.[42] Compared to II−VI or IV−VI semiconductor NCs such as CdE and PbE, however, single-particle studies of CIS QDs are still very limited, especially as it relates to understanding blinking mechanisms in these ternary systems. Upon adding ZnS shelling precursors to the CIS cores, a blue-shift in the emission spectrum is observed, suggesting that a

certain amount of ion exchange occurs in addition to shelling that reduces the size of the emitting core to produce a partially-alloyed Cu(Zn)InS_2/ZnS (C(Z)IS/ZnS) core/shell system.[33-34] This complicates the ternary I-III-VI QD system even more by forming a (partial) quaternary I-(II)-III-VI core and a binary II-VI shell. The Ren group reported a three-step synthesis approach consisting of CIS core synthesis, alloying of cores with Zn to produce C(Z)IS, followed by ZnS shelling to reduce blinking, the results of which were highly dependent on the Cu:In:Zn ratio used and the reaction time.[43] When thick shells of ZnS were added to CIS cores using a two-step shelling approach, suppressed blinking was also reported with QD sizes averaging 12.5 nm and being tetrahedral in shape.[44] This strategy led to a distribution in the blinking behavior with on-times fraction ranging from 0.2 to 1.0.

These multi-step shelling approaches[43-44] utilized a syringe-pump for dropwise hot-injection of $Zn(St)_2$ precursor solution into CIS cores, which is not ideal for large scale production.[45-46] Furthermore, the relationship between QD structure/composition and how they evolve from being blinking to non-blinking is still not completely clear. In this study, we avoid the hot injection approach to synthesize C(Z)IS/ZnS QDs with photoluminescence quantum yields up to 67%, which is comparable to the hot-injection approach. The optical properties at the ensemble and single particle level of C(Z)IS/ZnS are characterized as a functions of the amount of Zn precursor (zinc stearate, $Zn(St)_2$) added. The QD size, shape, crystal structure and elemental composition are also investigated to develop a better understanding of structure-optical property relationships of the QDs. As the amount of $Zn(St)_2$ used is increased, cation exchange is observed and the QDs transition from CIS through a core/shell like structure to almost pure ZnS with <1% of Cu and In remaining. Thus, emitting $CuInS_2$ clusters effectively act as a dopant in a ZnS lattice. Concurrent with this transition, blinking is reduced, although heterogeneity in blinking from QD-to-QD

increased. We perform a sub-population analysis to explore the origins of this heterogeneity and to gain a deeper insight into the relationship between blinking mechanism and QD structure. We show that as QD blinking is reduced, the on-times blinking statistics shift from multi-exponential (or inverse power-law) behavior towards mono-exponential behavior, while the off-times blinking statistics show the opposite trend, albeit to a lesser extent. We anticipate that these results will help provide a framework to design large scale production of reduced blinking, Cd-free QDs.

2.3. Methods

2.3.1. Synthesis and Cation Exchange

Materials. Copper (I) iodide (CuI, 99.999%, Sigma Aldrich), indium acetate (In(Ac)3, 99.99%, Alfa Aesar), sulfur powder (S, 100 mesh, 99.5%, Alfa Aesar), 1-dodecanethiol (DDT, 98%, Sigma Aldrich), 1-octadecene (ODE, 90%, Acros), zinc stearate ($Zn(St)_2$, Acros). All solvents were purchased from VWR International. Methanol and hexane were of pure grade.

Synthesis of CIS QDs. CIS QDs are synthesized by modification of the literature methods.[47]

Briefly, 0.292g of $In(Ac)_3$, 0.048g of CuI, 1mL of DDT and 10mL of ODE were mixed in a 50mL three-neck round bottom flask (rbf). This solution was first degassed under vacuum for at least 30 minutes at room temperature, then purged with argon for 30 minutes. Subsequently under argon flux the solution was heated to 210 ^{o}C for 40 minutes under argon flow. The color of the solution changed from yellow to orange to deep red as the QDs grew in size. The solution was cooled and then centrifuged at 4000 rpm for 10 minutes. The precipitation was disposed of and the solution was kept for cation exchange step.

Cation exchange with Zn. Different molar amounts (0.1 mmol, 1 mmol, 2 mmol, 4 mmol) of $Zn(St)_2$ were added to the cores. For a typical cation exchange reaction using 0.1 mmol of $Zn(St)_2$, 0.0632g of $Zn(St)_2$ was added to a 100mL RBF. Then, 20mL of ODE, 5mL of DDT and 100uL of

CIS QDs were added to the RBF. The mixture was stirred under vacuum at 60 °C for 30 minutes and backfilled with argon for 30 minutes. Under argon flux, the reaction temperature was increased to 230 °C. Samples were taken at 6h, 12h, 24h, 48h. Samples will be washed three times with a 50/50 mixture of hexane and methanol.

Apart from the ensemble optical characterization, for which the whole time series were measured, QDs following 48h of cation exchange were selected for further characterization.

2.3.2. Morphological and structural characterization of QDs. For structural and size characterization, X-ray powder diffraction (XRD) pattern was taken on a X-ray diffractometer (Rigaku, Japan) equipped with Cu Kα radiation (λ = 1.5418 Å, 40 kV, 30 mA). Bright field TEM images were taken on a Jeol with an accelerating voltage of 100 kV. The average QD size and size distribution were estimated by analyzing TEM images of 100 QDs. HRTEM images for analyzing d spacing of QDs were recorded on a Titan with an accelerating voltage of 300 kV.

2.3.3. Chemical Composition. The elemental compositions of QDs were analyzed by an iCAP-6300 inductively coupled plasma mass spectrometer (Thermo Scientific, iCAP Q). Samples were dissolved in concentrated HCl/HNO_3 3:1 (v/v) to completely dissolve the QDs into their component ions.

2.3.4. Optical measurement of QDs at the ensemble level. Absorption spectra of CIS before and after cation exchange were obtained by a Hitachi U-3900H UV/Vis-spectrophotometer and fluorescence emission spectra were recorded with a Perkin Elmer LS55 Luminescence Spectrometer. The relative PL quantum yields (QYs) of various QD samples were comparatively studied by comparison with that of Rhodamine 6G (95% in ethanol) as follows:

$$QY_{QD}=QY_{R6G}\times(OD_{R6G}/OD_{QD}) \times(n_{QD}/n_{R6G})^2$$

The excitation wavelength was set at 485 nm and the optical density (OD) was used ~ 0.05.

Fluorescence lifetimes measurements were taken using a MicroTime 200 fluorescence microscope (PicoQuant GmbH, Berlin, Germany), which is based on an Olympus IX71 microscope equipped with a PicoHarp 300 TCSPC controller. It uses a 485 nm laser (PDL 485, Picoquant) operating at 10 μW power to excite the QDs, using a dichroic mirror (500dcxr, Chroma) to send the laser through a water immersion objective (Olympus, Apochromat 60×, NA 1.3) to achieve a diffraction-limited laser focus. The fluorescence is collected by the same objective and passed through the same dichroic mirror and a 100 μm diameter pinhole. A fluorescence filter (620/60, Chroma) for CIS cores measurements and (605/55, Chroma) for CIS/ZnS QDs measurements is placed in front of a single photon avalanche diode detector (MPD SPAD, Microphotonic Devices, Bolano, Italy) to reject background fluorescence and scattered laser light. The objective is positioned on a subnanometer precision 3D piezo scanning stage (PI, Berlin, Germany). SymPhoTime software is used to control all acquisition and exporting functions. For ensemble fluorescence lifetime measurements, the pulsed laser was operated with a repetition rate of 80 MHz and focused into a ~10 nM solution of QDs.

The average lifetime (τ_{av}) is defined as: $\tau_{av} = \frac{\sum_i a_i \tau_i^2}{\sum_i a_i \tau_i}$

2.3.5. Optical measurement of QDs at single-particle level. Samples were prepared for single particle experiments by spin casting freshly diluted QDs in hexane. The QD particle density was controlled by changing the concentration of the QDs in the solution before spin coating.

Fluorescence of single QDs were acquired by an epi-fluorescent imaging system based on an Olympus IX 71 inverted fluorescence microscope (Olympus Optical Co., Japan).

The QDs samples were excited with a 488 nm laser (Dream Lasers Technology Co. Ltd., Shanghai, China) and the laser power monitored in front of an oil-immersion microscope objective (NA1.45/100×, Olympus Optical Co., Japan) was measured to be 1.55 mW after it was attenuated.

The laser was focused onto the back plane of the objective to provide an illumination area of ~200 × 200 μm^2 on the cover slip. Fluorescence from the sample was collected by the same objective, separated from the excitation light by a dichroic mirror and emission filters (613/205, Semrock), and then directed into an electron-multiplying charge coupled device (EM-CCD, ANDOR iXON Ultra 888) camera. The imaging array was 1024 × 1024 pixels with 13 × 13 μm^2/pixel. The frame rate was set at 20 fps (50 ms/frame) for all samples utilizing a frame transfer approach in which the next frame is acquired while the previous frame is read out, allowing for continuous movies to be acquired. Single particle trace extraction from the movie acquisition was processed using a Python home-built program that identifies the pixels originating from the QD emission and subtracts the local background signal from it. Only QDs in the central ~200 × 200 pixels portion of the CCD chip were used to minimize effects of illumination power variations due to the 2-D Gaussian laser illumination profile. At least 100 dots are randomly selected and analyzed for each sample. Single-particle blinking analysis to extract on and off time probability densities used homemade analysis software written in Igor, as previously described.[21, 31-32] All measurements were performed at room temperature.

2.4. Results

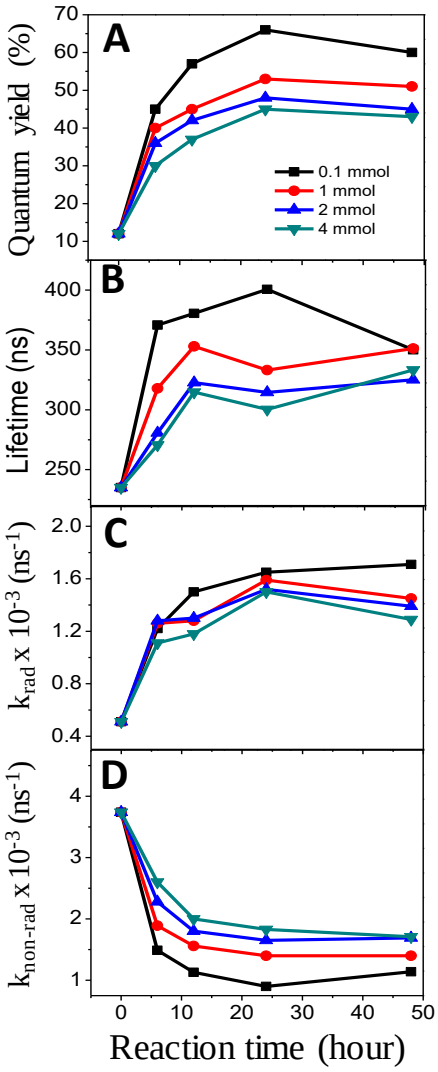

Figure 2.1. Ensemble fluorescence properties of CIS upon reaction with different $Zn(St)_2$ concentrations (0.1; 1; 2; 4 mmol). (A) Quantum yield; (B) Lifetime; (C) k_{rad}; (D) $k_{non-rad}$.

The ensemble fluorescence properties of CIS QDs as a function of time after adding $Zn(St)_2$ and heating to 230 °C is presented in figure 2.1. The photoluminescence quantum yield (PL QY) of CIS, synthesized with a In:Cu molar ratio of 4:1 is 12%, which is comparable to other reports that found

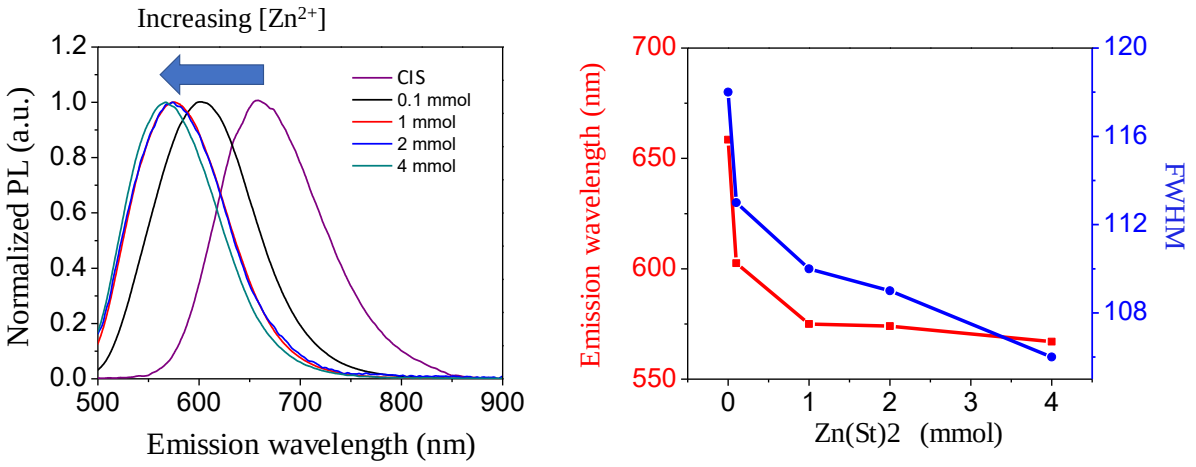

Figure 2.2. Left: Emission spectra, Right: Emission wavelength and peak full width at half maximum (FWHM) of CIS before and after cation exchange as a function of the amount of $Zn(St)_2$ used.

this ratio provided the highest PL QY.[47-48] The PL QY significantly increases to between 40-67% upon adding various concentrations of $Zn(St)_2$ to the prepared CIS. The PL QY as functions of time with different amounts of $Zn(St)_2$ share a similar pattern: first they sharply increase within 6h, continue to gradually increase reaching the highest values after 24h and then slightly decrease up to 48h. Interestingly higher PL QY results when *less* Zn is used rather than more. The average fluorescence lifetime follows approximately the same trend, resulting from a steady increase of the average radiative rate, k_{rad}, and a steady decrease in the average non-radiative rate, $k_{non\text{-}rad}$. The results show that k_{rad} increases more and $k_{non\text{-}rad}$ decreases more when less $Zn(St)_2$ is used than when more is used, with the effect on $k_{non\text{-}rad}$ being more pronounced than on k_{rad}.

The emission spectrum of CIS after a complete 48h of reaction at 230 ^{o}C with different amounts of $Zn(St)_2$ is shown in Figure 2.2. As the amount of $Zn(St)_2$ is increased, the emission spectrum of CIS/ZnS QDs is blue-shifted compared to the initial CIS, which is indicative of cation exchange of Zn^{2+} with Cu^{+} and/or In^{3+} as previously discussed.[49-52]

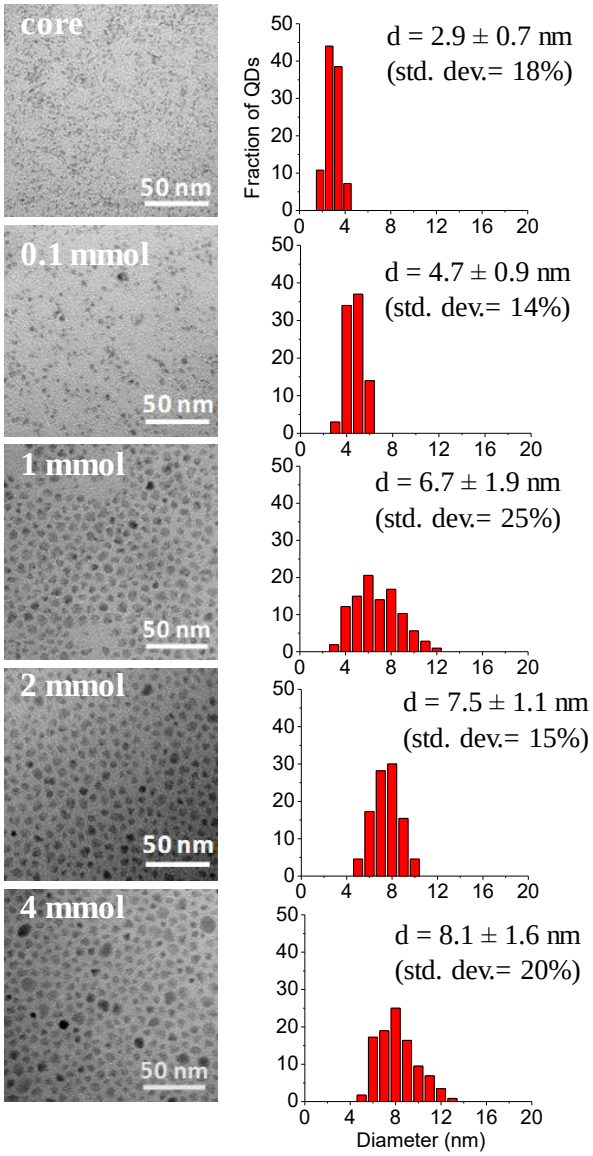

Figure 2.3. TEM images of CIS cores and CIS/ZnS QDs (left) and their corresponding size histogram (right).

The degree of blue shift from the emission spectrum is most noticeable up to 1 mmol of $Zn(St)_2$, and becomes relatively steady between 2 mmol and 4 mmol of $Zn(St)_2$, suggesting that the increased quantum confinement effects on the CIS emitting centers do not become stronger when more than 1 mmol $Zn(St)_2$ is used. The FWHM also decreases upon cation exchange with Zn, although this continues to decrease even when the blue shift levels off.

Figure 2.3 shows representative TEM images (left panel) and size histograms (right panel) of CIS before and after 48h of reaction with $Zn(St)_2$. The initial CIS have an average size of 2.9 nm. Upon reaction with Zn, the shape of CIS/ZnS QDs remain moderately isotropic compared to the strongly anisotropic shapes, such as pyramidal, that has been reported previously upon shelling.[43-44] Their average size increases as more $Zn(St)_2$ is used: 4.7 nm using 0.1 mmol $Zn(St)_2$, 6.7 nm using 1 mmol, 7.5 nm using 2mmol and 8.1 nm using 4 mmol. This trend is similar to the observed blue-shift, suggesting that both cation-exchange and additional ZnS growth occurs. The standard deviation in measured sizes fluctuates between 14-25%, although it does not vary consistently with the amount of $Zn(St)_2$ used.

In order to determine the effect of cation exchange on the crystal structure, Figure 2.4 presents the XRD diffraction patterns (left) of CIS before and after 48h of reaction with 0.1 and 4 mmol of $Zn(St)_2$, as well as their corresponding representative HRTEM images (right). The characteristic XRD peaks of CIS match up with their chalcopyrite structure (red peaks). Upon reaction of CIS with Zn the XRD peaks shift toward the ZnS zinc blende structure. The HRTEM images show that the CIS and CIS/ZnS QDs are highly crystalline. The d spacing values of the chalcopyrite of CIS and zinc blende of ZnS are very close,[53-54] so HRTEM cannot be used to differentiate chalcopyrite from zinc blende. However, the combined results of XRD and HRTEM suggest that the initial CIS are crystalline with chalcopyrite structure, but as 4 mmol $Zn(St)_2$ is used, cation exchange results in a lattice consistent with a zinc blende structure.

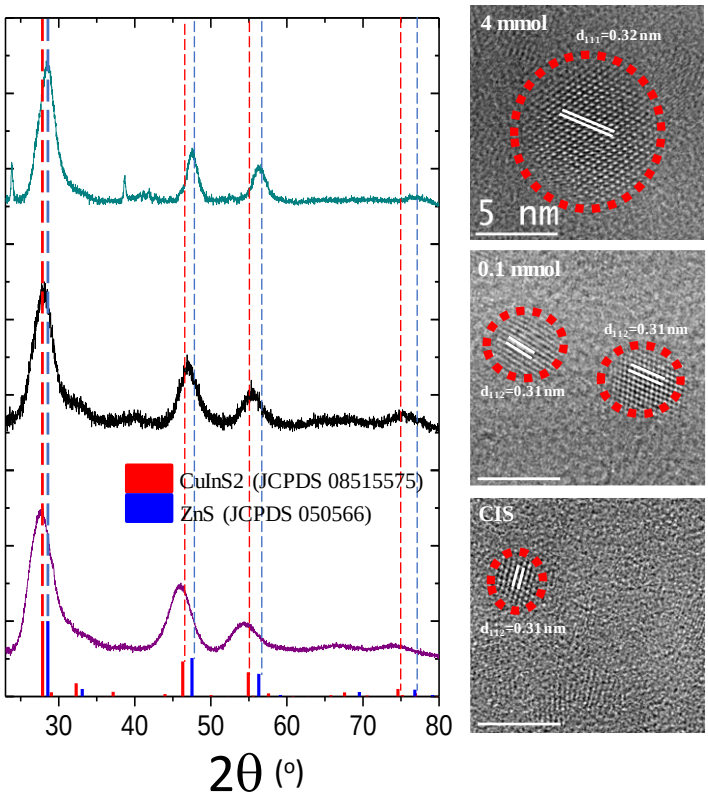

Figure 2.4. Left - X-ray diffraction (XRD) of CIS cores (purple) and CIS/ZnS QDs using 0.1 mmol $Zn(St)_2$ (black) and 4 mmol $Zn(St)_2$ (teal). Right -corresponding HR-TEM images.

The particles prepared with the lowest amount of Zn (0.1 mmol) show wider XRD peaks with their centers located between chalcopyrite and zinc blende, suggesting either the presence of both types of lattice or a strained lattice. The closeness of the two XRD patterns makes it difficult to differentiate these possibilities. Nevertheless, as 4 mmol Zn is used, the XRD pattern is indicative of almost pure zinc blende ZnS.

Elemental analysis was then performed to determine the degree of cation exchange in these particles, measured using inductively coupled plasma mass spectrometry (ICP-MS). Figure 2.5 and Table 2.1 shows the actual composition of the initial CIS is 80% In and 20% Cu (quantitatively 3.9:1 In:Cu as table 2.1 shows), in line with the 4:1 In:Cu molar ratio used in the synthesis. It is clear that, even when only 0.1 mmol $Zn(St)_2$ is used, there is a significant amount of Zn in the particles. In figure 2.5, the % composition of each element is plotted (in both linear and logarithmic

scales), and shows that 87% of the cations present are Zn when 0.1 mmol $Zn(St)_2$ was used. This increases to 98% Zn when 1mmol $Zn(St)_2$ was used and over 99% Zn when 4 mmol $Zn(St)_2$ is used. Clearly, the cation exchange is extensive to the point where the CIS components are at the level of dopant, rather than as a core/shell structure, as in the previously reported CIS/ZnS studies.[33-34, 44, 55] The data from figure 2.5 is shown in table 2.1, converted into molar ratios to enable a comparative quantities analysis of the In:Cu:Zn ratios as a function of the amount of $Zn(St)_2$ added.

Table 2.1. Chemical compositions of CIS cores and CIS/ZnS QDs using different $Zn(St)_2$ concentrations

$Zn(St)_2$ added (mmol)	**In:Cu:Zn**	**(In+Cu):Zn**
0	3.9:1:0	1:0
0.1	8.1:1:62	1:6.8
1	6.4:1:452	1:62
2	6.9:1:874	1:110
4	7.1:1:1101	1:136

.

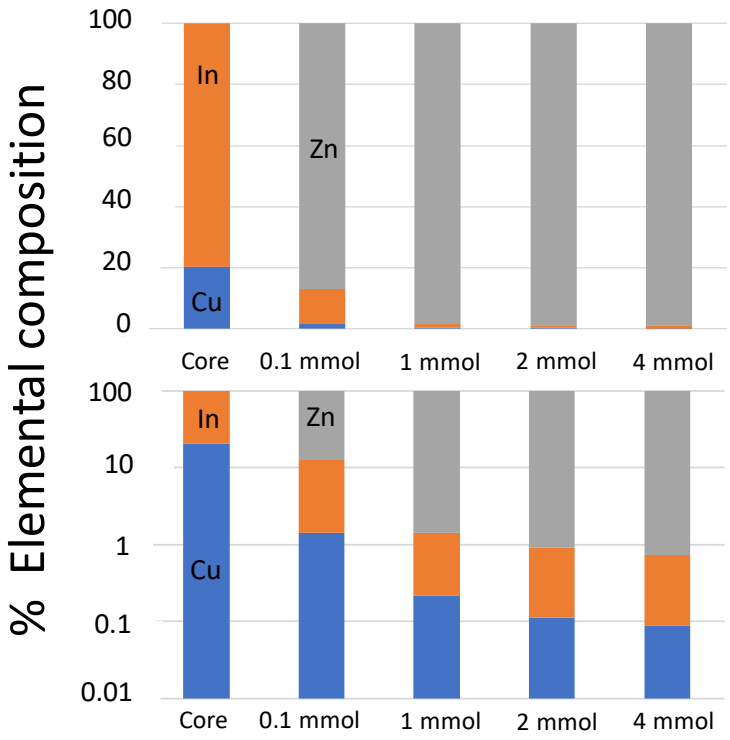

Figure 2.5. Percentage of elemental composition of CIS cores and CIS/ZnS QDs as function of $Zn(St)_2$ concentration. Linear scale (top) and log scale (bottom)

After 48h of reaction with $Zn(St)_2$, the molar ratios of In:Cu:Zn is 8.1:1:62, 6.4:1:452, 6.9:1:874 and 7.1:1:1101 at 0.1 mmol, 1 mmol, 2 mmol and 4 mmol of $Zn(St)_2$, respectively. In addition to the change in the relative Zn content of the QDs, the change in In:Cu molar ratio was determined to change from 3.9:1 in CIS core to 8.1:1 upon adding 0.1 mmol $Zn(St)_2$, showing that there is an enrichment of In relative to Cu following addition of Zn due to preferential cation exchange of Zn for Cu. In order to maintain charge neutrality of the crystal, the ratio of Cu^+:Cu^{2+} must also change to balance the relative enrichment of the In^{3+} ions. Cu^+ and Cu^{2+} ions have been proposed to have significant effects on photoluminescence.[56-57] This In:Cu enrichment reduces as more Zn is used, suggesting that the cation exchange has both kinetically and thermodynamically controlled aspects. When between 2 and 4 mmol $Zn(St)_2$ is used, the In:Cu ratio remains relatively constant,

although the particles still increase in size, suggesting that the extra Zn is added to the surface of the particles without affecting the very minor amounts of CIS that remain.

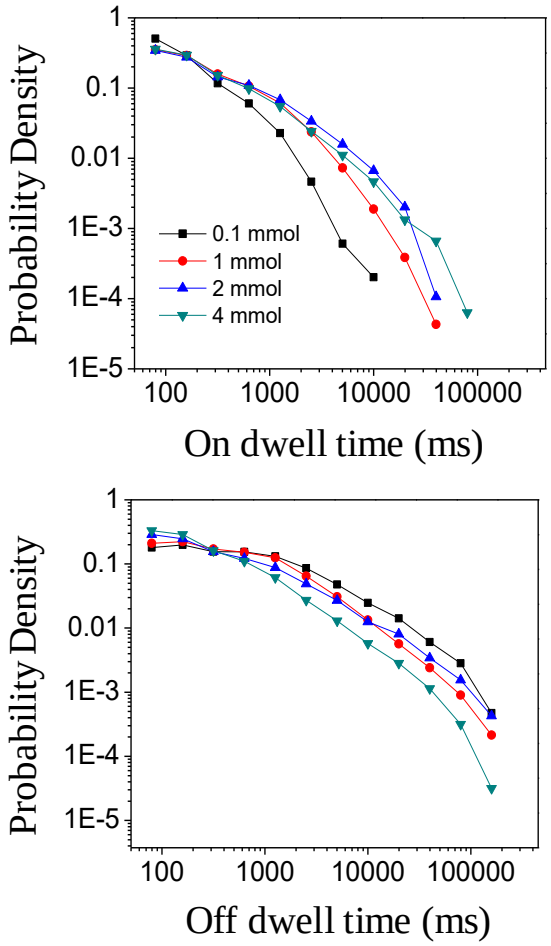

Figure 2.6. Probability density of on dwell time (top) and off dwell time (bottom) of over 100 CIS QDs after cation exchange using different amounts of $Zn(St)_2$.

Figure 2.6 shows the probability density of the on dwell time and off dwell time for over 100 CIS QDs after cation exchange as a function of the amount of $Zn(St)_2$ used. The single particle properties of the initial CIS QDs is not analyzed because their photoluminescence (PL) was too weak for us to quantitatively distinguish between the "on" and "off" events. Clearly, the on dwell times of cation-exchanged CIS QDs become longer as the amount of $Zn(St)_2$ used was increased. The off dwell time becomes shorter as the concentration of $Zn(St)_2$ increases from 0.1 mmol to 4

mmol. Interestingly, there is not much difference in the off dwell times between 1mmol and 2mmol $Zn(St)_2$, but there is a large change between 2mmol and 4mmol $Zn(St)_2$. This is in contrast to the on dwell times, which show more difference between 1 and 2mmol $Zn(St)_2$ than between 2mmol and 4mmol $Zn(St)_2$.

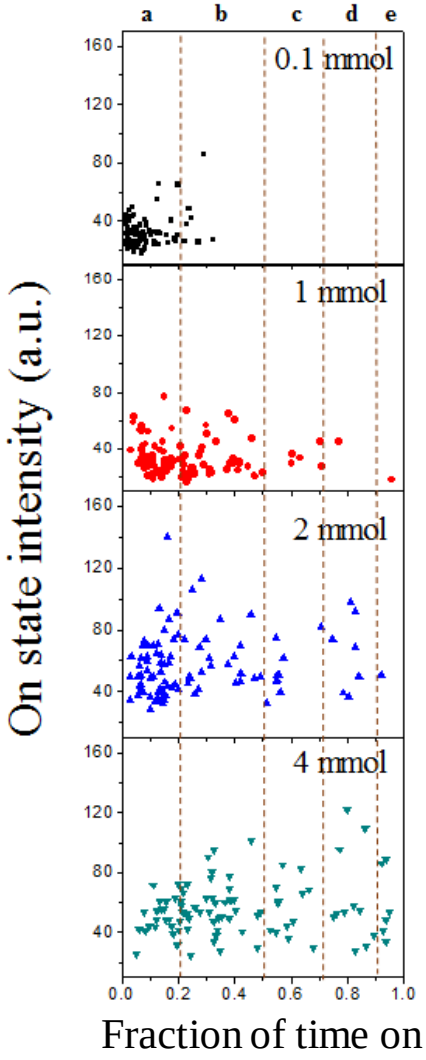

Figure 2.7. Scatter plot of on time intensity vs on time fraction of CIS QDs after cation exchange using different amounts of $Zn(St)_2$.

The data from figure 2.6 represents the accumulated/averaged data from over 100 random single QDs for each curve. Figure 2.7 shows scatter plots for the fraction of time a QD spends in the on

state versus the intensity of the on-state, giving an excellent indication of the degree of heterogeneity in the blinking behavior. In this figure, fraction of time on is calculated as the fraction of the total observation time of approximately 5 mins that the QD is on for. In other words, to be considered as having been on for 50% of the observation time, a QD has to be at on state for 2.5 mins (non-continuously). As expected from the data shown in figure 2.6, the trend shows that the higher the amount of $Zn(St)_2$ used during cation exchange, the more QDs have a higher fraction of their time in the on state. Almost all of the QDs are on for <20% of the time when only 0.1mmol $Zn(St)_2$ is used, whereas ~35% of the QDs are on for >50% of the time and ~20% are on for >70% of the time when 4mmol $Zn(St)_2$ is used. However, the scatter plots show that there is significant heterogeneity in the fraction of time a single QD spends on as more $Zn(St)_2$ is used for cation exchange. Clearly the heterogeneity in blinking is largely static rather than dynamic heterogeneity, which likely results from variations in the composition of the QDs due to the cation exchange process. Figure 2.7 shows that there is also a great deal of scatter in the on-state intensity from QD-to-QD with little-to-no dependence on the blinking dynamics.

We then perfomed a subpopulation analysis on these QDs to further elucidate the underlying mechanisms responsible for this heterogeneous blinking behavior upon cation exchange with Zn. The sub-populations of QDs that show fraction of on-times <20%, 20-50%, 50-70%, 70-90% and >90% are separately analyzed for their blinking statistics. This analysis is shown in figure 2.8. Here, differences in the blinking mechanisms become very apparent. With low amounts of $Zn(St)_2$ used for cation exchange (0.1 mmol), there are only populations that show fractions of time on <20% and between 20-50%, with the 20-50% fraction showing longer on-dwell times and shorter off dwell times, as expected. As 1mmol $Zn(St)_2$ is used, a number of QDs now fall in the 50-70%

range, with only a single QD in the >90% range, as seen in figure 2.7. There are not enough on-off-on transition events in this single QD to provide statistically relevant data, and so is excluded. As 2-4 mmol $Zn(St)_2$ is used, there are now significant numbers of QDs in each range of the fraction of time on, with the curves showing longer on dwell times and shorter off dwell times as the fraction of time spent on increases. The effect on the on dwell times is much stronger than for the off dwell times, including a more obvious change in the shape of the curves. Furthermore, there are no significant differences in the blinking dynamics in a given subpopulation range for each sample; only the relative number of QDs in each range varies with the amount of $Zn(St)_2$ used. This indicates that as more $Zn(St)_2$ is used, there is a prevalence for more QDs to adopt a structure that results in longer on times, although some QDs are not able to achieve it.

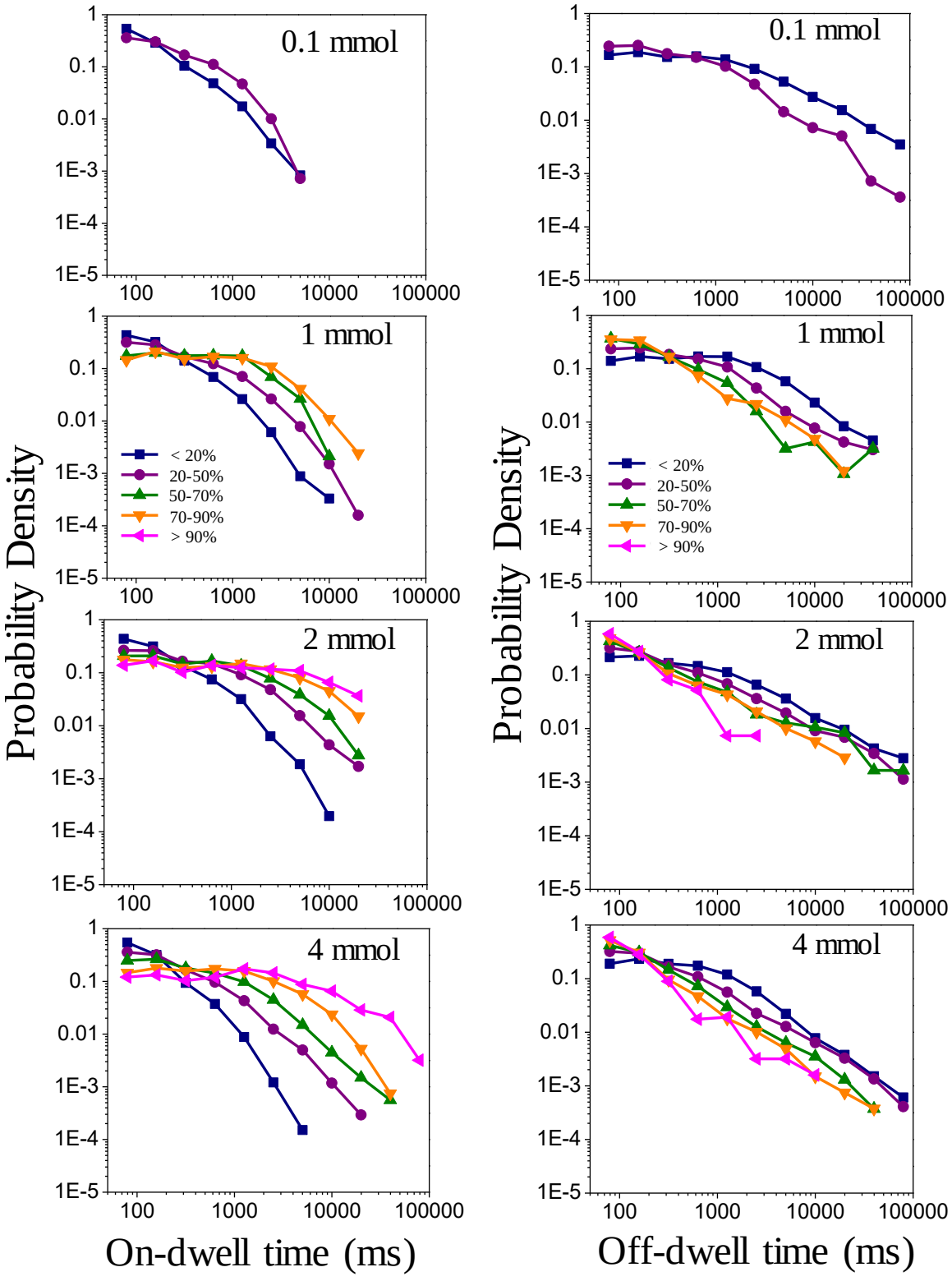

Figure 2.8. Sub-population analysis of blinking statistics showing probability density for on dwell times (left) and off dwell times (right) of CIS-doped ZnS QDs as a function of the amount of $Zn(St)_2$ used.

A great deal of effort has gone into studying the blinking dynamics in CdSe-based QDs. The probability density for on or off times (P_{on} or P_{off}) versus dwell time was originally proposed to fit to an inverse power law function that collapses to an exponential at longer timescales ($P_{on} = At^{-m}e^{-\frac{t}{\tau}}$).[23, 28, 30, 58-60] More recent studies have questioned the power law model, and instead proposed that a multiexponential model is more suitable[31, 61] particularly as far as the on dwell times are concerned ($P_{on} = \sum_i A_i e^{-\frac{t}{\tau_i}}$). Our group recently compared the reduced-χ^2 values when fitting CdSe-based core/shell QDs to both models and found that on dwell times do fit better to multiexponential model than inverse power law, although it was not possible to distinguish between the models for the off dwell times.[31] In figure 2.9, we overlaid simulated blinking curves of the on dwell times using both functions, and find that the subpopulation analysis blinking data can be explained in terms of either reducing the number of exponential terms from 5 to 1 or as decreasing the power law exponent from -1.5 to 0. In both models however, the magenta curves,

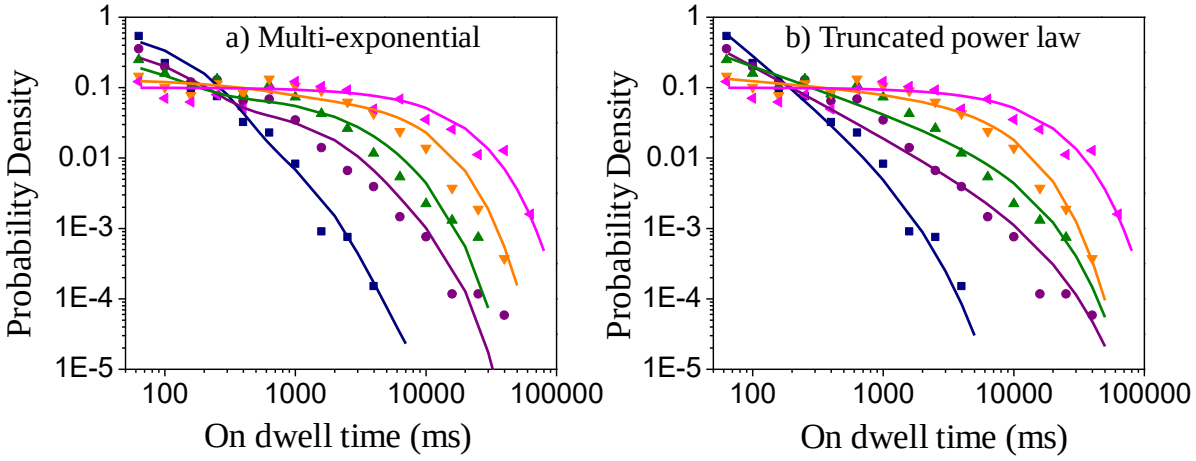

Figure 2.9. Overlay of blinking data for on dwell times with curves simulated using a) multiexponential or b) truncated power law functions. In a) the number of exponential terms is decreased from 5 (navy), to 4 (plum), to 3 (green) to 2 (orange) to 1 (magenta). In b) the power law slope is decreased from -1.5 (navy), to -1.0 (plum), to -0.65 (green), to -0.15 (orange), to 0 (magenta).

representing the least-blinking QDs that are on for >90% of the time, collapses to a mono-exponential curve.

2.5. Discussion

Previous reports on adding Zn to CIS cores resulted in CIS/ZnS core/shell materials which passivated the core surfaces to reduce surface traps to increase QY and reduce blinking.[43-44] In those reports, a blue shift was also observed. In ref 43 a ~75nm blue-shift was observed and in ref 44, a ~66 nm blue shift was observed. In this study the blue-shift observed was 60-100 nm, resulting from more complete cation exchange as the XRD and elemental analysis revealed. In ref 43 zinc was first injected at 200°C, followed by injection of more Zn at 220°C. A similar approach was used in ref 44, with a first injection of Zn at 210°C, followed by a second injection at 230°C. In this report, we avoided the slow, hot-injection steps by adding $Zn(St)_2$ at room temperature and then heating the solution to 230°C. In both refs 43 and 44, the obtained particles were much more anisotropic than those reported here. Thus, our approach led to more isotropic particles, avoided the slow hot injection step and still attained comparable PL QYs. These conditions also resulted in a more complete cation exchange as a result of the higher amounts of zinc used. The ratio of (Cu+In):Zn in ref 43 reached a maximum of ~1:23 (reported as Cu:In:Zn of 1.00:1.13:48.52) and in ref 44 reached levels of ~1:38. For the particles synthesized here, the (Cu+In):Zn ratios reached ~1:136 for the samples using 4 mmol $Zn(St)_2$. This reduced to 1:110 for 2 mmol $Zn(St)_2$, 1:62 for 1 mmol $Zn(St)_2$, and 1:6.8 for 0.1 mmol $Zn(St)_2$. Thus, only the samples synthesized with 0.1 mmol $Zn(St)_2$ and 1 mmol are comparable in zinc composition to the QD reported in refs 43 and 44, although they also showed much greater blinking than the more extensively exchanged

particles, and thus may still be core/shell in architecture. The more extensively cation exchanged QDs (using 2-4 mmol $Zn(St)_2$) are more than 99% ZnS and thus are more accurately characterized as doped QDs in which very small CIS emitting centers, possibly only a few unit cells in size, exist in a ZnS zinc blende lattice.

It is important to recognize that, in addition to the increase in Zn during cation exchange, there is also a change in the Cu:In ratio (table 2.1 and figure 2.5). Adding 0.1 mmol Zn increases the In:Cu ratio, leading to a relative decrease in the amount of Cu^{1+} ions compared to Cu^{2+} ions. This suggests that the Cu^{1+} ions are located closer to the surface of the initial CIS particles than Cu^{2+} ions, allowing for easier cation exchange with Zn. The PL QY of In-rich CIS QDs are known be higher than stoichiometry CIS.[47] Our results suggest that these In-rich CIS QDs have a Cu^{2+} rich center and a Cu^{1+}-rich surface. During cation exchange, it is necessary to exchange either one Cu^{1+} and one In^{3+} ions for two Zn^{2+} or two Cu^{1+} ions per Zn^{2+}. The data suggests that the latter process occurs more favorably than the former when lower amounts of Zn is added, although both processes do occur since the In content is also reduced. This preferential exchange initially enriches the In:Cu ratio and increases the number of copper vacancies. This formation of a Zn-enriched surface is similar to the core/shell structures reported previously.[43-44] As more Zn is added, the Cu and In composition drastically reduces to less than 1% when 4 mmol $Zn(St)_2$ is used. This also leads to a slight decrease in the In:Cu ratio (although still higher than the 4:1 ratio in the initial CIS) and thus the Cu^{2+}:Cu^{1+} ratio, as the lattice becomes almost pure zinc blende ZnS with small clusters of CIS effectively acting as dopant. These small CIS clusters may also diffuse within the ZnS lattice as they search for local minima in their energy, as is common for dopants, with

some dopant clusters in the center and some closer to the surface. This exchange process is depicted in figure 2.10.

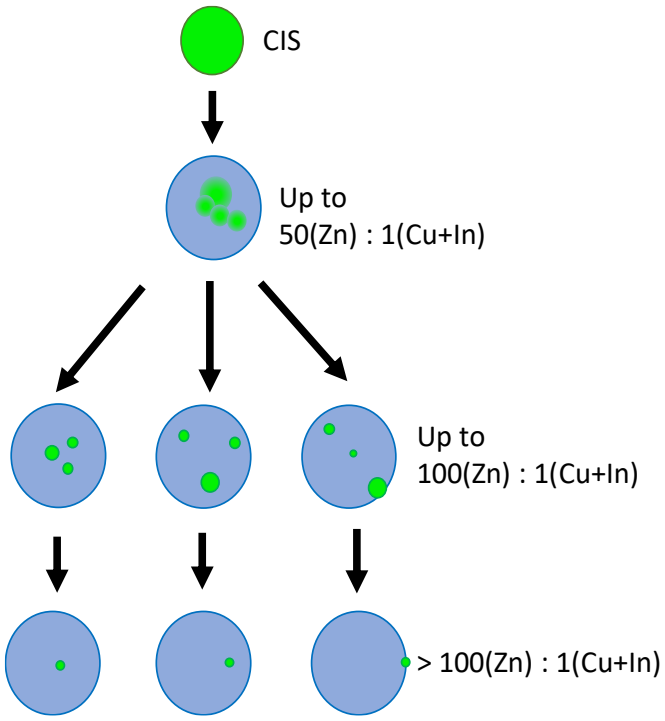

Figure 2.10. Schematic depiction of the cation exchange process in CIS QDs as the amount of Zn increases. Initially, core/shell-like structures are formed, but as more cation exchange occurs, the CIS exist as small dopant clusters at various sites in a ZnS lattice.

Figure 2.2 shows that the ensemble PL peak blue shifts and becomes narrower upon cation exchange. The model in figure 2.10 shows the CIS cluster becoming smaller with more extensive cation exchange, which leads to the blue shift. The leveling off occurs when the cluster become so small that they become more molecule-like in behavior where quantum confinement effects are at a maximum and no longer depend on size. Recently, Zang et al. explained the main reason for the large ensemble PL line width of CIS and thick-shell CIS/ZnS QDs is not intrinsic but rather due to sample heterogeneity.[44] They suggested that this phenomenon is due to a random positioning of the Cu-related emission centers within the QDs, which leads to large variations in the contribution from the electron−hole Coulomb interaction energy translating into a varied PL energy. The model

depicted in figure 2.10 can also be used to explain the narrowing of the peak width with more extensive cation exchange since the clusters become more homogeneous in size, reducing the variations in electron−hole Coulomb interaction energy.

Reconciling the ensemble fluorescence properties with the single particle properties has always presented a challenge. We have previously reported significant discrepancies with the ensemble and single particle properties of Cd-based core/shell and core/multishell QDs as a function of pH[28, 62] and of the shell architecture.[31] The dark fraction and the various radiative and non-radiative lifetimes of the different emitting states play roles in this discrepancy. In this study, ensemble PL QY increased upon adding Zn to CIS QDs but higher ensemble PL QYs are observed for the less extensively exchanged QDs while blinking is only reduced upon more extensive cation exchange. In order to connect the structural models of figure 2.10 with the electronic structures that leads to the various optical properties (PL peak shift and width, PL QY, fluorescence lifetimes and blinking) we started from the recent models describing the different recombination pathways for Cu^{2+} and Cu^{1+} centers[56-57] and examined how the formation of CIS dopant centers at various positions in a ZnS lattice formed by extensive cation exchange would affect them. The relationship between the CIS emitting center location within the ZnS lattice and the excitonic decay pathways is presented in figure 2.11.

Emission occurs when the conduction band (CB) electron radiatively recombines with hole intraband states at copper centers within the QD, which is a slow process and competes with non-radiative recombination due to surface trapping of charge carriers. During the cation exchange, the ensemble PL QY increases when 0.1 mmol $Zn(St)_2$ but decreases as up to 4 mmol $Zn(St)_2$ is used (figure 2.1). It was previously reported that changing the Cu:In ratio during synthesis of CIS leads

to a changes in the Cu^{1+}:Cu^{2+} ratio, which significantly affects the quantum yield through changing

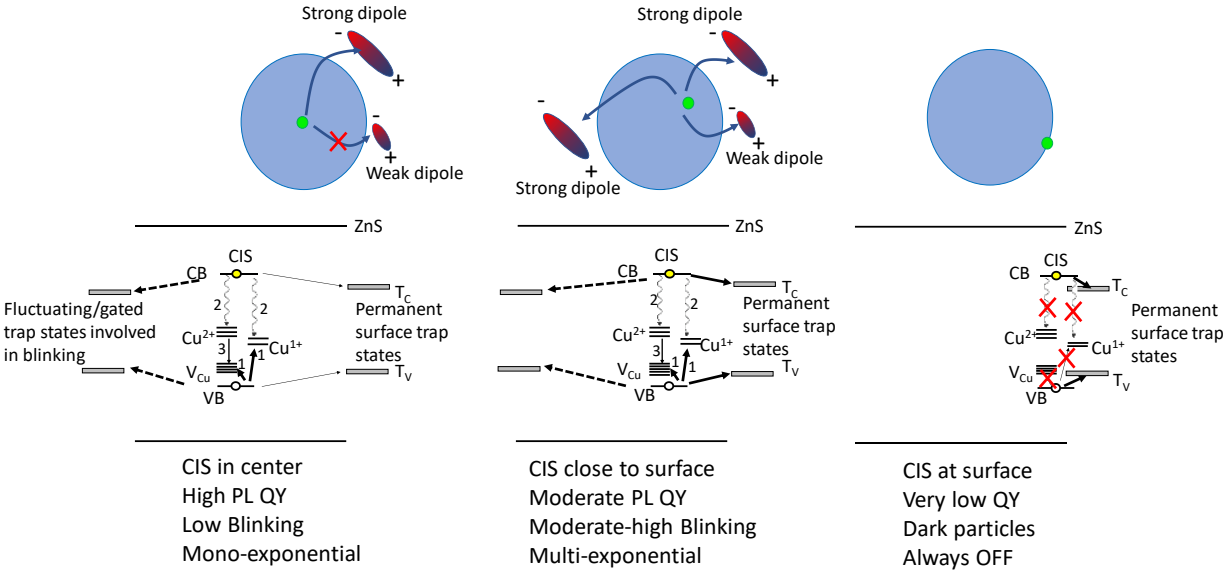

Figure 2.11. Schematic depiction of the relationship between CIS cluster location and electronic structure and excitonic decay pathways. As described in ref 53 and ref 54, holes are first transferred to Cu^{1+} centers or copper vacancies in Cu^{2+} centers (1), then radiative recombination (2) occurs when electrons in the conduction band of CIS recombine with these holes. In the case of Cu^{2+}, a third step is needed where the electron is subsequently transferred to the copper vacancy site (3). In our model, CIS emitting centers near the center of the QD have high probabilities of radiative recombination due to being isolated from permanent surface trap states, resulting in high PL QY. When CIS clusters are at the surface of the QD, trapping dominates and the QDs are permanently non-emissive (dark particles). For the emissive particles, fluctuating dipoles at the surface result in gated trap states that are involved in blinking. As the CIS cluster is more centralized, blinking is slow and mono-exponential due to the large distance of the emitting center to the fluctuating dipoles at the surface requiring strong dipoles to lead to trapping. As the CIS cluster is closer to the surface (but not at the surface where it is always dark), the distance to the fluctuating dipoles is more heterogeneous, and weaker dipoles can also lead to trapping, resulting in multi-exponential blinking dynamics.

the electron and hole relaxation pathways.[56-57] In this study, there is an enrichment in the In:Cu ratio upon cation exchange with Zn, which also increases the ensemble PL QY in addition to decreasing the accessibility of excitons to surface traps as a ZnS shell-like layer begins to form (first step in figure 2.10). Although the QDs remain relatively isotropic and do not increase in size significantly (figure 2.3), the morphology of the CIS emitting sites within the QD is likely not completely spherical due to the likelihood of non-isotropic cation exchange, and is depicted as

such in figure 2.10. Once more extensive cation exchange occurs (1 mmol $Zn(St)_2$ and above), the In-richness decreases slightly compared to 0.1 mmol $Zn(St)_2$, although it is still higher than the initial CIS. Furthermore, the Zn content is now high enough (over 98%) that the CIS centers are more accurately considered as small CIS clusters in a ZnS lattice rather than core/shell, possibly only several tens of atoms which is analogous to previous reports of Ag and Au clusters[70, 71] and thus reaching the level of being considered CIS-doped ZnS QDs. In this scenario, while the sizes of the CIS clusters are more homogeneous, the positional distribution in the CIS center within the QD is very heterogeneous. Those QDs with the CIS in the center of the QD are well isolated from permanent surface trap states so that the probability of radiative recombination (PL QY) is high. The closer the CIS cluster to the QD surface, the more accessibility the electron and holes have to permanent surface traps that limits single QD brightness (figure 2.7). When the CIS is at the surface, this leads to a particle where surface trapping dominates and the QD is always dark and thus not observable in a single particle experiment but contributes to the lowering of the ensemble PL QY. Another possibility is that at high concentration of Zn there are many permanent trap states at the interface, which also lead to dark QDs.

Although the PL QY increases more for less extensive cation exchange, QD blinking decreases more with more extensively exchanged QDs, and so does heterogeneity. This heterogeneity in blinking can also be explained in terms of heterogeneity in the location of the CIS centers within the QD, with significant populations of dark, high blinking and low blinking particles. To explain blinking, it is necessary to invoke trap states that are temporary in nature, either in terms of their formation or in terms of their accessibility. Several possible mechanisms to explain this have been proposed based on Cd-based QDs. These include stochastic variation in trapping rates to external

traps leading to charged QDs,[63] Diffusion Controlled Electron Transfer (DCET),[58] stochastic diffusion of excited state electronic energies to be in or out of resonance energy with hole trap states that leads to Auger-assisted trapping,[64] hole/electron trapping leading to trion formation[21, 65-68] and gated multiple recombination centers.[32, 61, 69] Of these mechanisms, the one that can be most easily described in the context of the schematic depiction of figure 2.11 is that of gated multiple recombination centers, particularly based on the model presented by Schmidt et al.[61] In that model, fluctuating dipoles that can trap either electrons or holes that have multiple timescales account for multi-exponential blinking dynamics. In order to extend this model to our system, it is necessary to describe the transition from multi-exponential (fast blinking) to single exponential (slow blinking) kinetics for the on state (figure 2.9). This can be explained by considering that the fluctuating dipoles can have a range of strengths. When the CIS is at the center of the QD, only the strongest dipoles have fields that can penetrate to the center of the ZnS to allow trapping of electrons or holes. However, the closer the CIS is to the QD surface, the less strong the dipole needs to be to trap the charge carriers so that weaker dipoles can now be involved, shortening the on dwell times. Clearly, when the CIS is close to the surface, strong dipoles on the opposite side of the QD to where the CIS center resides (see center panel of figure 2.11) can still lead to trapping and formation of an off state. These multiple (fluctuating) trapping rates are expected to lead to multi-exponential behavior in such a model.

This model can also be used to explain the weaker dependence on the off dwell time distribution. Once the charge carrier is trapped, the length of time it remains trapped depends only on the length of time the dipole exists, which is likely to depend much weaker on the position of the CIS. The off dwell time distributions do not appear to collapse to a single exponential, but the fastest

blinking QDs (<20% and between 20-50% fraction of time on) change slope (exponents) at shorter timescales. Tang and Marcus predicted the change in power law exponent as indicative of a DCET mechanism,[58] which was subsequently supported experimentally by Pelton et. al.[60] and Durisic et. al.,[28] although those reports applied them to the on-dwell times. In the context of our proposed mechanism, diffusion of the dipole on the surface may lead to a distribution in the recapture rates that may be explained in the context of a DCET-type model but exploring this possibility will require more studies.

The ensemble fluorescence lifetime increases mostly in line with the ensemble PL QY (figure 2.1), although the changes are not completely correlative, indicating that the average radiative and non-radiative rates change in a more complex manner, and vary depending on the time of the cation exchange reaction (figure 2.1). One possible explanation for this is that the radiative and non-radiative rates of the emission processes at the Cu^{1+} and Cu^{2+} sites are different depending on the exact location of the CIS emitting center in the ZnS lattice. As discussed above, the relative changes in Cu:In ratio with cation exchange suggest Cu^{1+} is preferentially located closer to the surface and thus more likely to lead to non-radiative recombination than at more central Cu^{2+} sites. This hypothesis can be further investigated by a single particle fluorescence lifetime analysis, which we plan to undertake in a subsequent study.

2.6. Conclusions

Relatively small and isotropic CIS-based QDs were synthesized through a non-injection synthetic method with zinc stearate. The resulting ensemble optical properties such as PL QY are comparable to the currently used hot injection approaches but have the advantage of being more

applicable to scaling up. Extensive cation exchange was observed, depending on the amount of Zn precursor used, eventually leading to small clusters of emitting CIS in a mostly ZnS lattice. As the cation exchange become more extensive, blinking was reduced but heterogeneity from QD-to-QD increased. A sub-population analysis showed that the least blinking QDs showed mono-exponential blinking dynamics compared to multi-exponential (or inverse power law) dynamics in the QD that showed faster blinking. A model was proposed that described the relationship between the blinking behavior and the underlying QD structure responsible. Our model suggests that the "dark fraction" formation and the blinking dynamics both have their origin in the location of the CIS recombination center within the QD lattice. These results will help provide a framework to design large scale production approaches to Cd-free QDs in which blinking and other optical properties can be more accurately controlled.

Acknowledgements

Generous financial support by the NSF (CHE-1255440), the NIH (COBRE P30 GM103450) and the Arkansas Biosciences Institute is gratefully acknowledged. TEM instrumentation access is provided by the Arkansas Materials Characterization Facility (funded in part by the NSF) and the Institute of Nanoscience and Engineering at the University of Arkansas. We would also like to thank Erik Pollack in the trace element and radiogenic isotope lab, TRAIL, for help with the ICP-MS experiments.

2.7. References

1. Jaiswal, J. K.; Mattoussi, H.; Mauro, J. M.; Simon, S. M. Long-term Multiple Color Imaging of Live Cells using Quantum Dot Bioconjugates. *Nat. Biotechnol.* **2003,** *21*, 47-51.

2. Alivisatos, P. The Use of Nanocrystals in Biological Detection. *Nat. Biotechnol.* **2004,** *22*, 47-52.

3. le Feber, B.; Prins, F.; De Leo, E.; Rabouw, F. T.; Norris, D. J. Colloidal-Quantum-Dot Ring Lasers with Active Color Control. *Nano Lett.* **2018,** *18*, 1028-1034.

4. Giovanella, U.; Pasini, M.; Lorenzon, M.; Galeotti, F.; Lucchi, C.; Meinardi, F.; Luzzati, S.; Dubertret, B.; Brovelli, S. Efficient Solution-Processed Nanoplatelet-Based Light-Emitting Diodes with High Operational Stability in Air. *Nano Lett.* **2018,** *18*, 3441-3448.

5. Zhang, X.; Santra, P. K.; Tian, L.; Johansson, M. B.; Rensmo, H.; Johansson, E. M. J. Highly Efficient Flexible Quantum Dot Solar Cells with Improved Electron Extraction Using MgZnO Nanocrystals. *ACS Nano* **2017,** *11*, 8478-8487.

6. Grieve, K.; Mulvaney, P.; Grieser, F. Synthesis and Electronic Properties of Semiconductor Nanoparticles/Quantum dots. *Curr. Opin. Colloid Interface Sci.* **2000,** *5*, 168-172.

7. Pietryga, J. M.; Park, Y.-S.; Lim, J.; Fidler, A. F.; Bae, W. K.; Brovelli, S.; Klimov, V. I. Spectroscopic and Device Aspects of Nanocrystal Quantum Dots. *Chem. Rev.* **2016,** *116*, 10513-10622.

8. Heyes, C. D. Chapter 4 - Quantum Dots in Single Molecule Spectroscopy. In *Spectroscopy and Dynamics of Single Molecules*, Johnson, C. K., Ed. Elsevier: 2019; pp 163-228.

9. McDonald, S. A.; Konstantatos, G.; Zhang, S.; Cyr, P. W.; Klem, E. J. D.; Levina, L.; Sargent, E. H. Solution-Processed PbS Quantum Dot Infrared Photodetectors and Photovoltaics. *Nat. Mater.* **2005,** *4*, 138-142.

10. Yong, K.-T.; Ding, H.; Roy, I.; Law, W.-C.; Bergey, E. J.; Maitra, A.; Prasad, P. N. Imaging Pancreatic Cancer Using Bioconjugated InP Quantum Dots. *ACS Nano* **2009,** *3*, 502-510.

11. Franke, D.; Harris, D. K.; Chen, O.; Bruns, O. T.; Carr, J. A.; Wilson, M. W. B.; Bawendi, M. G. Continuous Injection Synthesis of Indium Arsenide Quantum Dots Emissive in the Short-Wavelength Infrared. *Nat. Commun.* **2016,** *7*, 12749.

12. Allen, P. M.; Liu, W.; Chauhan, V. P.; Lee, J.; Ting, A. Y.; Fukumura, D.; Jain, R. K.; Bawendi, M. G. InAs(ZnCdS) Quantum Dots Optimized for Biological Imaging in the Near-Infrared. *J. Am. Chem. Soc.* **2010,** *132*, 470-471.

13. Lane, L. A.; Smith, A. M.; Lian, T.; Nie, S. Compact and Blinking-Suppressed Quantum Dots for Single-Particle Tracking in Live Cells. *J. Phys. Chem. B* **2014,** *118*, 14140-14147.

14. Keller, A. M.; Ghosh, Y.; DeVore, M. S.; Phipps, M. E.; Stewart, M. H.; Wilson, B. S.; Lidke, D. S.; Hollingsworth, J. A.; Werner, J. H. 3-Dimensional Tracking of Non-blinking 'Giant' Quantum Dots in Live Cells. *Adv. Funct. Mater.* **2014,** *24*, 4796-4803.

15. Chandrasekaran, V.; Tessier, M. D.; Dupont, D.; Geiregat, P.; Hens, Z.; Brainis, E. Nearly Blinking-Free, High-Purity Single-Photon Emission by Colloidal InP/ZnSe Quantum Dots. *Nano Lett.* **2017,** *17*, 6104-6109.

16. Nirmal, M.; Dabbousi, B. O.; Bawendi, M. G.; Macklin, J. J.; Trautman, J. K.; Harris, T. D.; Brus, L. E. Fluorescence Intermittency in Single Cadmium Selenide Nanocrystals. *Nature* **1996,** *383*, 802.

17. Mahler, B.; Spinicelli, P.; Buil, S.; Quelin, X.; Hermier, J.-P.; Dubertret, B. Towards Non-Blinking Colloidal Quantum Dots. *Nat. Mater.* **2008,** *7*, 659-664.

18. Chen, Y.; Vela, J.; Htoon, H.; Casson, J. L.; Werder, D. J.; Bussian, D. A.; Klimov, V. I.; Hollingsworth, J. A. "Giant" Multishell CdSe Nanocrystal Quantum Dots with Suppressed Blinking. *J. Am. Chem. Soc.* **2008,** *130*, 5026-5027.

19. Chen, O.; Zhao, J.; Chauhan, V. P.; Cui, J.; Wong, C.; Harris, D. K.; Wei, H.; Han, H. S.; Fukumura, D.; Jain, R. K.; Bawendi, M. G. Compact High-Quality CdSe-CdS Core-Shell Nanocrystals with Narrow Emission Linewidths and Suppressed Blinking. *Nat. Mater.* **2013,** *12*, 445-451.

20. Qin, H.; Niu, Y.; Meng, R.; Lin, X.; Lai, R.; Fang, W.; Peng, X. Single-Dot Spectroscopy of Zinc-Blende CdSe/CdS Core/Shell Nanocrystals: Nonblinking and Correlation with Ensemble Measurements. *J. Am. Chem. Soc.* **2014,** *136*, 179-187.

21. Omogo, B.; Gao, F.; Bajwa, P.; Kaneko, M.; Heyes, C. D. Reducing Blinking in Small Core-Multishell Quantum Dots by Carefully Balancing Confinement Potential and Induced Lattice Strain: The "Goldilocks" Effect. *ACS Nano* **2016,** *10*, 4072-4082.

22. Bharadwaj, P.; Novotny, L. Robustness of Quantum Dot Power-Law Blinking. *Nano Lett.* **2011,** *11*, 2137-2141.

23. Shimizu, K. T.; Neuhauser, R. G.; Leatherdale, C. A.; Empedocles, S. A.; Woo, W. K.; Bawendi, M. G. Blinking Statistics in Single Semiconductor Nanocrystal Quantum Dots. *Phys. Rev. B* **2001,** *63*, 205316.

24. Issac, A.; Krasselt, C.; Cichos, F.; von Borczyskowski, C. Influence of the Dielectric Environment on the Photoluminescence Intermittency of CdSe Quantum Dots. *ChemPhysChem* **2012,** *13*, 3223-3230.

25. von Borczyskowski, C.; Cichos, F.; Martin, J.; Schuster, J.; Issac, A.; Brabandt, J. Common Luminescence Intensity Fluctuations of Single Particle and Single Molecules in Non-Conducing Matrices. *The Eur. Phys. J. Spec. Top.* **2007,** *144*, 13-25.

26. Jin, S.; Song, N.; Lian, T. Suppressed Blinking Dynamics of Single QDs on ITO. *ACS Nano* **2010,** *4*, 1545-1552.

27. Yuan, C.-T.; Chou, W.-C.; Chen, Y.-N.; Chou, J.-W.; Chuu, D.-S.; Lin, C.-A. J.; Li, J. K.; Chang, W. H.; Shen, J.-L. Study of Fluorescence Enhancement of Colloidal CdSe/ZnS Quantum Dots Bound to Hexadecylamine by Single-Molecule Measurements. *J. Phys. Chem. C* **2007,** *111*, 15166-15172.

28. Durisic, N.; Wiseman, P. W.; Grütter, P.; Heyes, C. D. A Common Mechanism Underlies the Dark Fraction Formation and Fluorescence Blinking of Quantum Dots. *ACS Nano* **2009,** *3*, 1167-1175.

29. Xie, R.; Kolb, U.; Li, J.; Basché, T.; Mews, A. Synthesis and Characterization of Highly Luminescent CdSe−Core CdS/$Zn_{0.5}Cd_{0.5}$S/ZnS Multishell Nanocrystals. *J. Am. Chem. Soc.* **2005,** *127*, 7480-7488.

30. Heyes, C. D.; Kobitski, A. Y.; Breus, V. V.; Nienhaus, G. U. Effect of the Shell on the Blinking Statistics of Core-Shell Quantum Dots: A Single-Particle Fluorescence Study. *Phys. Rev. B* **2007,** *75*, 125431.

31. Bajwa, P.; Gao, F.; Nguyen, A.; Omogo, B.; Heyes, C. D. Influence of the Inner-Shell Architecture on Quantum Yield and Blinking Dynamics in Core/Multishell Quantum Dots. *ChemPhysChem* **2016,** *17*, 731-740.

32. Gao, F.; Bajwa, P.; Nguyen, A.; Heyes, C. D. Shell-Dependent Photoluminescence Studies Provide Mechanistic Insights into the Off-Grey-On Transitions of Blinking Quantum Dots. *ACS Nano* **2017,** *11*, 2905-2916.

33. Xie, R.; Rutherford, M.; Peng, X. Formation of High-Quality I−III−VI Semiconductor Nanocrystals by Tuning Relative Reactivity of Cationic Precursors. *J. Am. Chem. Soc.* **2009,** *131*, 5691-5697.

34. Li, L.; Pandey, A.; Werder, D. J.; Khanal, B. P.; Pietryga, J. M.; Klimov, V. I. Efficient Synthesis of Highly Luminescent Copper Indium Sulfide-Based Core/Shell Nanocrystals with Surprisingly Long-Lived Emission. *J. Am. Chem. Soc.* **2011,** *133*, 1176-1179.

35. Akdas, T.; Walter, J.; Segets, D.; Distaso, M.; Winter, B.; Birajdar, B.; Spiecker, E.; Peukert, W. Investigation of the Size-Property Relationship in $CuInS_2$ Quantum Dots. *Nanoscale* **2015,** *7*, 18105-18118.

36. Chen, C.-W.; Wu, D.-Y.; Chan, Y.-C.; Lin, C. C.; Chung, P.-H.; Hsiao, M.; Liu, R.-S. Evaluations of the Chemical Stability and Cytotoxicity of $CuInS_2$ and $CuInS_2$/ZnS Core/Shell Quantum Dots. *J. Phys. Chem. C* **2015,** *119*, 2852-2860.

37. Li, L.; Daou, T. J.; Texier, I.; Kim Chi, T. T.; Liem, N. Q.; Reiss, P. Highly Luminescent $CuInS_2$/ZnS Core/Shell Nanocrystals: Cadmium-Free Quantum Dots for In Vivo Imaging. *Chem. Mater.* **2009,** *21*, 2422-2429.

38. Pons, T.; Pic, E.; Lequeux, N.; Cassette, E.; Bezdetnaya, L.; Guillemin, F.; Marchal, F.; Dubertret, B. Cadmium-free $CuInS_2$/ZnS Quantum Dots for Sentinel Lymph Node Imaging with Reduced Toxicity. *ACS Nano* **2010,** *4*, 2531-2538.

39. Gao, X.; Liu, X.; Lin, Z.; Liu, S.; Su, X. $CuInS_2$ Quantum Dots as a Near-Infrared Fluorescent Probe for Detecting Thrombin in Human Serum. *Analyst* **2012,** *137*, 5620-5624.

40. Mandal, G.; Darragh, M.; Wang, Y. A.; Heyes, C. D. Cadmium-free Quantum Dots as Time-Gated Bioimaging Probes in Highly-Autofluorescent Human Breast Cancer Cells. *Chem. Commun.* **2013,** *49*, 624-626.

41. Chuang, P. H.; Lin, C. C.; Liu, R. S. Emission-Tunable $CuInS_2$/ZnS Quantum Dots: Structure, Optical Properties, and Application in White Light-Emitting Diodes with High Color Rendering Index. *ACS Appl. Mater. Inter.* **2014,** *6*, 15379-15387.

42. Li, C.; Chen, W.; Wu, D.; Quan, D.; Zhou, Z.; Hao, J.; Qin, J.; Li, Y.; He, Z.; Wang, K. Large Stokes Shift and High Efficiency Luminescent Solar Concentrator Incorporated with $CuInS_2$/ZnS Quantum Dots. *Sci. Rep.* **2015,** *5*, 17777.

43. Zhang, A.; Dong, C.; Li, L.; Yin, J.; Liu, H.; Huang, X.; Ren, J. Non-blinking (Zn)CuInS/ZnS Quantum Dots Prepared by In Situ Interfacial Alloying Approach. *Sci. Rep.* **2015,** *5*, 15227.

44. Zang, H.; Li, H.; Makarov, N. S.; Velizhanin, K. A.; Wu, K.; Park, Y. S.; Klimov, V. I. Thick-Shell $CuInS_2$/ZnS Quantum Dots with Suppressed "Blinking" and Narrow Single-Particle Emission Line Widths. *Nano Lett.* **2017,** *17*, 1787-1795.

45. Nam, D. E.; Song, W. S.; Yang, H. Noninjection, One-pot Synthesis of Cu-Deficient $CuInS_2$/ZnS Core/Shell Quantum Dots and their Fluorescent Properties. *J. Colloid Interface Sci.* **2011,** *361*, 491-496.

46. Zhong, H.; Lo, S. S.; Mirkovic, T.; Li, Y.; Ding, Y.; Li, Y.; Scholes, G. D. Noninjection Gram-Scale Synthesis of Monodisperse Pyramidal $CuInS_2$ Nanocrystals and Their Size-Dependent Properties. *ACS Nano* **2010,** *4*, 5253-5262.

47. Chen, B.; Zhong, H.; Zhang, W.; Tan, Z. a.; Li, Y.; Yu, C.; Zhai, T.; Bando, Y.; Yang, S.; Zou, B. Highly Emissive and Color-Tunable $CuInS_2$-Based Colloidal Semiconductor Nanocrystals: Off-Stoichiometry Effects and Improved Electroluminescence Performance. *Adv. Funct. Mater.* **2012,** *22*, 2081-2088.

48. Chuang, P.-H.; Lin, C. C.; Liu, R.-S. Emission-Tunable $CuInS_2$/ZnS Quantum Dots: Structure, Optical Properties, and Application in White Light-Emitting Diodes with High Color Rendering Index. *ACS Appl. Mater. Interfaces* **2014,** *6*, 15379-15387.

49. Song, W.-S.; Yang, H. Efficient White-Light-Emitting Diodes Fabricated from Highly Fluorescent Copper Indium Sulfide Core/Shell Quantum Dots. *Chem. Mater.* **2012,** *24*, 1961-1967.

50. Park, J.; Kim, S.-W. $CuInS_2$/ZnS Core/Shell Quantum Dots by Cation Exchange and their Blue-Shifted Photoluminescence. *J. Mater. Chem.* **2011,** *21*, 3745-3750.

51. Park, S. H.; Hong, A.; Kim, J.-H.; Yang, H.; Lee, K.; Jang, H. S. Highly Bright Yellow-Green-Emitting $CuInS_2$ Colloidal Quantum Dots with Core/Shell/Shell Architecture for White Light-Emitting Diodes. *ACS Appl. Mater. Interfaces* **2015,** *7*, 6764-6771.

52. Tang, X.; Cheng, W.; Choo, E. S. G.; Xue, J. Synthesis of $CuInS_2$–ZnS Alloyed Nanocubes with High Luminescence. *Chem. Commun.* **2011,** *47*, 5217-5219.

53. Nam, D.-E.; Song, W.-S.; Yang, H. Noninjection, One-pot Synthesis of Cu-Deficient $CuInS_2$/ZnS Core/Shell Quantum Dots and their Fluorescent Properties. *J. Colloid Interface Sci.* **2011,** *361*, 491-496.

54. Zhang, J.; Xie, R.; Yang, W. A Simple Route for Highly Luminescent Quaternary Cu-Zn-In-S Nanocrystal Emitters. *Chem. Mater.* **2011,** *23*, 3357-3361.

55. Zhang, A.; Dong, C.; Li, L.; Yin, J.; Liu, H.; Huang, X.; Ren, J. Non-blinking (Zn)CuInS/ZnS Quantum Dots Prepared by In Situ Interfacial Alloying Approach. *Sci. Rep.* **2015,** *5*, 15227.

56. Fuhr, A. S.; Yun, H. J.; Makarov, N. S.; Li, H.; McDaniel, H.; Klimov, V. I. Light Emission Mechanisms in $CuInS_2$ Quantum Dots Evaluated by Spectral Electrochemistry. *ACS Photonics* **2017,** *4*, 2425-2435.

57. van der Stam, W.; de Graaf, M.; Gudjonsdottir, S.; Geuchies, J. J.; Dijkema, J. J.; Kirkwood, N.; Evers, W. H.; Longo, A.; Houtepen, A. J. Tuning and Probing the Distribution of Cu^+ and Cu^{2+} Trap States Responsible for Broad-Band Photoluminescence in $CuInS_2$ Nanocrystals. *ACS Nano* **2018,** *12*, 11244-11253.

58. Tang, J.; Marcus, R. A. Diffusion-Controlled Electron Transfer Processes and Power-Law Statistics of Fluorescence Intermittency of Nanoparticles. *Phys. Rev. Lett.* **2005,** *95*, 107401.

59. Knappenberger, K. L.; Wong, D. B.; Romanyuk, Y. E.; Leone, S. R. Excitation Wavelength Dependence of Fluorescence Intermittency in CdSe/ZnS Core/Shell Quantum Dots. *Nano Lett.* **2007,** *7*, 3869-3874.

60. Pelton, M.; Smith, G.; Scherer, N. F.; Marcus, R. A. Evidence for a Diffusion-Controlled Mechanism for Fluorescence Blinking of Colloidal Quantum Dots. *Proc. Natl. Acad. Sci. U.S.A.* **2007,** *104*, 14249.

61. Schmidt, R.; Krasselt, C.; Göhler, C.; von Borczyskowski, C. The Fluorescence Intermittency for Quantum Dots Is Not Power-Law Distributed: A Luminescence Intensity Resolved Approach. *ACS Nano* **2014,** *8*, 3506-3521.

62. Durisic, N.; Godin, A. G.; Walters, D.; Grütter, P.; Wiseman, P. W.; Heyes, C. D. Probing the "Dark" Fraction of Core–Shell Quantum Dots by Ensemble and Single Particle pH-Dependent Spectroscopy. *ACS Nano* **2011,** *5*, 9062-9073.

63. Kuno, M.; Fromm, D. P.; Johnson, S. T.; Gallagher, A.; Nesbitt, D. J. Modeling Distributed Kinetics in Isolated Semiconductor Quantum Dots. *Phys. Rev. B* **2003,** *67*, 125304.

64. Frantsuzov, P. A.; Marcus, R. A. Explanation of Quantum Dot Blinking without the Long-lived Trap Hypothesis. *Phys. Rev. B* **2005,** *72*, 155321.

65. Galland, C.; Ghosh, Y.; Steinbruck, A.; Sykora, M.; Hollingsworth, J. A.; Klimov, V. I.; Htoon, H. Two Types of Luminescence Blinking Revealed by Spectroelectrochemistry of Single Quantum Dots. *Nature* **2011,** *479*, 203-207.

66. Qin, W.; Shah, R. A.; Guyot-Sionnest, P. CdSeS/ZnS Alloyed Nanocrystal Lifetime and Blinking Studies under Electrochemical Control. *ACS Nano* **2012,** *6*, 912-918.

67. Park, Y.-S.; Bae, W. K.; Pietryga, J. M.; Klimov, V. I. Auger Recombination of Biexcitons and Negative and Positive Trions in Individual Quantum Dots. *ACS Nano* **2014,** *8*, 7288-7296.

68. Yuan, G.; Gómez, D. E.; Kirkwood, N.; Boldt, K.; Mulvaney, P. Two Mechanisms Determine Quantum Dot Blinking. *ACS Nano* **2018,** *12*, 3397-3405.

69. Frantsuzov, P. A.; Volkán-Kacsó, S.; Jankó, B. Model of Fluorescence Intermittency of Single Colloidal Semiconductor Quantum Dots Using Multiple Recombination Centers. *Phys. Rev. Lett.* **2009,** *103*, 207402.

70. Petty, J. T.; Zheng, J.; Hud, N. V.; Dickson R. M. DNA Templated Ag Nanocluster Formation. *J. Am. Chem. Soc.* **2004,** *106*, 5207-5212.

71. Zheng, J.; Petty, J. T.; Dickson R. M. High Quantum Yield Blue Emission from Water-Soluble Au_8 Nanodots.

Compact and blinking Cd-free quantum dots for single-particle super-resolution imaging.

Anh T. Nguyen[#], Dustin Baucom[#], Yong Wang[$] and Colin D. Heyes[#]*

[#]Department of Chemistry and Biochemistry, University of Arkansas, 345 North Campus Drive, Fayetteville, Arkansas 72701, United States

[$]Department of Physics, University of Arkansas, 345 North Campus Drive, Fayetteville, Arkansas 72701, United States

[*]Corresponding author. Email: cheyes@uark.edu

3.1. Abstract

Quantum dots (QDs) can be a potential candidate for fluorescent probes in single molecule localization microscopy as a way to achieve sub-diffraction limit resolution (super-resolution imaging). However, the toxicity of Cd in the prototypical CdSe-based QDs limit their use in biological applications of super resolution imaging. Furthermore, commercial CdSe QDs have been modified with relatively thick shells to render them in the 10-20nm size range, which is relatively large for biological labels. In this report, we present a comparison between compact (4-6 nm) $CuInS_2$/ZnS (CIS/ZnS) and commercially-sourced CdSe/ZnS QDs in their blinking behavior, localization precision and super resolution localization imaging. Although commercial CdSe QDs were brighter than the more compact Cd-free CIS/ZnS QD, both give comparable results when applied to super resolution imaging of actin filaments. The width of actin filaments in super resolution images is less than the diffraction limit, showing a 4.5-fold improvement over conventional TIRF microscope images. We propose that the faster, burst-like blinking of the smaller CIS/ZnS QDs allow for higher density of labeling, which compensates for their lower brightness to result in comparable super-resolution imaging precision. These results demonstrate that CIS/ZnS QDs are an excellent candidate to complement and perhaps even replace the larger and more toxic CdSe-based QDs for robust single-molecule super-resolution imaging.

3.2. Introduction

The Abbé diffraction limit limits conventional imaging reoslution to approximately half of the excitation wavelength. Over recent years, a number of super resolution imaging techniques have been developed to achieve sub-diffraction-limited imaging resolution, so-called super-resolution imaging.[1-2] Some of the well-known super resolution imaging techniques are: i) patterned illumination microscopy such as stimulated emission depletion (STED)[3-4] and ii) single molecule

localization microscopy (SMLM) such as photoactivated localization microscopy (PALM)[5] and stochastic optical reconstruction microscopy (STORM)[6]. The essential principle of the PALM/STORM imaging technique relies on the use of switchable fluorescent probes. Conceptually, PALM/STORM allows a small fraction of fluorophores to stochastically switch between fluorescent ("on") and dark ("off") states and their centroid posistions can be precisely localized mathematically.[7-8] After that, all measured positions will be assembled over thousands of imaging frames to produce a recontructed super-resolution image. In comparison to switchable fluorescent proteins and dyes for super-resolution fluorescence imaging, inorganic quantum dots (QDs) can be a suitable candidate due to their high brightness, remarkable photostability and their natural blinking phenomenon.[9-10] The QD blinking-based super-resolution was first reported in 2005 in which the authors used Independent Component Analysis (ICA) to accurately localize two-point fluorophores as a function of their separation.[11] Blinking CdSe QDs have been used to improve spatial resolution with super resolution optical fluctuation imaging (SOFI).[12] Wang et al. introduced quantum dot blinking with three-dimensional imaging (QDB3) technique, in which 3D super-resolution imaging with blinking QDs is achieved by extracting the point-spread function (PSF) of individual QDs by subtracting subsequent frames.[13] Multicolor imaging has also been presented using QDs as probes.[14-16] However, the typical Cd-based QDs are limited in bioimaging application due to the highly toxic cadmium component. Moreover, commercialized Cd-based QDs are usually coated with thick shells, which render them up to 15-20 nm in size, as well as reducing blinking so that the QDs spend most of the time at the on state and rather short time in the off state. For PALM/STORM, it is ideal for the off-time of each fluorescent probe is much longer than the on-time to limit the number of fluorophores that are in the on state within a single imaging frame. This means that for low-blinking QDs, multiple QDs can be in the on-state within

the area of a point-spread function (PSF) if the labeling density is too high, thereby making it difficult to exploit the natural QD blinking for single-molecule super-resolution imaging. To address the problem of less blinking QDs, blueing of CdSe/ZnSe QD was exploited in super resolution imaging for microtubules[17] and in two color QSTORM imaging of microtubules and mitocondria using two sizes of the QDs (QD 705 nm and QD 565 nm).[14] Recently, a couple of reports introduced biocompatible carbon dots with burst like fluorescent for SMLM imaging of microtubule networks[18] and fixed trout epithelial gill cells.[19] In these reports, eventhough the authors compared the blinking behaviour and localization accuracy of carbon dots with CdSe/ZnS QDs, there was no direct comparision of the effectiveness for super-resolution imaging between the two QDs when imaging the same biological structures. Furthermore, the carbon dots reported in ref 18 required refluxing in 6M HNO_3 followed by 2 stage ultrafiltration to extract the nanoparticles from the reaction mixture, which are not ideal synthesis conditions.

In this report, we extend the toolbox of low toxicity, blinking QDs for SMLM imaging, by using compact $CuInS_2$/ZnS QDs in SMLM imaging of actin filaments. $CuInS_2$ (CIS) is a I-III-VI_2 semiconductor with a direct band gap of 1.45 eV and does not contain any toxic heavy metals.[20-22] As we reported previously,[23] we are able to control both the photoluminescence quantum yield the blinking behavior of CIS QDs by exposing them to different amounts of zinc stearate to control the degree of cation exchange of Cu and In with Zn. Although the synthesis of these QDs does require high temperatures, no concentrated acids are needed and the work up only requires simple solvent extraction steps to produce small QDs with narrow size distributions. To the best of our knowledge, this is the first time that $CuInS_2$/ZnS QDs have been demonstrated in super resolution imaging, and we find that these QDs are comparable in sub-diffraction imaging resolution to the more toxic CdSe/ZnS and to the previously-reported carbon QDs.[18]

3.3. Methods

Materials. Copper (I) iodide (CuI, 99.999%, Sigma Aldrich), indium acetate $In(Ac)_3$, 99.99%, Alfa Aesar), 1-dodecanethiol (DDT, 98%, Sigma Aldrich), 1-octadecene (ODE, 90%, Acros), zinc stearate ($Zn(St)_2$, Acros), mercaptopropionic acid (MPA, Sigma Aldrich), 1-ethyl-3-(3-dimethylaminopropyl)carbodiimide hydrochloride (EDC, Thermo fisher), NeutrAvidin (Thermo fisher). All solvents were purchased from VWR International. Methanol, hexane, dimethylformamide and ethyl acetate were of pure grade.

Synthesis of CIS QDs. CIS QDs are synthesized by modification of the literature methods.[20, 24] Briefly, 0.292g of $In(Ac)_3$, 0.048g of CuI, 1mL of DDT and 10mL of ODE were mixed in a 50mL three-neck round bottom flask (rbf). This solution was first degassed under vacuum for at least 30 minutes at room temperature, then purged with argon for 30 minutes. Subsequently under argon flux the solution was heated to 210 ^{o}C for 40 minutes under argon flow. The color of the solution changed from yellow to orange to deep red as the QDs grew in size. The solution was cooled and then centrifuged at 4000 rpm for 10 minutes. The precipitation was disposed of and the solution was kept for shelling step.

Synthesis of CIS/ZnS QDs. 0.1 mmol (0.063g) of $Zn(St)_2$ was added to a 50mL RBF. Then, 5 mL of ODE, 1 mL of DDT and 5 mL of CIS QDs were added to the RBF. The mixture was stirred under vacuum at 60 °C for 30 minutes and backfilled with argon for 30 minutes. Under argon flux, the reaction temperature was increased to 230 °C. After 6 hours, the reaction solution was cooled to room temperature and was washed three times with a 50/50 mixture of hexane and methanol. Afterward, the sample was precipitated by adding excess acetone. The flocculent precipitate was centrifuged at 4000 rpm for 10 min and the supernatant decanted.

Aqueous phase transfer of CIS/ZnS. The aqueous phase transfer was achieved by replacing the initial surface ligands, DDT by MPA, as shown in the following steps. A mixture of MPA (2 mL, ~20 mmol) and 100mg of dried CIS/ZnS QDs were added into 3 ml N,N-Dimethylformamide (DMF) and formed turbid solution. Then, the mixture was heated to 130 °C and stirred with the blanket of argon. After 10~15 min, the mixture solution became clear gradually. Finally, the product was precipitated by adding 10 mL ethyl acetate and centrifugated at 4000 rpm for 5 min. The precipitates were dissolved in alkaline buffer solution (pH ~ 9) to store.

Conjugation of MPA-CIS/ZnS QDs with neutravidin. Neutravidin was conjugated to the COOH-functionalized CIS/ZnS QDs by a straightforward EDC coupling method. Briefly, in an eppendorf tube, 10 µL of 16 µM stock solution of MPA-CIS/ZnS was diluted to 50 µL using 10 mM borate buffer, pH 7.4. Then, 200 µL of 10 mg/mL neutravidin was added to the QD solution. 10 mg/mL of EDC stock solution was prepared just before use. Immediately, added 50 µL of 10 mg/mL EDC stock solution to the mixture of QD and neutravidin. Gently mixed the solution by pipette and let the mixture sit at room temperature for 10 minutes. Transferred the solution to a clean centrifugal ultrafiltration unit (100 kDa cutoff, Pall Life Sciences) and centrifuged at 6000 rpm in 5 minutes to remove any excess unbound protein. The QDs were re-dissolved in PBS buffer (20 mM, pH 7.2), and filtered through a clean centrifugal filter unit (0.2 mm, Pall Life Sciences) to remove aggregates. The purified neutravidin conjugated CIS/ZnS QD solution was stored at 4 °C for further use.

Polymerization of actin. F-actin (or actin filaments) was freshly prepared before experiment. Dissolved biotin G-actin (monomer) to 0.2 mg/ml with general actin buffer and keep it on ice. Added 100 µl ice cold actin polymerization buffer. The mixture was left overnight at 4 °C (F-actin

formed) and then added ddH_2O to a total volume of 1 ml. The actin filaments (F-actin) were stored at 4 °C for later use in super resolution imaging experiments.

Clean microscope slides and coverslips. Microscope slides and coverslips were immersed with aqua regia solution for 30 minutes, then rinsed with ddH_2O. Afterward, sonicated slides and coverslips with detergent and rinsed with ddH_2O. Dried them with nitrogen gas before used. Construct sample chambers. Placed a tissue on the bench and then put a piece of lens paper on top of the tissue. Placed the slide on the lens paper. Make sure that the clean side of the slide is upwards. Applied two strips of double-sided tape onto the slide along the short edges, leaving a gap of 3-5 mm at the center. Placed the cleaned coverslip on top of the slide. Make sure that the clean side of the coverslip is facing the slide. Used a pipette tip to press down over the double-sided tape. Used a razor to remove excess tape from the slide so that the tape remains only under the coverslip. The open ends of the chamber are left open and serve as inlet and outlet. The chamber volume is several microliters.

Morphology characterization of QDs. Bright field TEM images were taken on a Jeol with an accelerating voltage of 100 kV. The average QD size and size distribution were estimated by analyzing TEM images of 100 QDs using Imagej.

Optical measurement of QDs at the ensemble level. Absorption spectra of CIS/ZnS QDs before and after aqueous transfer were obtained by a Hitachi U-3900H UV/Vis-spectrophotometer and fluorescence emission spectra were recorded with a Perkin Elmer LS55 Luminescence Spectrometer. The relative PL quantum yields (QYs) of various QD samples were comparatively studied by comparison with that of Rhodamine 6G (95% in ethanol) as follows:

$$QY_{QD}=QY_{R6G}\times(OD_{R6G}/OD_{QD}) \times(n_{QD}/n_{R6G})^2$$

n_{QD}: reflective index of hexane for DDT-CIS/ZnS and water for MPA-CIS/ZnS

n_{R6G}: reflective index of ethanol.

The excitation wavelength was set at 485 nm and the optical density (OD) was used ~ 0.05.

Optical measurement of QDs at single-particle level.

Fluorescence Imaging and Single Molecule analysis. All single molecule/particle imaging on coverslips were performed on an Olympus IX 71 inverted fluorescence microscope (Olympus Optical Co., Japan) at total internal refection fluorescence imaging mode (TIRF). The QDs were excited using 488 nm laser (Dream Lasers Technology Co. Ltd., Shanghai, China) and the laser power monitored in front of an oil-immersion microscope objective (NA1.45/100×, Olympus Optical Co., Japan) was measured to be 5 W after it was attenuated. The laser was focused onto the back plane of the objective to provide an illumination area of ~200 × 200 μm^2 on the cover slip. Fluorescence from the sample was collected by the same objective, separated from the excitation light by a dichroic mirror and emission filters (632/148, Semrock), and then directed into an electron-multiplying charge coupled device (EM-CCD, ANDOR iXON Ultra 888) camera. The imaging array was 1024 × 1024 pixels with 13 × 13 μm^2/pixel. The frame rate was set at 10 fps (100 ms/frame) for all samples utilizing a frame transfer approach in which the next frame is acquired while the previous frame is read out, allowing for continuous movies to be acquired. Electron multiplied (EM) gain set to 300 and CCD sensitivity set to 12.13 for the camera. Since the image was taken by an Andor iXon 898 EMCCD (13 μm/pixel) using a 100× objective lens, and the resultant effective dimension for each pixel was about 130 nm.

Blinking statistical analysis. For DDT-CIS/ZnS sample, single particle experiment was prepared by spin casting freshly diluted QDs in hexane. The QD particle density was controlled by changing the concentration of the QDs in the solution before spin coating. For MPA-CIS/ZnS sample, in order to immobilize the QDs on a coverslip surface, the QDs were first functionalized with

neutravidin as describe above. Then, in a sample chamber, pipetted in 20 µl mixture of mPEG and biotinylated mPEG (ratio 99:1) in ddH_2O. Incubate for 10 min. Rinse with 30 µl ddH_2O.

Pipetted in 20 µl neutravidin conjugated CIS/ZnS QDs. Incubated for 10 min. Rinsed with 30 µl ddH_2O. Single-particle trace extraction from the movie acquisition and on and off time probability densities were processed using a Python home-built. Only QDs in the central ~200 × 200 pixels portion of the CCD chip were used to minimize effects of illumination power variations due to the 2-D Gaussian laser illumination profile. At least 100 dots are randomly selected and analyzed for each sample. All measurements were performed at room temperature.

Localization precision experiment. In a sample chamber, pipetted in 20 µl mixture of mPEG and biotinylated mPEG (ratio 95:5) in ddH_2O. Incubated for 10 min. Rinsed with 40 µl ddH_2O. Pipetted in 20 µl neutravidin conjugated CIS/ZnS QDs or streptavidin conjugated CdSe/ZnS QDs. Incubated for 10 min. Rinsed with 40 µl ddH_2O.

Analysis of localization precision for single QD was processed by Matlab and ThunderSTORM,[25] an ImageJ plugin. The integrated signal was collected from 7 × 7 pixels around the maximum of a single spot. To avoid the crosstalk of multiple particles into an intensity trajectory, any fluorescent spot within five pixels of another fluorescent spot was omitted from analysis.

Reconstruction of Super-Resolution Images. In a sample chamber, pipetted in 20 µl mixture of mPEG and biotinylated mPEG (ratio 95:5) in ddH_2O. Incubated for 10 min. Rinsed with 40 µl ddH_2O. Pipetted in 60 µl neutravidin (10 mg/ml). Incubated for 10 min. Rinsed with 100 µl ddH_2O. Pipetted in 20 µl biotinylated actin filaments. Rinsed with 40 µl ddH_2O. Pipetted in 20 µl neutravidin conjugated CIS/ZnS QDs or streptavidin conjugated CdSe/ZnS QDs. Incubated for 10 min. Rinsed with 40 µl ddH_2O.

For reconstructing of super resolution images, a time series of fluorescence images were first acquired. The super-resolution images were then reconstructed with ThunderSTORM.[25] This plugin provides a complete tool for image preprocessing, particle localization, postprocessing analysis, and visualization of data.

3.4. Results and Discussion

In order to conjugate CIS/ZnS QDs to proteins for bioimaging, they must first be rendered water soluble and provide functional groups for protein attachments. To accomplish this, the organic-soluble thiol ligands (DDT) are exchanged for water-soluble thiol ligands, such as MPA. Figure 3.1 illustrates the phase transfer procedure for DDT-CIS/ZnS QDs to aqueous solution using MPA. Briefly, hydrophobic CIS/ZnS QDs were synthesized based on previous reports.[24, 26] Then, washed DDT-CIS/ZnS QDs were mixed with the mixture of DMF and MPA at 130 °C under vigorous stirring for 15 minutes. The sample was then precipitated from DMF with ethyl acetate and re-dispersed into buffer solution (pH 9) to form aqueous soluble CIS/ZnS QDs.[27]

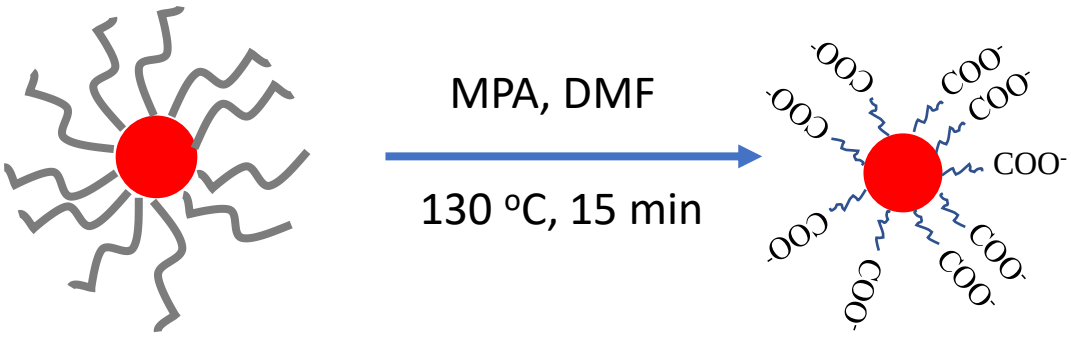

Figure 3.1. Illustration of MPA ligand exchange to render CIS/ZnS QDs to aqueous solution.

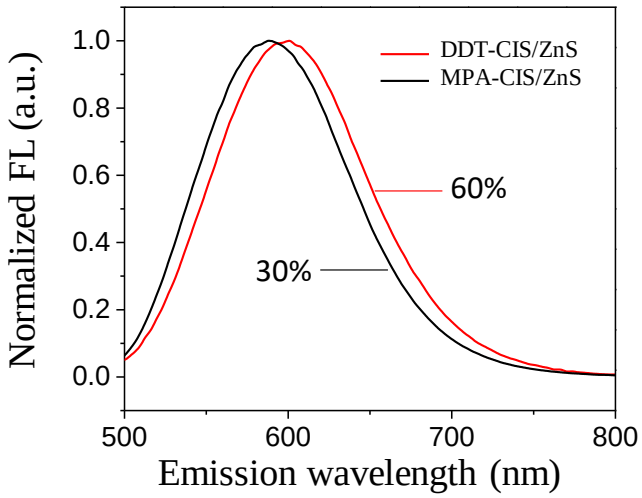

Figure 3.2. PL emission spectra and QY of CIS/ZnS QDs before and after ligand exchange.

Figure 3.2 shows the fluorescence emission peaks and full width at half maxima (fwhm) are relatively the same for the QDs before and after ligand exchange, indicating no obvious change in the particle size. Also, the PL QY of QDs before and after ligand exchange is 60% and 30%, respectively, which is relatively comparable with previous report for CIS/ZnS QDs.[27]

Generally, QDs with compact size and well-dispersed are more favorable for biological imaging application, especially in spatially-confined conditions such as in cell junctions,[28] or in

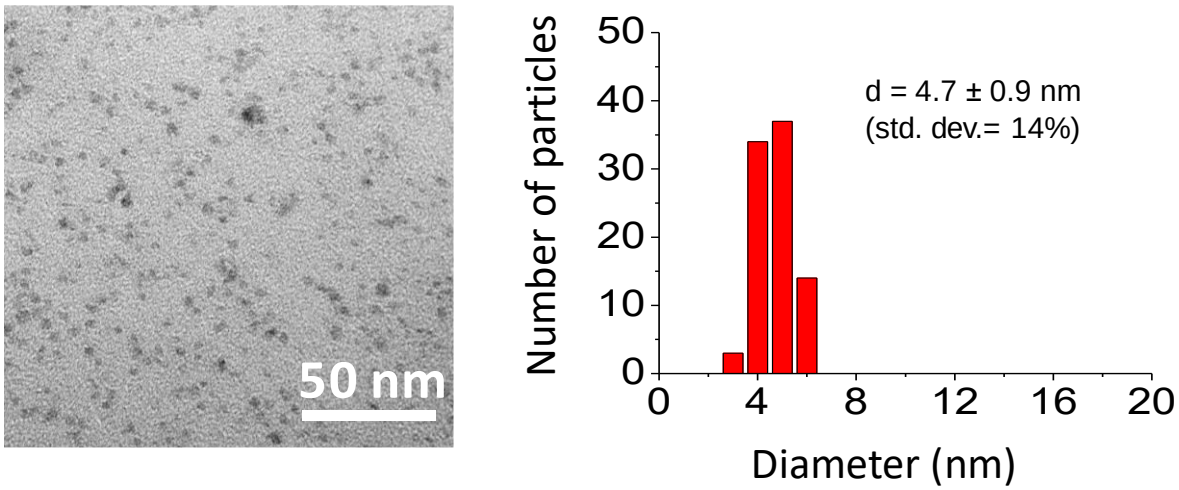

Figure 3.3. TEM image of DDT-CIS/ZnS QDs and the size histogram of the QDs.

overlapping/interacting biological structures.[29] In this report, size analysis by TEM (Figure 3.3) indicates the average size of CIS/ZnS QDs is less than 5 nm, which is compact enough for labeling small, overlapping/interacting biological structures for super resolution imaging applications.

Representative traces of intensity vs time in figures 3.4a indicates that streptavidin-CdSe/ZnS QDs spend most of the time at the on state whereas DDT-CIS/ZnS and neutravidin-CIS/ZnS QDs stochastically give burst like fluorescence (figure 3.4b, c). Statistical analysis of blinking behavior (figure 3.4 d, e) presents the probability density of the on dwell time and off dwell time for over 100 QDs of streptavidin-CdSe/ZnS, CIS/ZnS QDs before and after neutravidin conjugation. Clearly, the on dwell times of streptavidin-CdSe/ZnS QDs are longer compared to that of DDT-CIS/ZnS and neutravidin-CIS/ZnS QDs, especially at the longer time. In the off dwell time results, there is a more pronounced difference of CdSe/ZnS compared to CIS/ZnS QDs. Also, the blinking analysis shows that there is more noticeable deviation in the on dwell time than the off dwell time for CIS/ZnS QDs before and after neutravidin conjugation.

Since the first observation of blinking phenomenon of semiconductor QDs in 1996,[30] the blinking mechanism has not been well elucidated until now. The most widely accepted explanation is that blinking arises when the photoexcited electrons (or holes) is trapped in trap states on the surface of nanocrystals or the surrounding environment.[31] In the resultant charged/trapped nanocrystals, the fluorescence is quenched via nonradiative recombination until the electrons (or holes) tunnel back to the nanocrystal emitting core, rendering it bright again. While majority of QD research have aimed at eliminating blinking, the stochastic switching between an on and off state clearly gives blinking QDs potential for super resolution localization imaging.

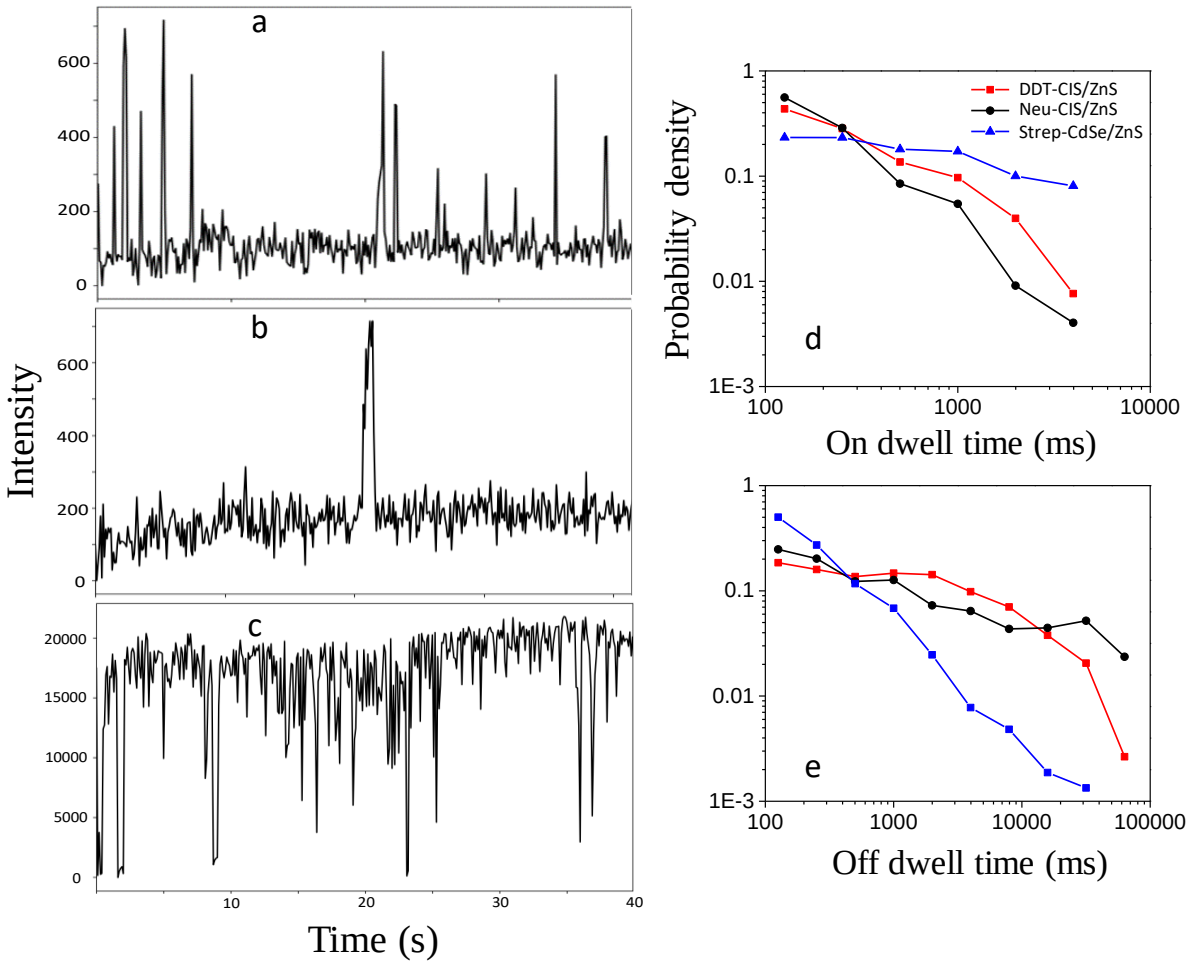

Figure 3.4. Representative traces of intensity vs time of DDT-CIS/ZnS QDs (a); Neutravidin-CIS/ZnS QDs (b) and-streptavidin CdSe/ZnS (c). Statistical analysis for Pon (d) and Poff (e) of blinking QDs.

For fluorescent probes that can spend the majority of their time at the off state, while only giving burst-like signal in the on state, higher density of probes can be labeled on samples to be imaged, resulting in more details for the final reconstructed image.[18] For localization precision experiments of single QDs, neutravidin-CIS/ZnS and streptavidin CdSe/ZnS QDs were immobilized on a coverslip surface as depicted in figure 3.5.

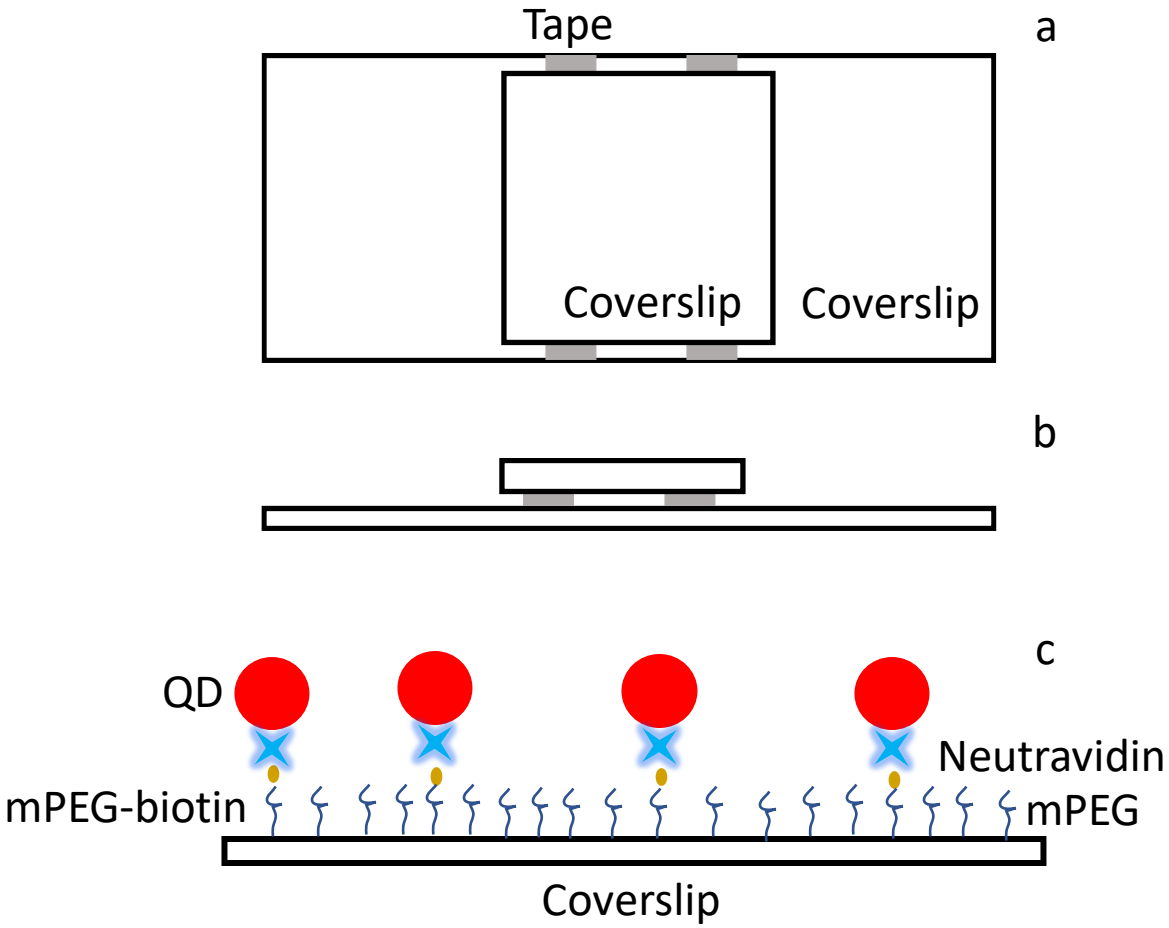

Figure 3.5. Sketch of a typical sample chamber. (a) Top view; (b) Side view; (c) Illustration for immobilization of MPA-CIS/ZnS on a coverslip surface.

The surface of a coverslip was coated with a mixture of mPEG and mPEG-biotin, in which the concentration of mPEG-biotin is just 1% so that the immobilized QDs are well dispersed.

The carboxylated MPA-CIS/ZnS QDs can be conjugated to neutravidin via EDC coupling, which cross-links carboxyl groups on the QDs to amine groups on the proteins. Unconjugated proteins were removed by a 100 kDa cutoff centrifugal filter unit.

First, surface-immobilized CdSe/ZnS and CIS/ZnS samples were imaged. A typical image is shown in figure 3.6a. A bright field image of QDs immobilized on a coverslip surface and a PSF

of a single CIS/ZnS QD were shown in figures 3.6 b and c, respectively. The localization precision is described as $\sigma^2 = s^2/N + a^2/(12N) + 8\pi s^2 b^2/(N^2 b^2)$,[32] where s is the standard deviation (SD) of the PSF, a is the pixel size (130 nm) in the image, b is the background noise, and N is the number of photons. By statistical analysis, the averaged localization precision of the CIS/ZnS QDs is 7.2 nm and CdSe/ZnS QDs is 1.6 nm, which is expected due to the higher brightness of commercialized CdSe/ZnS QDs.

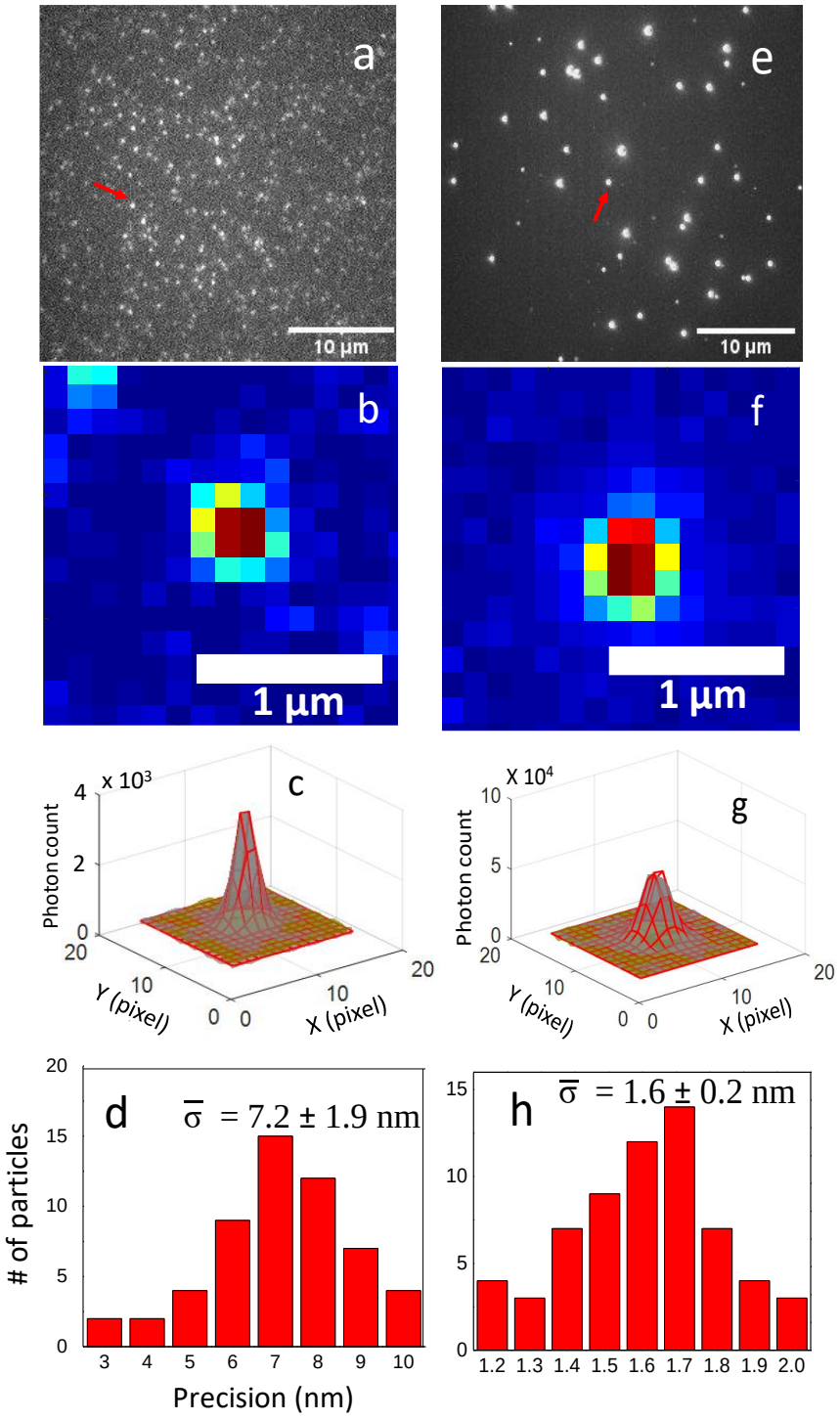

Figure 3.6. Left images are for CIS/ZnS QDs; right images are for CdSe/ZnS QDs. (a, e) bright field images of QDs immobilized on a coverslip surface. (b, f) Images of a single QD, indicated by the red arrow in (a) and (e). (c, f) Fitting the point spread function of the single QD with a

To evaluate the effectiveness of super-resolution localization, a region of the image in which CIS/ZnS QD emission overlapped was chosen. Figure 3.7 a and b present the stacked image in which the maximum intensity of each pixel over 300 frames was determined (to show the intensity of the QD only when it is on) and the reconstructed super-resolution image, respectively. The comparative analysis of the two images demonstrates an improvement in spatial resolution. Figure 3.7 c shows a representative line profile of two spots immobilized within a PSF (~350 nm) showing two unresolved peaks, but after reconstruction, two well-separated peaks are evident.

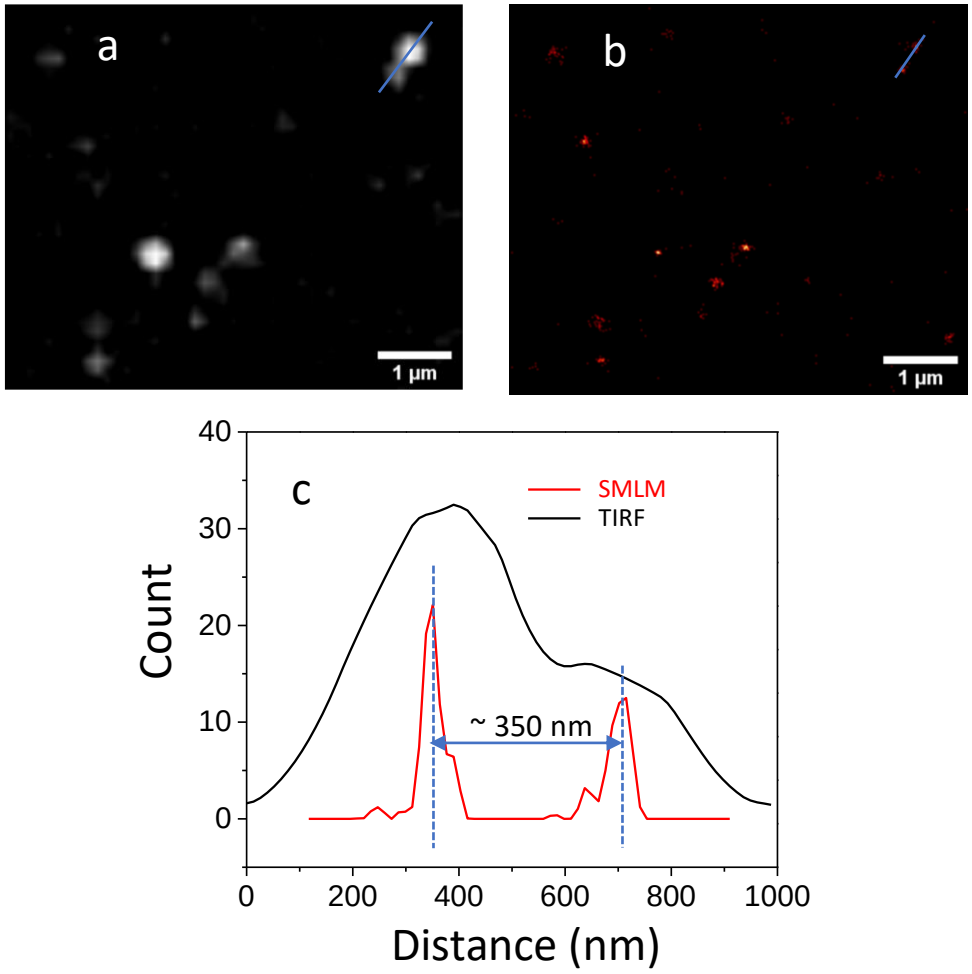

Figure 3.7. (a) bright field (or TIRF) image and (b) reconstructed (or SMLM) image of immobilized QDs. (c) line scan profile of two adjacent QDs.

Actin is one of the key proteins involved in muscle contraction, cell division, and migration. It is a globular protein with molecular weight of 42 kDa and diameter of 5 nm. In presence of salts and magnesium, it polymerizes into long filaments with two helically twisted strands.[33-34] The length of actin filaments can reach up to several microns, while the thickness is about 10 nm (size of two actin monomers), making super-resolution imaging ideal to study them.[35-36] Figure 3.8 illustrates how QDs were labeled onto f-actin filaments. The surface of a coverslip was coated with a mixture

of mPEG and mPEG-biotin as described in the localization precision experiment. An excess amount of Neutravidin was used to both provide adequate sites to bind the biotinylated actin filaments and to saturate the biotin sites on the surface to minimize the unspecific bindings of Neutravidin-CIS/ZnS and streptavidin CdSe/ZnS QDs to mPEG-biotin. Then the polymerized biotinylated actin filaments were added, which bound to free sites on the Neutravidin, and finally strepativin-CdSe/ZnS or neutravidin-CIS/ZnS QDs were labeled onto f-actin filaments via the strong Neutravidin/streptavidin-biotin affinity.

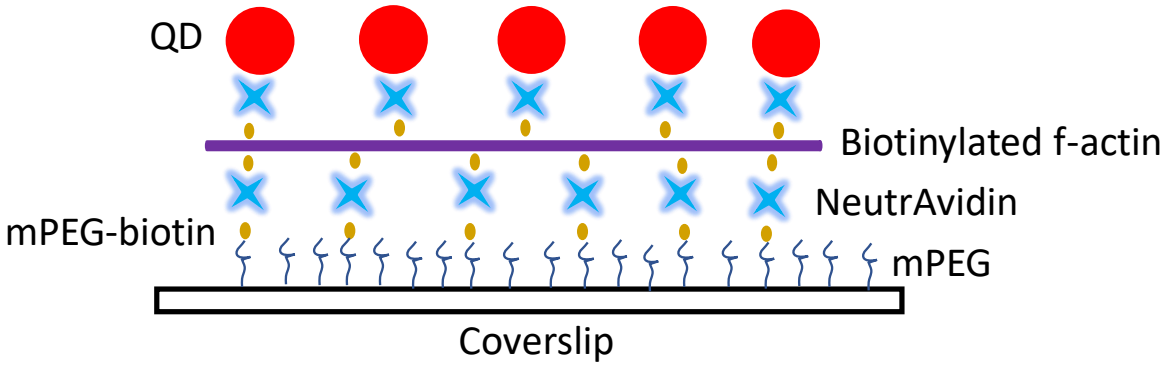

Figure 3.8. Illustration of QDs labeled onto actin filaments.

Figure 3.9 shows the TIRF images, reconstructed super-resolution images and line scan profiles of CIS/ZnS QDs (left) and CdSe/ZnS QDs (right) labeled actin filaments. The average width of actin filaments from the Gaussian fit (fwhm) is determined to be 79 nm for CIS/ZnS QDs and 76 nm for CdSe/ZnS, which is approximately 4.5-5 times higher resolution than that acquired by TIRF imaging. This is an interesting result, since the localization precision of CIS/ZnS QDs is 4.5 times less precise than that of CdSe/ZnS QDs but the two QDs give relatively the same resolution for super resolution imaging of actin filaments. This can be explained that even the CdSe/ZnS QDs give better localization precision at single QD due to their higher brightness, they mostly stay at the on state so at a given binning time many QDs fluoresce, leading to the less precise localization

when labeling at high density for super resolution imaging. However, when compared to the width of actin filaments which is about 10 nm, these results still leave room for some improvement for all 3 types of QD (CdSe/ZnS, CIS/ZnS and Carbon QDs). Endesfelder et al. achieved a width of 30 nm in imaging actin filaments by labeling them with both carbocyanine fluorophores Cy5 and Alexa 647.[37] Also, in this report, the authors used myosin II to coat the coverslip surface, which may avoid possibility of non-specific bindings of QDs. Another possible method for labeling of QDs on actin filaments to reduce non-specific binding is that QDs first can be conjugated with actin monomers before the polymerization step.[33]

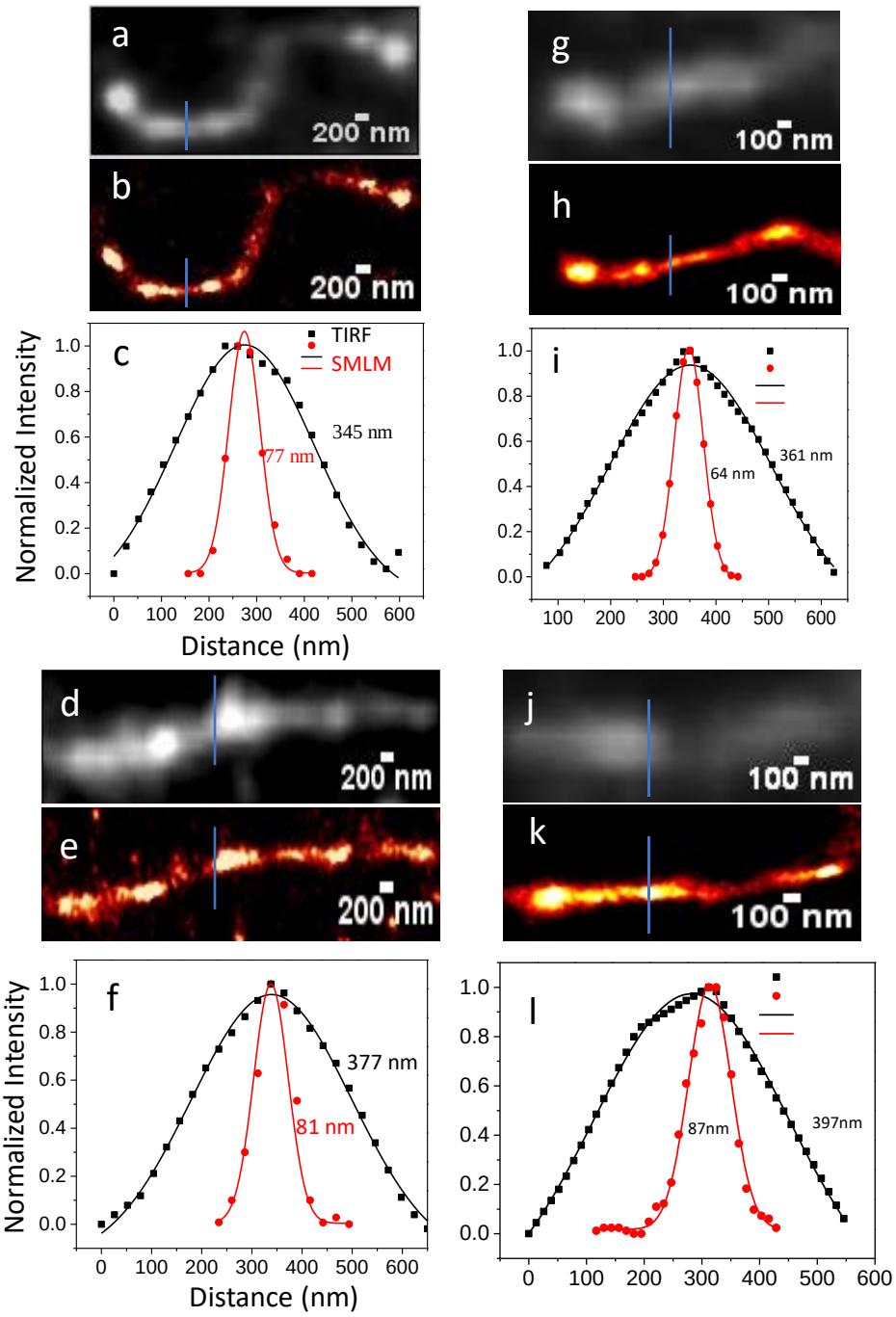

Figure 3.9. Left images are for CIS/ZnS QDs. Right images are for CdSe/ZnS QDs. (a, g, d and j) bright field (or TIRF) images; (b, h, e and k) reconstructed (or SMLM) images of actin filaments. (c, i, f and l) line scan profiles of the widths of actin filaments.

3.5. Conclusions

For the first time, compact CIS/ZnS QDs with burst like fluorescence were used as probes for single molecule localization microscopy. This material could offer the opportunity to fulfill the potential of semiconductor QDs without the toxicity limitations encountered by II-VI QDs. The FL QY of CIS/ZnS QDs after phase transferring is about 30% which is high enough for super resolution imaging. The average localization precision of single QD for CIS/ZnS is 7.2 nm which is approximately 4.5 times less precise compared to that of commercialized CdSe/ZnS QDs. However, because the aqueous soluble CIS/ZnS QDs give burst like fluorescence while the CdSe/ZnS QDs spend most of the time at the on state, with a relatively equal concentration of sample labling, both of the QDs obtained 4.5 times higher in resolution for super-resolution imaging when compared to those acquired from conventional TIRF imaging. This report highlights that CIS/ZnS QD can be a potential candidate for using compact, non-toxic QDs for single molecule localization imaging of biological structures.

3.6. References

1. Hell, S. W., Far-field optical nanoscopy. *Science* **2007,** *316* (5828), 1153-1158.

2. Huang, B.; Babcock, H.; Zhuang, X., Breaking the Diffraction Barrier: Super-Resolution Imaging of Cells. *Cell* **2010,** *143* (7), 1047-1058.

3. Hell, S. W.; Wichmann, J., BREAKING THE DIFFRACTION RESOLUTION LIMIT BY STIMULATED-EMISSION - STIMULATED-EMISSION-DEPLETION FLUORESCENCE MICROSCOPY. *Optics Letters* **1994,** *19* (11), 780-782.

4. Klar, T. A.; Hell, S. W., Subdiffraction resolution in far-field fluorescence microscopy. *Optics Letters* **1999,** *24* (14), 954-956.

5. Betzig, E.; Patterson, G. H.; Sougrat, R.; Lindwasser, O. W.; Olenych, S.; Bonifacino, J. S.; Davidson, M. W.; Lippincott-Schwartz, J.; Hess, H. F., Imaging intracellular fluorescent proteins at nanometer resolution. *Science* **2006,** *313* (5793), 1642-1645.

6. Rust, M. J.; Bates, M.; Zhuang, X., Sub-diffraction-limit imaging by stochastic optical reconstruction microscopy (STORM). *Nature Methods* **2006,** *3* (10), 793-795.

7. Gustafsson, M. G. L., Surpassing the lateral resolution limit by a factor of two using structured illumination microscopy. *Journal of Microscopy* **2000,** *198*, 82-87.

8. Shroff, H.; Galbraith, C. G.; Galbraith, J. A.; White, H.; Gillette, J.; Olenych, S.; Davidson, M. W.; Betzig, E., Dual-color superresolution imaging of genetically expressed probes within individual adhesion complexes. *Proceedings of the National Academy of Sciences of the United States of America* **2007,** *104* (51), 20308-20313.

9. Chan, W. C. W.; Nie, S. M., Quantum dot bioconjugates for ultrasensitive nonisotopic detection. *Science* **1998,** *281* (5385), 2016-2018.

10. Resch-Genger, U.; Grabolle, M.; Cavaliere-Jaricot, S.; Nitschke, R.; Nann, T., Quantum dots versus organic dyes as fluorescent labels. *Nature Methods* **2008,** *5* (9), 763-775.

11. Lidke, K. A.; Rieger, B.; Jovin, T. M.; Heintzmann, R., Superresolution by localization of quantum dots using blinking statistics. *Opt. Express* **2005,** *13* (18), 7052-7062.

12. Dertinger, T.; Colyer, R.; Iyer, G.; Weiss, S.; Enderlein, J., Fast, background-free, 3D super-resolution optical fluctuation imaging (SOFI). *Proceedings of the National Academy of Sciences of the United States of America* **2009,** *106* (52), 22287-22292.

13. Wang, Y.; Fruhwirth, G.; Cai, E.; Ng, T.; Selvin, P. R., 3D Super-Resolution Imaging with Blinking Quantum Dots. *Nano letters* **2013,** *13* (11), 5233-5241.

14. Xu, J.; Tehrani, K. F.; Kner, P., Multicolor 3D Super-resolution Imaging by Quantum Dot Stochastic Optical Reconstruction Microscopy. *ACS Nano* **2015,** *9* (3), 2917-2925.

15. Chizhik, A. M.; Stein, S.; Dekaliuk, M. O.; Battle, C.; Li, W.; Huss, A.; Platen, M.; Schaap, I. A. T.; Gregor, I.; Demchenko, A. P.; Schmidt, C. F.; Enderlein, J.; Chizhik, A. I., Super-Resolution Optical Fluctuation Bio-Imaging with Dual-Color Carbon Nanodots. *Nano Letters* **2016,** *16* (1), 237-242.

16. Chen, X.; Liu, Z.; Li, R.; Shan, C.; Zeng, Z.; Xue, B.; Yuan, W.; Mo, C.; Xi, P.; Wu, C.; Sun, Y., Multicolor Super-resolution Fluorescence Microscopy with Blue and Carmine Small Photoblinking Polymer Dots. *ACS Nano* **2017,** *11* (8), 8084-8091.

17. Hoyer, P.; Staudt, T.; Engelhardt, J.; Hell, S. W., Quantum Dot Blueing and Blinking Enables Fluorescence Nanoscopy. *Nano Letters* **2011,** *11* (1), 245-250.

18. He, H.; Liu, X.; Li, S.; Wang, X.; Wang, Q.; Li, J.; Wang, J.; Ren, H.; Ge, B.; Wang, S.; Zhang, X.; Huang, F., High-Density Super-Resolution Localization Imaging with Blinking Carbon Dots. *Analytical Chemistry* **2017,** *89* (21), 11831-11838.

19. Zhi, B.; Cui, Y.; Wang, S.; Frank, B. P.; Williams, D. N.; Brown, R. P.; Melby, E. S.; Hamers, R. J.; Rosenzweig, Z.; Fairbrother, D. H.; Orr, G.; Haynes, C. L., Malic Acid Carbon Dots: From Super-resolution Live-Cell Imaging to Highly Efficient Separation. *ACS Nano* **2018,** *12* (6), 5741-5752.

20. Li, L.; Daou, T. J.; Texier, I.; Kim Chi, T. T.; Liem, N. Q.; Reiss, P., Highly Luminescent CuInS2/ZnS Core/Shell Nanocrystals: Cadmium-Free Quantum Dots for In Vivo Imaging. *Chemistry of Materials* **2009,** *21* (12), 2422-2429.

21. Pons, T.; Pic, E.; Lequeux, N.; Cassette, E.; Bezdetnaya, L.; Guillemin, F.; Marchal, F.; Dubertret, B., Cadmium-Free CuInS2/ZnS Quantum Dots for Sentinel Lymph Node Imaging with Reduced Toxicity. *ACS Nano* **2010,** *4* (5), 2531-2538.

22. Mandal, G.; Darragh, M.; Wang, Y. A.; Heyes, C. D., Cadmium-free quantum dots as time-gated bioimaging probes in highly-autofluorescent human breast cancer cells. *Chemical Communications* **2013,** *49* (6), 624-626.

23. Nguyen, A. T.; Gao, F.; Baucom, D.; Heyes, C. D., CuInS2-Doped ZnS Quantum Dots Obtained via Non-Injection Cation Exchange Show Reduced but Heterogeneous Blinking and Provide Insights into Their Structure–Optical Property Relationships. *The Journal of Physical Chemistry C* **2020,** *124* (19), 10744-10754.

24. Li, L.; Pandey, A.; Werder, D. J.; Khanal, B. P.; Pietryga, J. M.; Klimov, V. I., Efficient Synthesis of Highly Luminescent Copper Indium Sulfide-Based Core/Shell Nanocrystals with Surprisingly Long-Lived Emission. *Journal of the American Chemical Society* **2011,** *133* (5), 1176-1179.

25. Ovesný, M.; Křížek, P.; Borkovec, J.; Švindrych, Z.; Hagen, G. M., ThunderSTORM: a comprehensive ImageJ plug-in for PALM and STORM data analysis and super-resolution imaging. *Bioinformatics* **2014,** *30* (16), 2389-2390.

26. Chen, B.; Zhong, H.; Zhang, W.; Tan, Z. a.; Li, Y.; Yu, C.; Zhai, T.; Bando, Y.; Yang, S.; Zou, B., Highly Emissive and Color-Tunable CuInS2-Based Colloidal Semiconductor Nanocrystals: Off-Stoichiometry Effects and Improved Electroluminescence Performance. *Advanced Functional Materials* **2012,** *22* (10), 2081-2088.

27. Zhao, C.; Bai, Z.; Liu, X.; Zhang, Y.; Zou, B.; Zhong, H., Small GSH-Capped CuInS2 Quantum Dots: MPA-Assisted Aqueous Phase Transfer and Bioimaging Applications. *ACS Applied Materials & Interfaces* **2015,** *7* (32), 17623-17629.

28. Cai, E.; Ge, P.; Lee, S. H.; Jeyifous, O.; Wang, Y.; Liu, Y.; Wilson, K. M.; Lim, S. J.; Baird, M. A.; Stone, J. E.; Lee, K. Y.; Davidson, M. W.; Chung, H. J.; Schulten, K.; Smith, A. M.; Green, W. N.; Selvin, P. R., Stable Small Quantum Dots for Synaptic Receptor Tracking on Live Neurons. *Angewandte Chemie International Edition* **2014,** *53* (46), 12484-12488.

29. Shroff, H.; Galbraith, C. G.; Galbraith, J. A.; Betzig, E., Live-cell photoactivated localization microscopy of nanoscale adhesion dynamics. *Nature Methods* **2008,** *5* (5), 417-423.

30. Nirmal, M.; Dabbousi, B. O.; Bawendi, M. G.; Macklin, J. J.; Trautman, J. K.; Harris, T. D.; Brus, L. E., Fluorescence intermittency in single cadmium selenide nanocrystals. *Nature* **1996,** *383* (6603), 802-804.

31. Galland, C.; Ghosh, Y.; Steinbrück, A.; Sykora, M.; Hollingsworth, J. A.; Klimov, V. I.; Htoon, H., Two types of luminescence blinking revealed by spectroelectrochemistry of single quantum dots. *Nature* **2011,** *479* (7372), 203-207.

32. Thompson, R. E.; Larson, D. R.; Webb, W. W., Precise nanometer localization analysis for individual fluorescent probes. *Biophysical Journal* **2002,** *82* (5), 2775-2783.

33. Patolsky, F.; Weizmann, Y.; Willner, I., Actin-based metallic nanowires as bio-nanotransporters. *Nature Materials* **2004,** *3* (10), 692-695.

34. Wu, K. C.-W.; Yang, C.-Y.; Cheng, C.-M., Using cell structures to develop functional nanomaterials and nanostructures – case studies of actin filaments and microtubules. *Chemical Communications* **2014,** *50* (32), 4148-4157.

35. Xu, K.; Babcock, H. P.; Zhuang, X., Dual-objective STORM reveals three-dimensional filament organization in the actin cytoskeleton. *Nature Methods* **2012,** *9* (2), 185-188.

36. Izeddin, I.; El Beheiry, M.; Andilla, J.; Ciepielewski, D.; Darzacq, X.; Dahan, M., PSF shaping using adaptive optics for three-dimensional single-molecule super-resolution imaging and tracking. *Optics Express* **2012,** *20* (5), 4957-4967.

37. van de Linde, S.; Wolter, S.; Heilemann, M.; Sauer, M., The effect of photoswitching kinetics and labeling densities on super-resolution fluorescence imaging. *Journal of Biotechnology* **2010,** *149* (4), 260-266.

Chapter 4. Conclusions and future direction

The highlight of this dissertation is that it includes projects starting from synthesis and characterization of CIS/ZnS QDs and then applications fast blinking CIS/ZnS QDs as fluorescent probes for single particle localization super resolution imaging.

In the first project presented in chapter 2, the relationship of structures, elemental analysis and photophysics of CIS/ZnS QDs are carefully investigated. The CIS cores with In/Cu ratio is 4/1 were first synthesized based on previous report.[1] Then CIS cores were encapsulated with different concentrations (0.1; 1; 2; 4 mmol) of Zn precursor, $Zn(St)_2$. Instead of using hot injection method,[2-3] during the shelling procedure in this dissertation, Zn precursor was added to CIS core solution at room temperature and heated up to 230 ^oC. Thus, the procedure can be more applicable for large scale production of the QDs. The resulting QDs were relatively isotropic compared to other reports and had average sizes of 4-8 nm with different concentrations of Zn precursor used. XRD and HRTEM analysis suggested that the structure of QDs changed from chalcopyrite for CIS cores to zinc blende for CIS/ZnS. Elemental and spectroscopic analysis indicated that as concentration of Zn precursor increased, the size of CIS became smaller due to excess cation exchange and eventually reached 'cluster'-size regime embedded in ZnS lattice. Furthermore, interesting properties between ensemble and single particle of CIS/ZnS QDs were observed, which were high PL QY but fast blinking for CIS/ZnS QDs synthesized at 0.1 mmol of Zn precursor, whereas low PL QY but relatively suppressed blinking for QDs when 2 and 4 mmol of Zn was used.

For single particle analysis, a wide heterogeneity in blinking behavior from QD-to-QD is evident, especially when 2 and 4 mmol of zinc precursor was used and a subpopulation statistical analysis shows that the on-state dwell times change from multiexponential (or inverse power law) behavior towards more mono-exponential behavior for particles that spend more of their time in the on-

state. These results indicate that, as the number of $CuInS_2$ emitting centers is reduced, the number of pathways leading to the off-state decreases, and a model is proposed to relate this behavior to the QD structure.

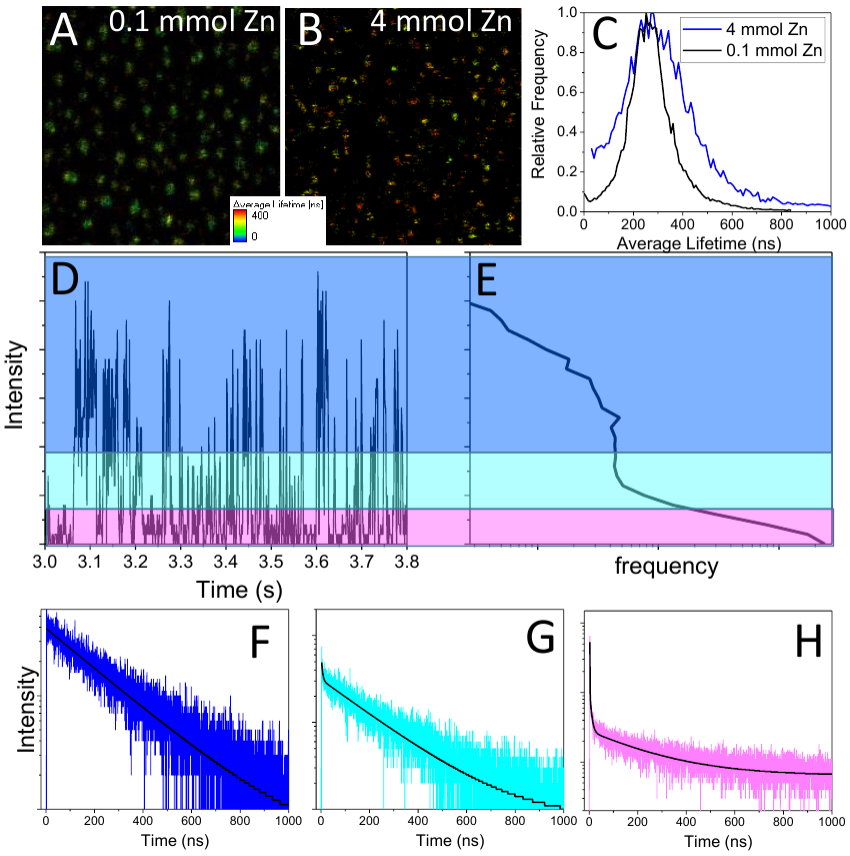

Figure 4.1. (A-B). FLIM images and (C). single particle histogram for CIS/ZnS QDs at 0.1 and 4 mmol of Zn. (D). time dependent intensity and (E) PCH of CIS/ZnS QDs at 4 mmol of Zn. F-H. intensity resolved fluorescence lifetime curves with fitting of high intensity 'on' state (blue), intermediate intensity 'on' state (cyan) and 'off' state (magenta).

One project can be done in the future in our group is to investigate the single particle lifetime for CIS/ZnS QDs. Preliminary results showed that there is a significant difference in lifetime between QDs at different Zn concentrations. FLIM image and lifetime histogram of single particle for QDs at 0.1 and 4 mmol is show in figure 4.1. Clearly, single QD of 4 mmol Zn shows wider heterogeneity compared to 0.1 mmol Zn. Time dependent fluorescence intensity and photon counting histogram (PCH) for single QD of 4 mmol Zn show a distribution of intensity levels.

There are three states can be extract out from the PCH. First is high intensity state having long lifetime and monoexponential decay time of 300 ns. Second is intermediate state with short 5ns component in combination with 300 ns component. Third is lowest state with 3 components of 1 ns, 5 ns and 300 ns. Interestingly, the long component is still present in the intermediate and lowest states.

In the first project we proposed the wide heterogeneity in blinking of CIS doped ZnS QDs resulted from the differences in positions of emitting centers CIS embedded in ZnS lattice. Therefore, it would be more comprehensive if one can use advanced imaging and spectroscopy techniques (i.e. STEM/EELS[4-5] and/or XANES, EXAFS and EPR)[6] to confirm our model.

Currently, one project related to CIS/ZnS QDs is being carried out in our lab. Due to high level of cation exchange during the shelling ZnS for CIS cores, we want to add Zn precursor during CIS core synthesis in order to pre-alloy the CIS core, then proceed with encapsulating the Zn/CIS cores with ZnS. Different reaction conditions will be carefully investigated such as of amount of Zn precursors added during core synthesis, amount of Zn precursors added during shelling and also reaction time.

In project 2, to our best knowledge, this is the first time CIS/ZnS QDs are used as fluorescent probes for single molecule localization super resolution imaging.

First, CIS/ZnS QDs were rendered to aqueous solution by ligand exchange with MPA. Blinking analysis of CIS/ZnS QDs before and after ligand exchange indicated that MPA-CIS/ZnS blink even more than DDT-CIS/ZnS, which make them suitable for single particle localization super resolution imaging.

In this project, we separately labeled CIS/ZnS QDs and commercial CdSe/ZnS QDs onto actin fibers, then compared the resolution of reconstructed super resolution images. The results showed

that the CdSe/ZnS QDs gave better precision for single molecule localization due to their higher brightness. However, both QDs gave the same resolution for reconstructed resolution images due to the fact that CdSe/ZnS QDs stay mostly at the on state so their fluorescent signals in a certain binning time overlapped with each other, whereas fast blinking CIS/ZnS QDs can stochastically fluoresce so their locations can be separately determined.

During the seconds project the most challenging steps were bioconjugation of CIS/ZnS QDs to Neutravidin via EDC coupling and how to avoid the binding of CIS/ZnS QDs with mPEG-biotin when they are labeled to actin-filament.

For bioconjugation, even though EDC coupling is a widely used method for bioconjugation of nanoparticles with biological molecules, this method is highly pH dependent and usually causes precipitation. Snee's research group recently reported a mini-review for their accomplishments in utilizing their own synthesized molecules showing higher yield in bioconjugation compared to EDC coupling.[7] Particularly, methyl-terminated poly(ethylene glycol) 350 Da (mPEG-350) functionalized CdSe/ZnS QDs conjugation with amine functionalized dyes yields as high as 95%. Also, they used mPEG-350 for conjugation of $AgInS_2$/ZnS QDs which also belong to I-III-VI QDs as CIS/ZnS QDs. Therefore, one of possible project related to my second project is to systematically investigate the chemistry of available conjugation agents to offer the highest yield. For non-specific binding of CIS/ZnS QDs on coverslip surface, even high amount of Neutravidin was used to bind with mPEG-biotin, the binding of CIS/ZnS QDs to mPEG-biotin is still high. Heilemann et al. reported using myosin II to cover to surface of coverslip and the reconstructed super resolution image show the resolution for actin filament is 30 nm,[8] which is two times better than our results. Thus, myosin II can be a potential candidate for covering glass surface in actin filament imaging.

I have also tried to use CIS/ZnS QDs as fluorescent probes for super resolution imaging of T3T fixed cells but due to high amount of non-specific binding of QDs in cells, the project has to be postponed. Recently, Smith et al. combined zwitterion and oligo(ethylene glycol) to functionalize surface of QDs for reducing of non-specific binding.[8] Their study showed that this combination can significantly improve the non-specific binding resistance when labeling QDs to proteins, fixed cells and live cells. Thus, this method can be applied in the T3T fixed cells super resolution imaging.

4.1. References

1. Chen, B.; Zhong, H.; Zhang, W.; Tan, Z. a.; Li, Y.; Yu, C.; Zhai, T.; Bando, Y.; Yang, S.; Zou, B., Highly Emissive and Color-Tunable CuInS2-Based Colloidal Semiconductor Nanocrystals: Off-Stoichiometry Effects and Improved Electroluminescence Performance. *Advanced Functional Materials* **2012,** *22* (10), 2081-2088.

2. Zhang, A.; Dong, C.; Li, L.; Yin, J.; Liu, H.; Huang, X.; Ren, J., Non-blinking (Zn)CuInS/ZnS Quantum Dots Prepared by In Situ Interfacial Alloying Approach. *Scientific reports* **2015,** *5*, 15227.

3. Zang, H.; Li, H.; Makarov, N. S.; Velizhanin, K. A.; Wu, K.; Park, Y. S.; Klimov, V. I., Thick-Shell CuInS2/ZnS Quantum Dots with Suppressed "Blinking" and Narrow Single-Particle Emission Line Widths. *Nano Lett* **2017,** *17* (3), 1787-1795.

4. Orfield, N. J.; McBride, J. R.; Keene, J. D.; Davis, L. M.; Rosenthal, S. J., Correlation of Atomic Structure and Photoluminescence of the Same Quantum Dot: Pinpointing Surface and Internal Defects That Inhibit Photoluminescence. *ACS Nano* **2015,** *9* (1), 831-839.

5. Orfield, N. J.; McBride, J. R.; Wang, F.; Buck, M. R.; Keene, J. D.; Reid, K. R.; Htoon, H.; Hollingsworth, J. A.; Rosenthal, S. J., Quantum Yield Heterogeneity among Single Nonblinking Quantum Dots Revealed by Atomic Structure-Quantum Optics Correlation. *ACS Nano* **2016,** *10* (2), 1960-1968.

6. Manikandan, D.; Yadav, A. K.; Jha, S. N.; Bhattacharyya, D.; Boukhvalov, D. W.; Murugan, R., XANES, EXAFS, EPR, and First-Principles Modeling on Electronic Structure and Ferromagnetism in Mn Doped SnO2 Quantum Dots. *The Journal of Physical Chemistry C* **2019,** *123* (5), 3067-3075.

7. Snee, P. T., The Role of Colloidal Stability and Charge in Functionalization of Aqueous Quantum Dots. *Accounts of Chemical Research* **2018,** *51* (11), 2949-2956.

8. van de Linde, S.; Wolter, S.; Heilemann, M.; Sauer, M., The effect of photoswitching kinetics and labeling densities on super-resolution fluorescence imaging. *Journal of Biotechnology* **2010,** *149* (4), 260-266.